Elastic scattering of protons at the TOTEM experiment at the LHC

A thesis submitted to the Eötvös University of Budapest for the degree of
Doctor of Philosophy
in the Faculty of Natural Sciences

Written by: Frigyes Nemes

PhD School of Physics
Particle and Astrophysics program

PhD school leader:	Dr. László Palla, professor
PhD program leader:	Dr. Ferenc Csikor, professor
Supervisor:	Tamás Csörgő, DSc, scientific advisor, honorary professor
Co-Supervisor:	Dr. Máté Csanád, associate professor

2015

Elastic scattering of protons at the TOTEM experiment at the LHC

A thesis presented for the degree of Doctor of Philosophy

Written by: Frigyes Nemes

Eötvös University, Budapest, Hungary, PhD School of Physics, Particle and Astrophysics program, 2015

PhD school leader: Dr. László Palla, DSc, professor

PhD program leader: Dr. Ferenc Csikor, DSc, professor

Supervisor: Tamás Csörgő, Member of the European Academy, DSc, scientific advisor, honorary professor

Co-Supervisor: Dr. Máté Csanád, associate professor

Abstract

The TOTEM experiment at the LHC at CERN is optimized to measure elastic and diffractive scattering at the LHC and measures the total proton-proton cross-section with the luminosity-independent method. The TOTEM experiment uses the special technique of movable beam pipe insertions – called Roman Pots – to detect very forward protons. The reconstruction of the forward proton kinematics requires the precise understanding of the LHC beam optics. A new method of LHC optics determination is reported, which exploits kinematical distributions of elastically scattered proton-proton data measured by the Roman Pots of the TOTEM experiment. The method has been successfully applied to data samples recorded since 2010.

The interpretation of the proton-proton elastic differential cross-section is a challenging task. The geometrical model of proton-proton elastic scattering of Bialas and Bzdak is fitted to ISR data and to data measured by the TOTEM experiment at LHC energy of $\sqrt{s} = 7$ TeV. The Bialas-Bzdak model is generalized and improved in order to give a satisfactory and unified description of the ISR and LHC data. The improved model is extrapolated to future LHC energies and beyond.

Contents

Chapter 1

Introduction

Proton-proton (pp) scattering reactions are partly diffractive by means of the presence of a diffractive pattern in the final state; elastic pp scattering is a typical example where a diffractive minimum (the "dip") appears in the measured elastic differential cross-section [1–3]. The term *diffraction* was introduced in nuclear high-energy physics in the 1950's by Landau and his school in strict analogy with optical diffraction [4].

Diffractive processes represent about 50 % of the total pp cross-section $\sigma_{\rm tot}$ at the Large Hadron Collider (LHC) [5–7]. The general purpose experiments at the LHC are focusing mainly to non-diffractive events, where it is the most likely that the creation of a new particle happens, enlarging our knowledge about the Universe. This certainly doesn't mean that diffractive physics is not worth to investigate and the TOTEM (TOTal cross section, Elastic scattering and diffraction dissociation Measurement at the LHC) experiment at the LHC at CERN (Conseil Européen pour la Recherche Nucléaire) is dedicated to measure the total pp cross-section and to study diffractive physics [5].

The TOTEM experiment is placed at the Interaction Point 5 (IP5) of the LHC and uses the special technique of movable beam pipe insertions – called Roman Pots (RP) – to detect very forward protons. The reconstruction of the kinematics of forward protons require the precise understanding of the LHC beam optics defined by the LHC magnet lattice, see Fig. 2.2. My main task in the physics program of the TOTEM experiment became the calibration of the LHC optics, resulting in the validation and application of a novel experimental method to determine the optics of the LHC accelerator at IP5 utilizing measured RP pp data [8, 9].

My PhD work also included the interpretation of elastic pp differential cross-section data using the particular geometrical model of A. Bialas and A. Bzdak (BB model) [10]. The BB model is based on the so-called "eikonal picture", which is the high-energy physics analogue of optical Fraunhofer-diffraction [2]. A limitation of the original BB model that its purely imaginary elastic scattering amplitude vanishes at the diffractive minima, which leads to vanishing elastic differential cross-section value at these points.

I have fitted the original BB model at ISR energies and at the LHC energy of $\sqrt{s} = 7$ TeV to the measured TOTEM data [11]; the $\sqrt{s}$ variable is defined in the Appendix. In order to obtain meaningful result I left out the data points close to the dip from the fit procedure, which led to acceptable fits in case of the ISR data sets, but the interpretation of the TOTEM data remained unsatisfactory.

I have improved the BB model by adding a real part to its scattering amplitude, as a perturbative correction, which lead to non-vanishing elastic differential cross-section at the dip position [12]. The improved model gives a satisfactory description of the ISR data and a qualitatively improved but statistically not acceptable result at the LHC $\sqrt{s} = 7$ TeV data. I have found that the interpretation of the LHC data requires an increased real part in the elastic scattering amplitude, which is too large to be handled perturbatively.

To overcome the persisting disagreement between data and model description at the LHC energy of $\sqrt{s} = 7$ TeV, I have generalized the BB model using unitarity constraints by adding an arbitrarily large real part to its scattering amplitude in a systematic way [13]. Based on the good quality of the fit results, the improved model can be extrapolated to future LHC energies and beyond.

The structure of this PhD dissertation is as follows: in the remaining part of this chapter a terse overview of the LHC collider is provided in Section 1.1, followed by an elementary overview of diffractive hadronic physics in Section 1.2. The TOTEM experiment at the LHC is introduced in Section 1.3.

My LHC optics studies are reported in Chapter 2, which describes the mentioned new experimental method to determine the optics of the LHC accelerator at IP5, used by the TOTEM collaboration in many physics analysis.

My fit results using the BB model at ISR energies and at the LHC energy of $\sqrt{s} = 7$ TeV are explained in Chapter 3, while the perturbatively improved BB model is the

topic of Chapter 4. Chapter 5 presents the results obtained with the further improved BB model applying unitarity constraints.

The brief summary of my PhD research is the subject of Chapter 6. My research was supported by many people and organizations: I would like to thank their contribution in the Acknowledgments of Chapter 7. The Appendix defines the basic notations used throughout in my PhD thesis.

1.1 The Large Hadron Collider

The Large Hadron Collider (LHC) is currently the largest and most powerful particle collider of the world, which started its operation in 2008 [14]. The main goal of the accelerator is to test the Standard Model (SM) and search for new physics beyond the SM. I describe briefly the main design parameters of the LHC in Section 1.1.1 and the experiments at the LHC in Section 1.1.2.

1.1.1 The LHC accelerator

The schematic layout of the LHC particle collider is shown in Fig. 1.1. The LHC is built in the existing Large Electron Positron (LEP) tunnel with a circumference of 26.7 km. The tunnel is under the ground at a depth between 50 m and 100 m. The final, future, collision energy of the LHC is $\sqrt{s} = 14$ TeV, while the expected maximum collision energy is at $\sqrt{s} = 15$ TeV [14].

The particles are circulated in two beams at the LHC, clockwise in Beam 1 and counter-clockwise in Beam 2, see Fig. 1.1. The trajectory of the particles is defined by the accelerator magnets, which act similarly to an "optical" system characterized with a nominal betatron amplitude of $\beta^* = 0.55$ m, see also Chapter 2. The two beams circulate the particles in separated beam pipes, except at the four interaction points where Beam 1 and 2 cross each other, if dedicated dipole magnets bring them into collision. The interaction points are referred as IP1, IP2, IP5 and IP8, which host the experimental insertions indicated with stars in Fig. 1.1 [14].

The LHC uses other accelerators at CERN as a chain of injectors, including the Linac2, Proton Synchrotron Booster (PSB), Proton Synchrotron (PS) and Super Proton Syn-

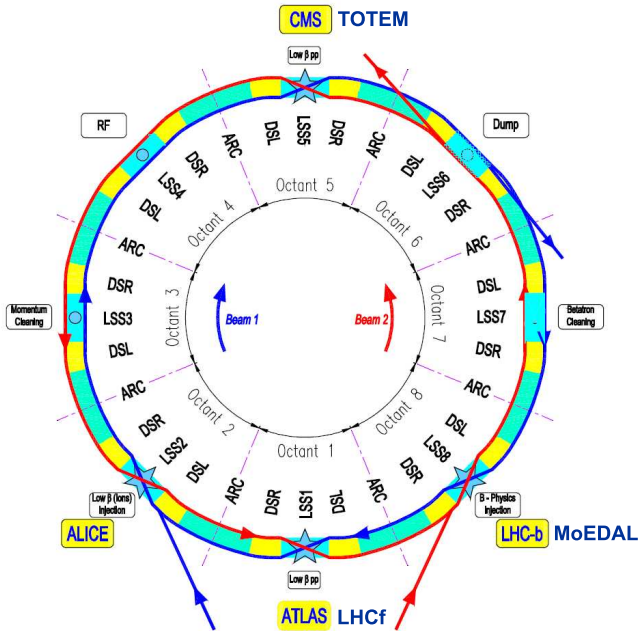

Figure 1.1: Schematic layout of the LHC. Beam 1 circulates the particles clockwise, while Beam 2 counter-clockwise. The four interaction points, IP1, IP2, IP5 and IP8, which host the experimental insertions are indicated with stars.

chrotron (SPS) accelerators. The particles are accelerated by the radio frequency (RF) high voltage system. The RF system is designed such that particle motion is confined longitudinally to a region called the RF bucket. Collection of particles captured within one RF bucket is called the particle bunch [14].

Nominally, there are $n_b = 2808$ number of bunches per beam with $N_b = 1.15 \times 10^{11}$ protons per bunch at the LHC [14]. The nominal value of the so-called normalized transverse emittance is $\varepsilon_N = 3.75\,\mu$m rad at the LHC, see Eq. (2.18) for details. The luminosity $\mathcal{L}$ is defined by the machine parameters, see also Eq. (2.19), and lead to an LHC peak luminosity of $\mathcal{L}_{\text{nom}} = 10^{34}$ cm^{-2}s^{-1} at IP5, which determines the reach of the LHC in terms of physics cross-sections, see also Eq. (1.3).

1.1.2 The experiments at the LHC

There are seven experiments at the LHC. The ATLAS (A Toroidal LHC ApparatuS), the CMS (Compact Muon Solenoid), the ALICE (A Large Ion Collider Experiment), LHCb (Large Hadron Collider beauty), LHCf (Large Hadron Collider forward), TOTEM

(TOTal Elastic and diffractive cross section Measurement) and the MoEDAL (Monopole and Exotics Detector at the LHC) experiment. The locations of the LHC experiments are illustrated in Figs. 1.2 and 1.1.

The ATLAS and CMS are general-purpose detectors, which can test the largest range of physics possible at the LHC. On 4 July 2012, after 4 years of successful operation, the ATLAS and CMS experiments announced a fundamental discovery, the observation of a new particle in the mass range of 126 GeV. The observed particle is consistent with the Higgs boson [15, 16], which particle plays a central role in the Standard Model.

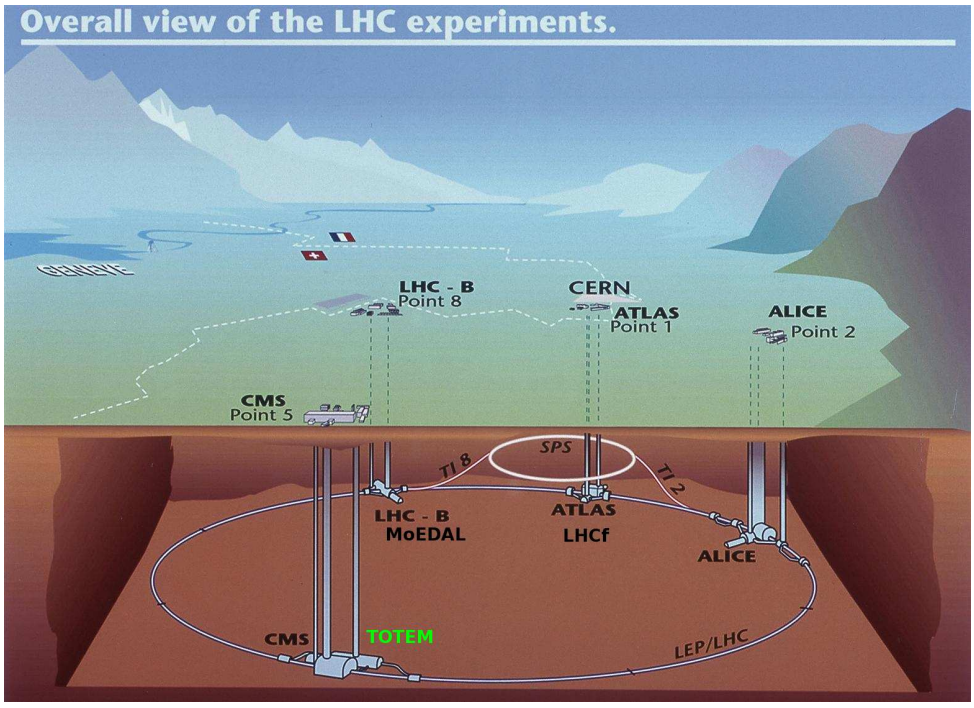

Figure 1.2: The locations of the 7 LHC experiments (ALICE, ATLAS, CMS, LHCb, LHCf, MoEDAL, TOTEM) [17]. The TOTEM experiment shares the IP5 with CMS.

The ALICE detector is specialized to study lead-ion collisions. It is designed to test the physics of strongly interacting matter at extreme energy densities, where the so-called strongly coupled quark-gluon plasma is formed. The LHCb experiment specializes to study the differences between matter and antimatter by studying the “b” quark. The LHCf studies forward particles to simulate cosmic rays in laboratory conditions. The main motivation of the MoEDAL experiment is to search directly for a hypothetical particle with magnetic charge: the magnetic monopole.

1.2 Overview of particle diffraction at high-energy

In this section a brief overview of particle diffraction is provided. If optical light is diffracted by an obstacle at small angles and at sufficiently large wave numbers k, the distribution of the intensity with the scattering angle ϑ can be approximated with [2]

$$I(\vartheta) \simeq I(0) \cdot (1 - B \cdot k^2 \vartheta^2)\,, \tag{1.1}$$

where $B \propto R^2$ (the square of the obstacle's radius, or of the hole in the screen), and $q \simeq k \cdot \vartheta$ is the momentum transfer. Hence, the intensity Eq. (1.1) shows a forward peak and a rapid decrease with increasing scattering angle ϑ.

Similar behavior can be observed in case of the cross-sections of diffractive hadronic processes; consider for example Fig. 5.8, which shows the recent pp elastic differential cross-section data measured by the TOTEM experiment at $\sqrt{s} = 7$ TeV. In general at small values of the four-momentum squared t ($|t| \propto \vartheta^2$ at high energies) the cross-section behave as [2]

$$\frac{\mathrm{d}\sigma}{\mathrm{d}t} = \left.\frac{\mathrm{d}\sigma}{\mathrm{d}t}\right|_{t=0} \cdot e^{-B\,|t|} \simeq \left.\frac{\mathrm{d}\sigma}{\mathrm{d}t}\right|_{t=0} \cdot (1 - B\,|t|)\,, \tag{1.2}$$

where the definition of the squared four-momentum t is given in the Appendix.

In case of hadronic processes the slope parameter B is proportional to the squared nuclear radius of the target hadron. The observed similarity between optical and hadronic diffractive phenomena can be transformed into a general definition in terms of pure particle physics: a reaction where no quantum numbers are exchanged between the colliding particles, at high energies, is a diffractive reaction [2].

The general definition of diffraction can be further classified as elastic, single diffractive, double diffractive, central diffractive ("double pomeron exchange") and higher order ("multi pomeron") processes [5], see also Fig. 1.3. Operationally, a diffractive reaction is characterized by a large, non exponentially suppressed, gap in rapidity $y = \frac{1}{2}\ln[(E + p_z)/(E - p_z)]$ in the final state, whose measurement is a challenging task in itself [1].

Since the 1960's the theoretical framework to describe hadronic diffraction is the so-called Regge-theory: the pioneering introduction of complex angular momenta, where hadronic reactions are described with the exchange of "objects" called reggeons. The

[1] A rapidity gap means an empty region in the rapidity distribution.

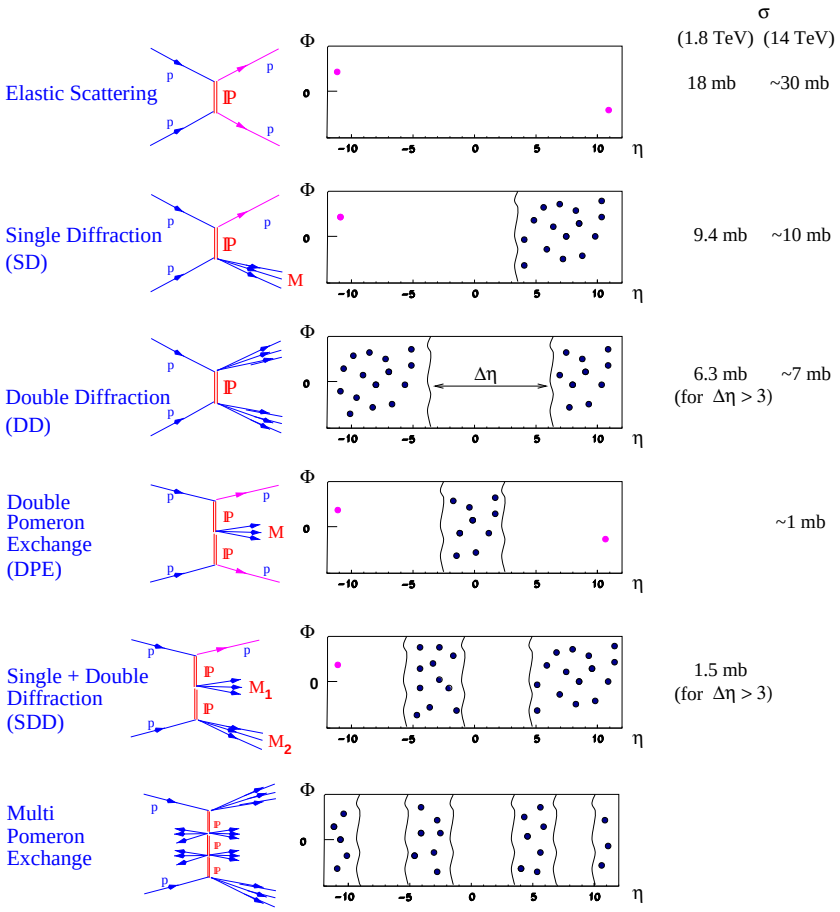

Figure 1.3: Classification of diffractive processes and their measured cross-sections at Tevatron and estimated for the LHC [5].

reggeon with vacuum quantum numbers which dominates asymptotically is the so-called *pomeron* [2].

In the 1960's the increase of the total pp cross-section was observed with increasing center-of-mass energy $\sqrt{s}$. This phenomenon has no classical optical analogy, since in case of classical electrodynamics the total cross-section is independent of the momentum of the scattered light, see Eq. (4.5). It is the exchange of intermediate particle states in QED, which leads to the increase of the total cross-section and exactly the same is the case in QCD, leading to the concept of the "expanding" proton [18–23], see also Fig. 5.10.

The optical analogy extends to pp elastic scattering, since the so-called "optical theorem" relates the total cross-section to the forward nuclear elastic scattering amplitude $T(s,t)|_{t=0}$, extrapolated to vanishing squared four-momentum transfer $t = 0$. At very low-$|t|$ the interference with the pp Coulomb interaction has to be carefully taken into

account in the model extrapolation [5].

1.3 The TOTEM experiment

The TOTEM experiment is dedicated to measure the total pp cross-section, elastic scattering and diffractive processes at the LHC at CERN. The experimental layout and the detector technologies are chosen in order to exploit efficiently the physics spectrum, briefly summarized in the previous Section 1.2. The main physics objective is the luminosity-independent measurement of the total pp cross-section, which relies on the determination of the nuclear inelastic rate N_{inel} [2, 5, 14]

$$\mathcal{L} \cdot \sigma_{\text{tot}} = N_{\text{tot}} = N_{\text{el}} + N_{\text{inel}} \,, \tag{1.3}$$

where $\mathcal{L}$ is the LHC luminosity, and on the "optical theorem" which relates the total cross-section to the nuclear elastic rate density function $\mathrm{d}N_{\text{el}}/\mathrm{d}t$ extrapolated to vanishing squared four-momentum transfer $t = 0$ [2, 5]

$$\mathcal{L} \cdot \sigma_{\text{tot}}^2 = \frac{16\pi}{1+\rho^2} \cdot \left.\frac{\mathrm{d}N_{\text{el}}}{\mathrm{d}t}\right|_{t=0} . \tag{1.4}$$

The total cross-section σ_{tot} can be expressed from Eqs. (1.3) and (1.4), without making use the luminosity $\mathcal{L}$. The parameter ρ, defined with Eq. (3.13), is taken from theoretical predictions or from extrapolations of other measurements [24]. Expression (1.4) is a simple consequence of Eqs. (3.11) and (3.12), as discussed later.

The reliable extrapolation of $\mathrm{d}N_{\text{el}}/\mathrm{d}t$ to $t = 0$ requires the measurement of protons with very small scattering angles. The TOTEM Roman Pot detectors, described in Section 1.3.1, fulfill this requirement. According to the general cross-section assumption Eq. (1.2) the nuclear inelastic rate N_{inel} is measured in the forward direction with the T1 and T2 inelastic detectors of the TOTEM experiment, described in Section 1.3.2.

The potential of the setup of the TOTEM experiment was demonstrated by several important measurements at the lower LHC energies of $\sqrt{s} = 7$ and 8 TeV. The total cross-section was measured at $\sqrt{s} = 7$ TeV and 8 TeV centre-of-mass energies by the TOTEM experiment with the luminosity-independent method [25, 26] and with other methods; at $\sqrt{s} = 7$ TeV the elastic σ_{el} and inelastic σ_{inel} cross-sections were also determined [25]. The forward charged particle pseudorapidity $\eta = -\ln\tan(\vartheta/2)$ density in pp collisions was

measured at $\sqrt{s} = 8$ TeV in the first common CMS-TOTEM measurement [27], which measurement was also done at $\sqrt{s} = 7$ TeV and 8 TeV by the TOTEM experiment itself independently, but limited to the forward rapidity range of the T1 and T2 detectors [28, 29]. The double diffractive cross-section in the very forward region was measured at $\sqrt{s} = 7$ TeV by the TOTEM experiment [30], while the challenging way of creating new resonances and new particles through central diffraction is under feasibility studies [5,31].

During the Long Shutdown 1 (LS1) the TOTEM experiment's layout has been upgraded substantially enlarging its physics potential [32–34]. In this PhD thesis only the experimental layout before LS1 is considered.

1.3.1 The Roman Pot detectors of the TOTEM experiment

The RPs are moveable beam-pipe insertions, which are able to approach the beam of the LHC through vacuum bellows in order to detect very forward protons [5,35]. The sensitive detectors are placed inside the secondary vacuum of the RP, see Fig. 1.5, which keeps them isolated from the LHC primary vacuum.[2] This innovative experimental technique was introduced at the ISR [36] and it has been successfully applied at other colliders like the S$\bar{p}p$S, TEVATRON, RHIC and HERA.

The RPs of the TOTEM experiment are organized into RP units, where each unit consists of three RPs: two of them approaches the outgoing beam vertically (top and bottom RPs) and another one horizontally. During data taking the horizontal RP detector overlaps with both vertical RP detectors, see Fig. 1.6. The overlap of the detector planes within a unit allows for the relative alignment of the 3 RPs with a precision of 10 μm by correlating the registered hit positions [37]. The horizontal alignment of the RPs with respect to the beam centre is based on proton tracks with low-ξ, while the vertical by matching the distributions of elastic protons. The final uncertainty of this procedure is less than 10 μm [35, 37].

The horizontal RP of the unit has yet another benefit: it approaches the beam center from the radially outer side of the beam, thus it completes the RP acceptance for diffractively scattered protons, see also Eq. (2.21) and Ref. [35].

[2]The experimental layout of the TOTEM experiment changed substantially during the LHC Long Shutdown 1 (LS1) [32, 33]. In this PhD thesis the layout before LS1 is considered.

Figure 1.4: Side view of a Roman Pot unit with two vertical (top and bottom) and one horizontal pot.

Figure 1.5: Roman Pot with the diamond shaped thin window and with the ferrite collar mounted around the housing on the beam vacuum side.

The RP units are organized into RP stations, where each station consists of two RP units, see Fig. 1.7. The two RP147 stations are centered at ±149.6 m from the IP5, while the two RP220 stations are centered at ±217.3 m [5][3]. The distance of the units in the RP220 stations is $\Delta s_{\text{units}} = 5.372\,\text{m}$. In a particular arm the units of station RP220 are abbreviated as "near" and "far" by means of their distance from IP5, see Fig. 2.2, which figure also explains the "left arm" and "right arm" abbreviations by means of the relative directions of the RPs with respect to the IP5. The long lever arm within a station, between the near and far units, has the advantage that local track angles are reconstructed with a precision of 5 to 10 μrad, which greatly helps to identify the background. The RPs can be arranged into so-called diagonals, where the top RPs in the left arm and the bottom RPs in the right arm form one diagonal; the other diagonal can be obtained by exchanging the top and bottom in the statement. The two diagonals are almost independent experiments [35].

Each RP hosts a stack of 10 planes of "edgeless" silicon strip detectors to detect leading protons scattered at very small angles, see Fig. 1.8. There are 512 strips on each silicon detector plane with a separation of 66 μm pitch distance. Half of the planes are oriented at an angle of +45° (5 planes), while the other half is oriented at −45° (5 planes) with respect to the detector edge which faces the beam. The (programmable) trigger requires

[3]Note, that the RP147 station was not used in actual data taking.

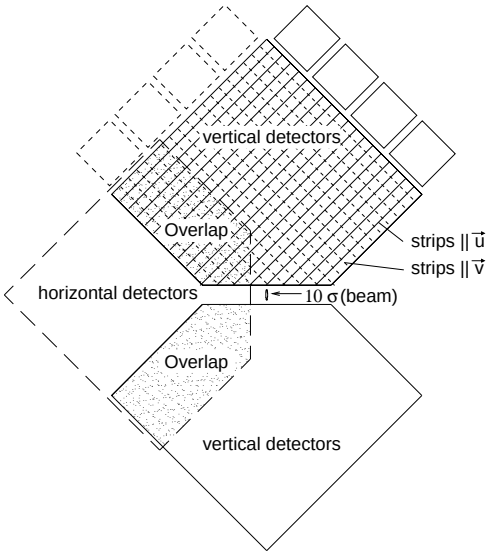

Figure 1.6: The overlap between the horizontal and vertical RP detectors of a RP unit.

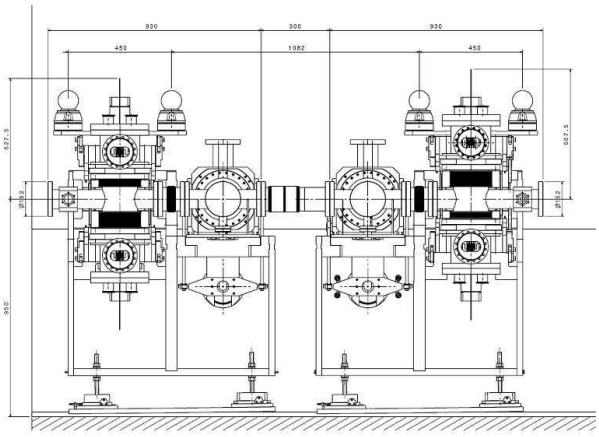

Figure 1.7: The design drawing of the RP147 Roman Pot station. The design of the other station, RP220, is identical except that the distance between the two units is larger.

collinear hits in at least three out of five planes for each projection, which significantly reduces the background. This radiation tolerant integrated trigger circuits are mounted on the detector. The alignment precision of the 10 mounted detector planes within a stack is of 20 μm [5, 35].

The movement of the RPs happens with step motors (5 μm step) and their precision is verified with inductive sensors with 10 μm precision.

The LHC beams are very thin, due to the high beam energy, consider Eqs. (2.15) and (2.18). Consequently, the detectors have to approach the beam to a distance as close as 1 mm and the silicon detectors have to remain efficient close to their mechanical edge.

This required the development of a so-called Planar Edgeless Detector with "Current Terminating Structure" (CTS) which includes an external "Current Terminating Ring" (CTR) guard ring, see Fig. 1.8. The CTR has the same potential bias as the device, hence it is able to collect the currents generated in the highly damaged region at the cut edge, preventing the diffusion of charges into the sensitive detector volume [5].

Figure 1.8: Planar Edgeless Detector with CTS (left). The magnification of a portion of the chip cut region (right) shows the details of the CTS.

The RP insertion has an integrated cooling system, which removes the thermal load from the sensors and the electronics.

1.3.2 The forward inelastic telescopes

According to Eqs. (1.3) and (1.4), the measurement of the inelastic rate N_{inel} is necessary for the luminosity-independent total cross-section determination [5]. Monte Carlo simulations showed that a detector coverage in the forward region is necessary for an efficient measurement of the inelastic rate, see also Eq. (1.2) about the distribution of diffractive processes in general. The apparatus of the TOTEM experiment consists of the T1 and T2 forward inelastic telescopes to measure the charged particles produced in inelastic collisions in order to determine N_{inel}.

The T1 inelastic telescope

The T1 forward tracking inelastic telescope of the TOTEM experiment takes place inside the endcaps of the CMS detector within two cone-shaped regions. It detects charged

particles covering the pseudorapidity range of $3.1 \leq |\eta| \leq 4.7$ [5]. The two arms of the T1 telescope are installed symmetrically with respect to the IP5 at a distance between 7.5 m and 10.5 m from the IP5, see Fig. 1.9.

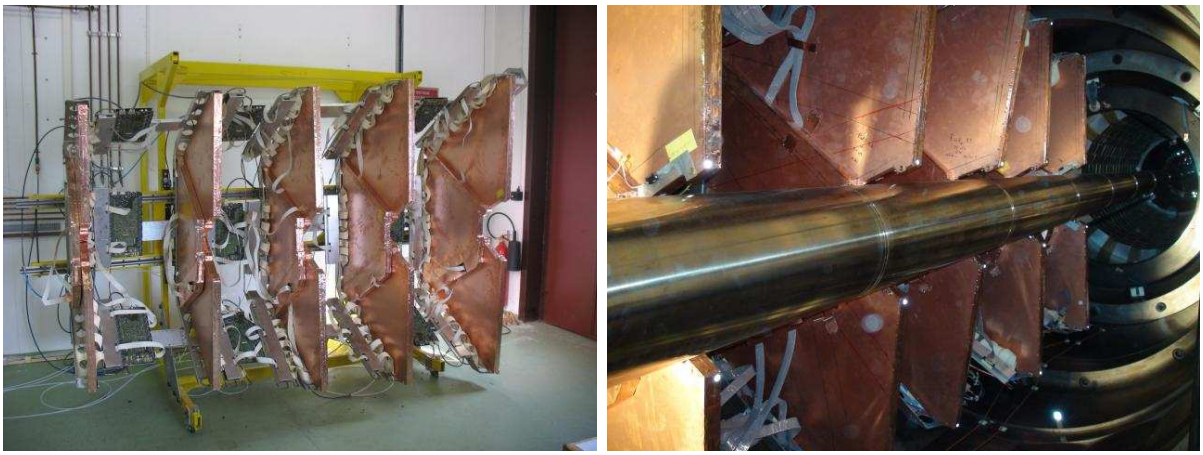

Figure 1.9: Half arm of the T1 forward telescope before (left) and after (right) installation inside the endcaps of the CMS detector.

The T1 detector and its inelastic trigger is of key importance for the measurement of the inelastic rate N_{inel}, which is part of the total pp cross-section measurement, see Eqs. (1.3) and (1.4). In order to distinguish the background (beam-gas interactions, beam muon-halo, etc.) from good beam-beam events with high efficiency the T1 detector has to have the capability to reconstruct the three coordinates of the primary vertex [5].

The T1 detector technology is the multiwire proportional chamber with segmented cathode read-out: the Cathode Strip Chamber (CSC), which meets with the above requirements. The CSC is a well understood technology. The CSC applies small material densities which is important as there are forward calorimeters behind the T1 telescope [5, 38].

Each arm of the T1 telescope consists of five planes with CSCs. The planes are placed equidistantly along the longitudinal axis of the detector and each arm is divided to two vertical halves to facilitate the installation around the vacuum chamber (Fig. 1.9).

A single detector plane of T1 is composed of six pieces of CSC wire chambers, where each CSC chamber covers approximately a ϕ region of 60°. Within one detector plane the neighboring CSC chambers overlap in ϕ in order to fully cover the geometrical area with sensitive detector surface. The detector sextants of each plane are slightly rotated with

respect to each other with an angular step of 3° to improve the pattern recognition step of the track reconstruction procedure [5].

The T2 inelastic telescope

The T2 detectors are placed at ±13.5 m on both sides of the IP5 [5]. The T2 inelastic telescopes detect charged particles in the pseudorapidity range of $5.3 \leq \eta \leq 6.5$. The generic requirements for the T2 detector are similar to the ones for T1 described in the previous section: it has to provide an inclusive trigger for diffractive events, an efficient reconstruction of the coordinates of the interaction vertex point in order to be able to discriminate the signal beam-beam events from the background, and it has to have a left-right symmetric alignment of the telescopes for better control of the systematic uncertainties [5].

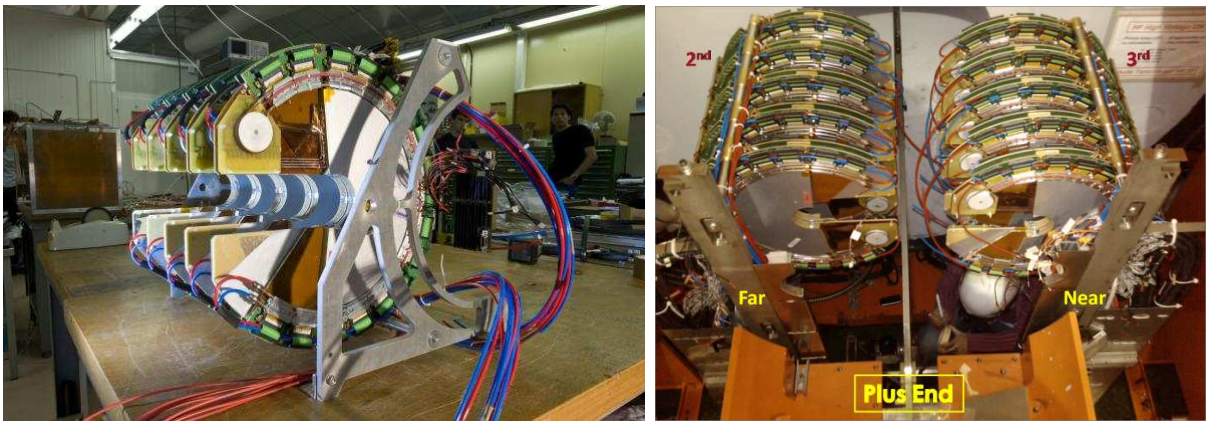

Figure 1.10: Half arm of the T2 detector (left) and the two halves of a single arm of the T2 detector before installation (right).

It is expected that the T2 telescope is able to work up to luminosities $\mathcal{L}$ of the order of 10^{33} cm^{-2}s^{-1} (close to $\mathcal{L}_{\text{nom}}$) where hard diffraction, heavy particle searches and physics beyond the SM could be probed [5, 31].

The T2 detector applies the gaseous electron multiplier (GEM) technology due to its high rate capability, good spatial resolution and robust mechanical structure [5]. The fill gas of the GEM is Ar/CO_2 with a mixture ratio of 70/30.

The T2 telescopes are installed in the forward shielding of CMS between the vacuum chamber and the inner shielding of the HF calorimeter. In each arm of T2, 20 pieces of

semi-circular GEM planes are installed. The GEMs are installed in pairs in a back-to-back configuration to form 10 detector planes of full azimuthal coverage, see Fig. 1.10 [5].

The shape of the GEM detector used in the T2 telescope is semi-circular with an active area covering an azimuthal angle of 192° and extending from radius $R_1 = 43$ mm up to $R_2 = 144$ mm from the beam axis. The front and back plates of the T2 GEM detector are 3 mm thick lightweight honeycomb structures. The drift electrode takes place on the front honeycomb plate. The electrode is followed by a 3 mm long drift space, where the three GEM foils are placed in a cascade, separated with a 2 mm charge transfer region. After the last GEM foil there is an induction gap of 2 mm space followed by the charge readout board installed on the back honeycomb plate of the GEM detector. The frames of the GEM foils contain also holes in two corners for a uniform distribution of the gas to the drift, transfer and induction gaps [5].

At the design value of the operating voltage, the gas amplification over all the three GEM foils is roughly 8000. The corresponding electrical field over the drift space is approximately 2.4 kV/cm, and 3.6 kV/cm over the transfer and induction gaps [5].

The readout board of T2 contains 2×256 concentric strips for the readout of the radial coordinates. The azimuthal coordinates are read with a matrix of 1560 pads. The pads take place under the strips isolated from each other with a layer of polyimide. The pads are divided into 65 radial sectors each containing 24 pads [5].

1.3.3 The electronics of the TOTEM experiment

The main requirement for the TOTEM electronics system is to provide the readout of the collected electrical charge for the three different detectors (RPs, T1 and T2 detectors) and maintain the full compatibility with the CMS experiment. In the TOTEM experiment the VFAT chip is the common front-end ASIC (Application-Specific Integrated Circuit), which provides the charge readout for all the TOTEM detectors and introduces the common data format and control mechanism [5].

The VFAT chip is designed to provide the trigger and tracking information at the LHC.

1.3.4 The TOTEM trigger system

The TOTEM trigger system is constructed on the basis of all TOTEM detectors [5]. The trigger mechanism depends on the targeted physics, on the machine luminosity $\mathcal{L}$, the run and background conditions as well. Coincidences between the different detectors on both sides of the intersection point reduce the background but as well can introduce certain biases. An important example is the measurement of the total cross-section, which requires triggers, as unbiased as possible, on all possible inelastic event topologies.

The TOTEM detectors actively create the first level trigger of the TOTEM experiment, where the read-out and trigger strategy is common to all detectors using the trigger bits generated by the VFAT chip. The Coincidence Chip (CC) provides on-detector coincidences to reduce the trigger data [5]. It is applied at the RP and T2 detectors, while in case of T1 due to the complex geometry of the detector it is not used. The CC chip has 80 inputs which are grouped in two ways: 16 groups of 5 inputs, for 5 silicon detector planes (RP case) and 8 groups of 10 inputs, for 10 detector planes (T2 case).

Chapter 2

LHC optics reconstruction using Roman Pots

2.1 Introduction

The TOTEM experiment at the LHC is optimized to measure elastic pp scattering at the LHC with the Roman Pot detectors, described in Section 1.3.1. Due to the very small scattering angle of the detected protons, observed by the near beam RP detectors, their trajectories are determined by the magnetic fields of the LHC accelerator magnet lattice, see Fig. 2.2. Therefore, the reconstruction of the kinematics of the scattered protons requires an accurate model of the LHC optics. The currently available so-called β-beating measurements with an uncertainty of $5 - 10$ % do not allow to estimate the optics model with the uncertainty, required by the TOTEM physics program [39, 40].

I have validated a new method of LHC optics determination for the TOTEM experiment. The method compares the measured information, obtained from angle-position distributions of elastically scattered protons observed in the RP detectors, with the LHC optics model, and tunes the transport model of the LHC within its nominal uncertainties until the LHC optics model calculations meet with the measured constraints. Theoretical predictions, as well as Monte Carlo studies, show that the residual uncertainty of the optics estimation method is smaller than 2.5 ‰. I have successfully applied the method to data samples recorded since 2010 [8, 9].

The outline of this chapter is as follows: the overview of the particular magnet lattice

of the LHC is the topic of Section 2.2, followed by a minimal and elementary accelerator theory part in Section 2.3, which is necessary to explain the method's theoretical background. After the introductory parts the description of the mentioned new method of LHC optics evaluation is provided in Section 2.4, where I discuss two representative LHC optics of betatron amplitudes $\beta^* = 3.5\,\mathrm{m}$ and $90\,\mathrm{m}$ [8, 9].

2.2 The LHC magnet system

The layout of the LHC accelerator follows the design of the 27 km long LEP tunnel, which contains eight arc and straight sections, see Fig. 1.1. In order to reuse the existing LEP tunnel in the most profitable way and also to drive the LHC cost-efficiently superconducting magnets, with a classical Nb-Ti technology, are heavily used in the LHC magnet lattice [14].

The arc sections of the LHC house the dipole magnets which bend the beams. In each arc of the LHC beam the magnets are organized into 23 *regular cells*, where each half-cell is 53.45 m long (Fig. 2.1). The half-cell contains three dipole magnets and one MQ quadrupole to focus or defocus the beam, according to the alternating focusing and defocusing quadrupoles of the Focus-Drift-Defocus-Drift (FODO) system [14].

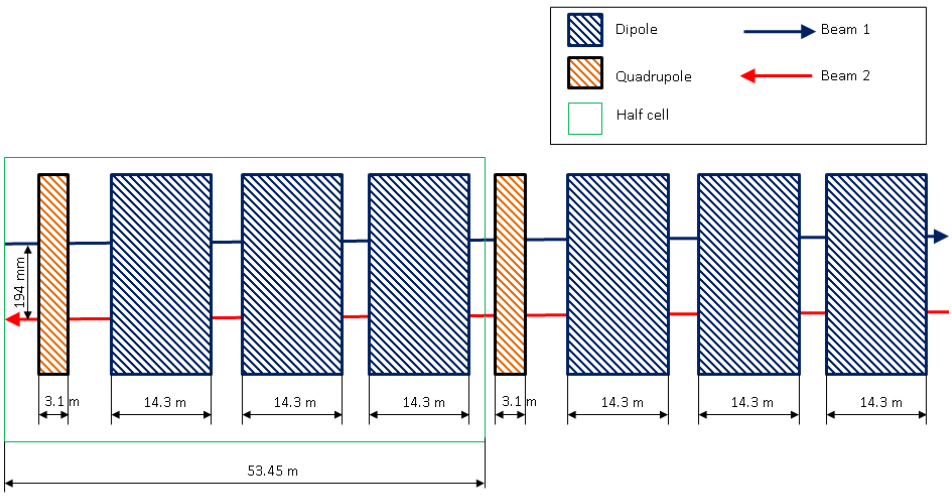

Figure 2.1: Schematic layout of one half-cell of the LHC.

At the LHC 1232 main dipole magnets are used for bending, which all share the same

design [14]. The overall length of a dipole is 16.5 m, the cold mass diameter is 570.0 mm at room temperature 293 K. The weight of one dipole is approximately 27.5 tons. These magnets are cooled down with superfluid helium to operate at a temperature of 1.9 K in order to achieve the required field strength of 8.33 T which provides a bending radius of 2803.98 m at 7 TeV beam energy [14].

The straight sections house the four experimental insertions, where the two beams cross each other [14]. The remaining four straight sections are utility insertions without beam crossing, see Fig. 1.1.

The nominal beam separation is 194 mm at the LHC. The separation dipole magnets D1 and D2 are used to change the nominal separation and bring together the beams onto a colliding orbit. D1 is a normal conducting magnet, MBXW, in case of high-luminosity insertions (IP1 and IP5) and superconducting magnet, MBX, at the ALICE and LHCb insertions. The D2 dipole, MBRC, is a twin-aperture superconducting magnet. The location of the separation dipole magnets at IP5 is shown in Fig. 2.2 with respect to the TOTEM experiment's RP detectors, described in Section 1.3.1.

The focusing and defocusing of the beam at the collision point is provided by the two inner triplet, one on each side of the collision point, see Fig. 1.1. One triplet is composed of four single-aperture quadrupoles. The two MQXA quadrupoles are 6.6 m long, developed by KEK, Japan. These are the Q1, Q3 parts of the triplet. The Q2 part contains two 5.7 m long MQXB quadrupoles, built by FNAL, USA. In total 16 MQXA and 16 MQXB magnets are used at the four experimental insertions [14].

The operating temperature of these quadrupoles is 1.9 K and their nominal gradient is 220 T/m. The MQY and MQML matching quadrupoles are also installed in each straight section.

Crossing angle

The number of bunches in the beam n_b is maximized in order to maximize the LHC luminosity $\mathcal{L}$. The bunches are so closely spaced that unwanted "parasitic" collisions occur. To keep this beam-beam effect as small as possible, a crossing-angle is introduced at each experimental insertion. In case of standard LHC runs, with betatron amplitude $\beta^* = 0.55$ m, a horizontal crossing angle of $+142.5\,\mu$rad is applied for Beam 1 at IP5

during collision, which is half of the total crossing angle [14]. The error of the crossing angle is determined by the error of the Beam Position Monitors (BPM).

Runs with dedicated $\beta^* = 90$ m optics have lower luminosity than the nominal $\mathcal{L}_{\text{nom}}$ with not more than 156 bunches, hence in this case the crossing-angle is zero; the same applies to the TOTEM-specific $\beta^* = 1540$ m future optics. In case of the $\beta^* = 3.5$ m optics the crossing angle is half of the $\beta^* = 0.55$ m one.

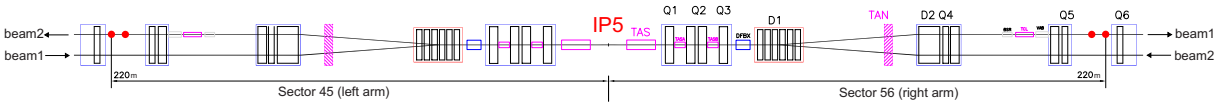

Figure 2.2: Schematic layout of the LHC magnet lattice at IP5 up to the RP220 RP station of the TOTEM experiment. The "near" and "far" RP units of the RP220 station are indicated with full (red) dots at the positions pointed by the black arrows. The figure also illustrates the key ingredients of the TOTEM experiment's "microscope" for the right arm: the inner triplet (Q1, Q2, Q3 superconducting quadrupoles) and the Q4 and Q5 quadrupoles are shown together with the D1 and D2 separation dipole magnets.

2.3 Description of particle transport

2.3.1 The closed orbit

The bending magnetic fields of an accelerator are usually vertically directed [41]. Therefore, the force acting on a charged particle due to the bending magnetic fields is horizontal

$$\vec{F} = e\,\vec{v} \times \vec{B}\,, \tag{2.1}$$

where e is the electrical charge and $\vec{v}$ is the velocity of the particle, respectively, and $\vec{B}$ describes the magnetic field.

If the bending magnetic fields of the accelerator were uniform everywhere, and the radiative corrections were small enough, the trajectory of the particle could be well approximated with a circle in the horizontal plane. In case of a non-uniform field one can define the local curvature $\rho(s)$ illustrated in Fig. 2.3.

The plane and the curvature of the trajectory is defined by the LHC bending magnets. The accelerator design is such that there is a particle trajectory with an ideal momentum

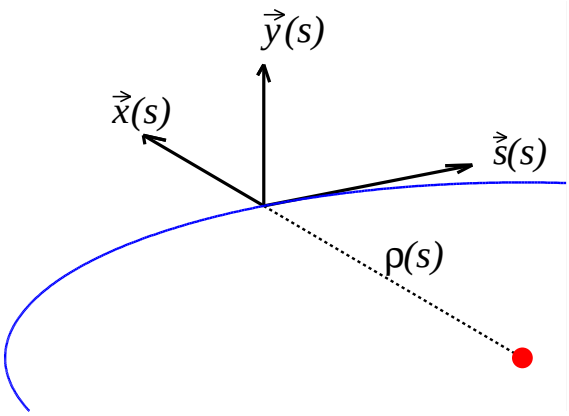

Figure 2.3: The local coordinate system of the closed orbit at position s. Charged particles with ideal momentum, placement and angle follow this orbit, with local curvature $\rho(s)$.

p_0 which closes on itself. We refer this orbit as the *closed orbit* of the central momentum particle [14, 41–43].

The description of particle motion can be given in a local coordinate system, see Fig. 2.3. There is a curved s-coordinate line which is aligned along the closed orbit. The horizontal x- and the vertical y-coordinate axes are perpendicular to the closed orbit, and the origin of the coordinate axes lies on the closed orbit. The positive x-coordinate axis is oriented outward from the accelerator center, while the positive y-coordinate axis points upward.

Charged particles with ideal momentum p_0 and position $x_0 = y_0 = 0$ follow the closed orbit. In reality, the bunch of particles enter into the LHC as a bundle of trajectories which shows a certain spread about the ideal orbit: the momentum of a particle may differ from the ideal one p_0. Also, at any instant the particle may have displacements and divergence angles both horizontally and vertically in the transverse (x, y) plane

$$\vartheta_x \approx x' = \frac{\mathrm{d}x}{\mathrm{d}s}\,,\ \vartheta_y \approx y' = \frac{\mathrm{d}y}{\mathrm{d}s}\,. \tag{2.2}$$

The alternating focusing-defocusing magnet system of the LHC is designed such that protons whose position deviates from the ideal one are restored back towards the closed orbit and, in total, the particles are forced to do so-called betatron oscillations around the closed orbit in the transverse plane. The influence of the transverse displacement and the relative momentum loss on the particle's trajectory is discussed in Sections 2.3.2 and 2.3.4, respectively.

2.3.2 Motion in the transverse plane

If a particle, which carries the elementary charge e, traverses a magnetic field $\vec{B}$ which is perpendicular to its velocity vector $\vec{v}$, the equation of particle motion is [41–43]

$$e\,\vec{v}\times\vec{B}=\frac{\mathrm{d}\vec{p}}{\mathrm{d}t}\,, \tag{2.3}$$

where $\vec{p}$ is the relativistic momentum vector of the particle.

The result of the cross product is perpendicular to the velocity vector $\vec{v}$ and consequently the particle trajectory is curved with radius ρ. Denote the length of this curved trajectory with s, where $s=\rho\,\vartheta$, then

$$\left|\frac{\mathrm{d}\vec{p}}{\mathrm{d}t}\right|=|\vec{p}|\,\frac{\mathrm{d}\vartheta}{\mathrm{d}t}=\frac{|\vec{p}|}{\rho}\frac{\mathrm{d}s}{\mathrm{d}t}\,. \tag{2.4}$$

The plane of motion and the magnetic field is assumed to be normal, hence the absolute value of the left hand side of the equation of motion Eq. (2.3) becomes

$$e\,\left|\vec{v}\times\vec{B}\right|=eB\frac{\mathrm{d}s}{\mathrm{d}t}\,, \tag{2.5}$$

where $B=|\vec{B}|$. The two results Eq. (2.4) and Eq. (2.5) must be equal, thus

$$eB\frac{\mathrm{d}s}{\mathrm{d}t}=\frac{|\vec{p}|}{\rho}\frac{\mathrm{d}s}{\mathrm{d}t}\,, \tag{2.6}$$

and after simplification one can define the so called *magnetic rigidity*

$$B\rho=\frac{p}{e}\,, \tag{2.7}$$

where $p=|\vec{p}|$.

2.3.3 Hill's equation

In order to describe momentum independently the strength of a given quadrupole magnet, its gradient has to be normalized with magnetic rigidity

$$k=\frac{1}{B\cdot\rho}\frac{\mathrm{d}B_y}{\mathrm{d}x}\,. \tag{2.8}$$

Suppose that a particle, which is displaced by a small x, passes through a short quadrupole with strength k and thickness $\mathrm{d}s$. The angular deflection is

$$\mathrm{d}x'\approx\mathrm{d}\vartheta_x=\frac{\mathrm{d}s}{\rho}\approx\frac{(\mathrm{d}B_y/\mathrm{d}x)\,x}{B\rho}\mathrm{d}s=kx\,\mathrm{d}s\,. \tag{2.9}$$

It follows from the last equation Eq. (2.9) that negative k focuses horizontally. The result Eq. (2.9) can be written as a second-order linear differential equation

$$x'' - k(s)x = 0\,, \tag{2.10}$$

with periodic coefficient function $k(s)$. This equation is known as Hill's equation [41, 44].

If the strength k is constant, the solution of Hill's equation Eq. (2.10) is the solution of the harmonic oscillator. The general solution can be found with the method of variation of integration constants, thus we use an ansatz with s dependent amplitude and phase

$$x(s) = \sqrt{\beta_x(s)\varepsilon}\cos\left[\phi_x(s) + \phi_0\right]\,, \tag{2.11}$$

where ε is a constant, β_x is the horizontal betatron amplitude function, and ϕ_x is the horizontal phase advance function of the oscillation. Note, that the $\sqrt{\beta_x(s)\varepsilon}$ function describes the envelope of the horizontal motion.

Differentiate the trial solution (2.11) with respect to s:

$$x'(s) = -\sqrt{\frac{\varepsilon}{\beta_x(s)}}\sin\left[\phi_x(s) + \phi_0\right] + \frac{\beta_x'(s)}{2}\sqrt{\frac{\varepsilon}{\beta_x(s)}}\cos\left[\phi_x(s) + \phi_0\right]\,. \tag{2.12}$$

The first derivative Eq. (2.12) and the second $x''(s)$ can be substituted back to Hill's equation (2.10), which leads to the following conditions [41–43]

$$\phi_x'(s) = \frac{1}{\beta_x(s)}\,, \tag{2.13}$$

and

$$\beta_x(s)\beta_x''(s) - \frac{1}{2}\beta_x'(s)^2 + 2k(s)\beta_x(s)^2 = 2\,. \tag{2.14}$$

At the positions s_m where $\beta_x'(s)\big|_{s=s_m} = 0$ the particles always fall to an ellipse in the (x, x') plane according to Eqs. (2.11) and (2.12) with semi-axis in the x-direction

$$\sigma(x) = \sqrt{\beta_x\varepsilon}\,, \tag{2.15}$$

while in the x'-direction Eq. (2.12) gives

$$\sigma(x') = \sqrt{\varepsilon\beta_x^{-1}}\,. \tag{2.16}$$

The area of the ellipse is thus constant

$$\pi\cdot\sigma(x)\cdot\sigma(x') = \pi\,\varepsilon\,, \tag{2.17}$$

which is the consequence of Liouville's theorem, and one can introduce ε as the so-called emittance of a beam of many particles. The emittance is a constant of the motion as long as the particle's energy is constant. In case of accelerating beam the normalized emittance is defined [41]

$$\varepsilon_N = (\beta_{\mathrm{L}} \cdot \gamma_{\mathrm{L}})\varepsilon\,,\ \beta_{\mathrm{L}} = \frac{v}{c}\,, \tag{2.18}$$

where v is the velocity of the particle, c is the speed of light and $\gamma_{\mathrm{L}} = (1-\beta_{\mathrm{L}}^2)^{-\frac{1}{2}}$ is the Lorentz factor. [1]

The quantity $\sigma(x)$, introduced in Eq. (2.15) is the so-called betatron beam size, as it does not include the component coming from the particles with momentum loss, discussed in the next Section.

The luminosity can be calculated for a beam with Gaussian transverse spatial distribution with [14, 41, 44]

$$\mathcal{L} = f \cdot n_{\mathrm{b}} \cdot \frac{N_{\mathrm{b}_1} N_{\mathrm{b}_2}}{4\pi\sigma_x^*\sigma_y^*}\,, \tag{2.19}$$

where f is the revolution frequency (11.2 kHz at LHC, determined by the circumference of the LEP tunnel), n_{b} is the number of bunches with N_{b_1} and N_{b_2} number of protons in Beam 1 and 2, respectively. $\sigma_{x,y}^*$ are the horizontal and vertical beam sizes, see Eq. (2.15), at the interaction point, respectively. Note, that in Eq. (2.19) the contribution of the crossing angle is not taken into account.

2.3.4 Orbit of low-momentum particles

Particles with momentum loss with respect to p_0

$$\Delta p = p - p_0\,, \tag{2.20}$$

will deviate from the closed orbit: according to the definition of the magnetic rigidity Eq. (2.7) if the particle losses momentum $\Delta p < 0$, the bending radius ρ becomes smaller, hence the particle is bent more at each dipole of the lattice.

The trajectory of a particle with slight momentum loss can be understood as a continuous deformation of the closed orbit, which preserves the topology and the trajectory

[1] The subscript "L" is used in β_{L} and γ_{L} to avoid confusion with the betatron amplitude function β and a γ function, which is introduced later in Eq. (3.32).

remains closed. Locally, it is the FODO system which compensates the extra bent and leads to the new closed orbit. The effect of the particle's momentum loss is similar to the effect of the gravity field on the trajectory, which effect is also compensated with a "suspension" coming from the extra focusing component of the FODO system [41].

The effect of the momentum-loss Δp combines together with the transverse motion described with Eq. (2.11). In total the horizontal coordinate of the transverse particle motion is described with

$$x(s) = \sqrt{\beta_x(s)\varepsilon}\cos\left[\phi_x(s) + \phi_{x,0}\right] + D_x(s)\xi, \;\; \xi = \frac{\Delta p}{p}\,, \tag{2.21}$$

where $D_x(s)$ is the horizontal dispersion function, which describes the horizontal "suspension" effect of the FODO system. In case of the LHC the vertical dispersion function vanishes $D_y(s) = 0$, since the bending fields are vertical and forces can act in the horizontal plane only.

According to Eq. (2.21) the width of the beam increases with increasing momentum spread. If one assumes that the momentum distribution of the beam is independent from the betatron oscillations the full beam size can be characterized with

$$\sigma_D(x) = \sqrt{\sigma(x)^2 + \left(D_x\frac{\sigma(p_0)}{p_0}\right)^2}\,, \tag{2.22}$$

where $\sigma(p_0)$ is the RMS of beam momentum spread.

2.3.5 Description of particle transport with matrices

The transport of particles from an initial position s_1 to another one s_2 can be described with matrices, which formalism is similar to the description of light ray propagation in optics through a system of optical lenses, collimators and drift spaces. The matrix description is a general consequence of the linearity of Hill's differential equation Eq. (2.10).

In the horizontal plane the propagation can be written with the help of a 2×2 matrix M_{21}, the transport matrix

$$\begin{pmatrix} x(s_2) \\ x'(s_2) \end{pmatrix} = M_{21}\begin{pmatrix} x(s_1) \\ x'(s_1) \end{pmatrix}\,. \tag{2.23}$$

In the particular case, when the particle passes through a drift space with length l, the motion is described with the linear equations

$$x(s_2) = x(s_1) + x'(s_1) \cdot l\,, \tag{2.24}$$
$$x'(s_2) = x'(s_1)\,,$$

which can be transformed into the form of matrix equation Eq. (2.23) with the matrix

$$M_{\text{drift}} = \begin{pmatrix} 1 & l \\ 0 & 1 \end{pmatrix}. \tag{2.25}$$

The particle transport through a thin quadrupole magnet, with strength k and length l, can be described with the matrix [41]

$$M_{\text{quad}} = \begin{pmatrix} 1 & 0 \\ -kl & 1 \end{pmatrix}. \tag{2.26}$$

The effect of each particular element of the magnet lattice may be expressed by a matrix M_i. Finally, one can trace particles over a whole section of the lattice by simply forming the product of the elementary lattice element matrices

$$T(s, s_0) = M_1 \cdot M_2 \cdot ... \cdot M_n\,. \tag{2.27}$$

2.4 The LHC optics between IP5 and the RPs

In case of the LHC accelerator, the scattered protons are detected by the Roman Pots after having traversed a segment of the LHC lattice containing 29 main and corrector magnets per beam, see Fig. 2.2. The trajectory of protons produced with transverse positions[2] (x^*, y^*) and angles $(\vartheta_x^*, \vartheta_y^*)$ at IP5 is described approximately by a linear formula

$$\vec{d} = T \cdot \vec{d^*}\,, \tag{2.28}$$

where $\vec{d} = (x, \vartheta_x, y, \vartheta_y, \xi)^T$. The single pass transport matrix

$$T = \begin{pmatrix} v_x & L_x & m_{13} & m_{14} & D_x \\ \frac{\mathrm{d}v_x}{\mathrm{d}s} & \frac{\mathrm{d}L_x}{\mathrm{d}s} & m_{23} & m_{24} & \frac{\mathrm{d}D_x}{\mathrm{d}s} \\ m_{31} & m_{32} & v_y & L_y & D_y \\ m_{41} & m_{42} & \frac{\mathrm{d}v_y}{\mathrm{d}s} & \frac{\mathrm{d}L_y}{\mathrm{d}s} & \frac{\mathrm{d}D_y}{\mathrm{d}s} \\ 0 & 0 & 0 & 0 & 1 \end{pmatrix} \tag{2.29}$$

[2]The '*' superscript indicates the LHC Interaction Point 5

is defined by the optical functions [42, 43]. The transport equation Eq. (2.28) is the straightforward generalization of the two-dimensional case of Eq. (2.23), which includes the description of low-momentum particles using the dispersion $D_{x,y}$ functions, see Eq. (2.21).

The horizontal and vertical magnifications

$$v_{x,y} = \sqrt{\beta_{x,y}/\beta^*}\cos\Delta\mu_{x,y} \tag{2.30}$$

and the effective lengths

$$L_{x,y} = \sqrt{\beta_{x,y}\beta^*}\sin\Delta\mu_{x,y} \tag{2.31}$$

are of particular importance for proton kinematics reconstruction, where the horizontal and vertical relative phase advances

$$\Delta\mu_{x,y} = \int_{\mathrm{IP}}^{\mathrm{RP}} \frac{\mathrm{d}s}{\beta(s)_{x,y}} \tag{2.32}$$

are determined by the horizontal and vertical betatron amplitudes $\beta_{x,y}$, according to Eq. (2.13).

In case of the LHC nominal optics the coupling coefficients of the transport matrix Eq. (2.29) are, by design, equal to zero

$$m_{13}, ..., m_{42} = 0\,. \tag{2.33}$$

Also for elastically scattered protons the interaction related contribution to longitudinal momentum loss ξ is 0. However, the beam protons are characterized by a momentum spread resulting from the beam longitudinal emittance and the RF configuration. For the LHC this spread is $\delta p/p_0 = 10^{-4}$ [14], which is not significant with respect to the beam momentum offset uncertainty of 10^{-3}, reported in Table 2.1. Therefore, the terms $D_{x,y}\cdot\xi$ and $\mathrm{d}D_{x,y}/\mathrm{d}s\cdot\xi$ of the transport equation Eq. (2.28) can be neglected in case of elastically scattered protons.

Furthermore, the horizontal phase advance $\Delta\mu_x$ is equal to π at 219.59 m (see Fig. 2.4), and consequently the horizontal effective length L_x vanishes close to the far RP unit, as it is shown in Fig. 2.6. Therefore, in the proton kinematics reconstruction $\mathrm{d}L_x/\mathrm{d}s$ is used.

Note, that each optical function is a complicated and non-linear function of the proton's relative momentum loss ξ, according to the transport equation Eq. (2.28); not the subject of this thesis, where $\xi = 0$ is always assumed. Comprehensive LHC beam optics studies, concerning the case of non vanishing ξ, can be found in Ref. [45].

2.4.1 Proton's kinematics reconstruction

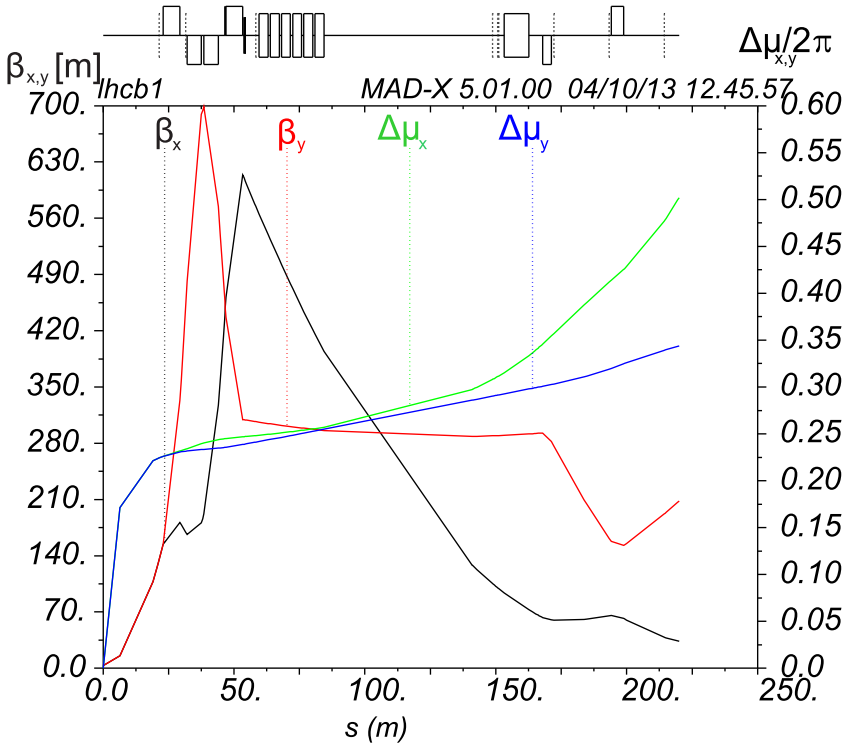

Figure 2.4: The evolution of the horizontal β_x and vertical betatron amplitude β_y between IP5 and the location of the Roman Pot stations for the LHC $\beta^* = 3.5$ m optics. The horizontal μ_x and vertical phase advance μ_y are also shown, these functions are normalized to 2π. The plot shows that the horizontal phase advance $\Delta\mu_x = \pi$ close to the far RP unit. The figure has been obtained with the MAD-X code of version 5.01.00 [46].

The kinematics of elastically scattered protons at IP5 can be reconstructed on the basis of RP proton tracks using the transport equation Eq. (2.28). Suppose, that the coupling coefficients in the transport matrix Eq. (2.29) vanish, $m_{ij} = 0$, and the proton's momentum loss is zero $\xi = 0$. In this case the transport equation Eq. (2.28) dictates that the proton's horizontal coordinate and horizontal scattering angle at a given location are

$$\begin{aligned} x &= v_x \cdot x^* + L_x \cdot \vartheta_x^* \,, \\ \vartheta_x &= \frac{\mathrm{d}v_x}{\mathrm{d}s} x^* + \frac{\mathrm{d}L_x}{\mathrm{d}s} \vartheta_x^* \,, \end{aligned} \tag{2.34}$$

where each optical function is a function of the initial and final location s along the beam line, according to Eq. (2.32). The corresponding equations in the vertical y-plane can be obtained from Eqs. (2.34) by replacing x with y.

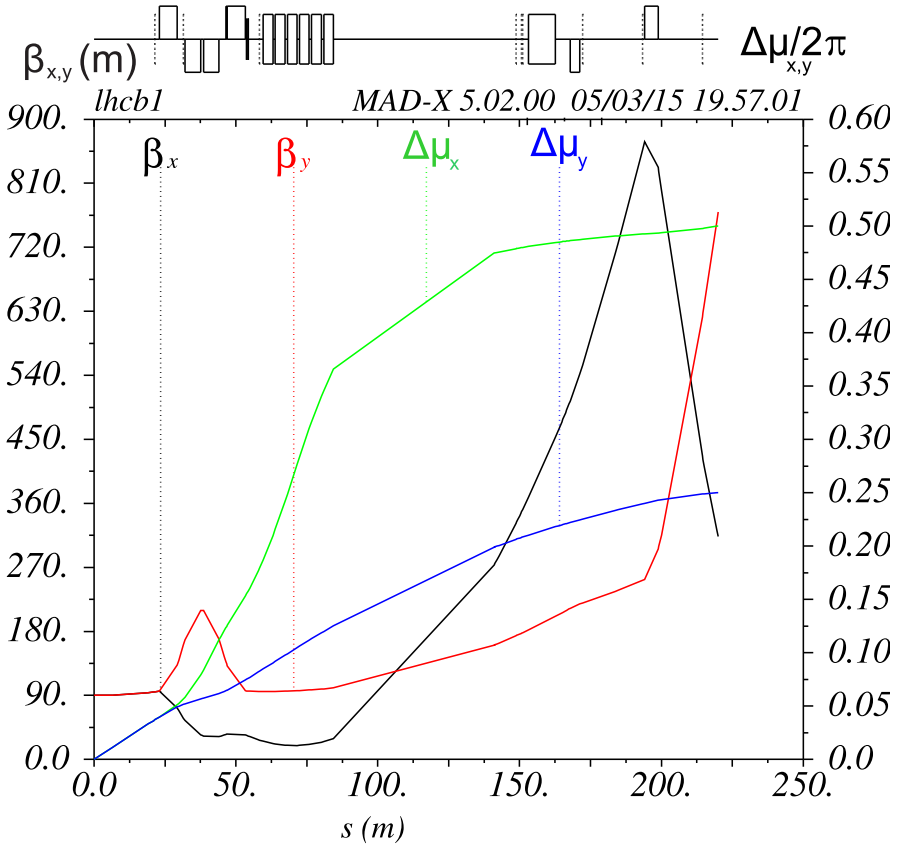

Figure 2.5: The evolution of the horizontal β_x and vertical betatron amplitude β_y between IP5 and the location of the Roman Pot stations for the LHC $\beta^* = 90$ m optics. The horizontal μ_x and vertical phase advance μ_y are also shown, these functions are normalized to 2π. The plot shows that the horizontal and vertical phase advance $\Delta\mu_x = \pi$ and $\Delta\mu_y = \pi/2$ close to the far RP unit.

The proton's horizontal coordinate at the location of the "near" RP unit can be explicitly written

$$x_{\text{near}} = v_{x,\text{near}} \cdot x^* + L_{x,\text{near}} \cdot \vartheta_x^* \,, \tag{2.35}$$

and the same applies to the "far" RP unit. These two equations can be inverted

$$x^* = \frac{L_{x,\text{far}} \cdot x_{\text{near}} - L_{x,\text{near}} \cdot x_{\text{far}}}{D} \,, \tag{2.36}$$

$$\vartheta_x^* = \frac{v_{\text{x,near}} \cdot x_{\text{far}} - v_{x,\text{far}} \cdot x_{\text{near}}}{D} \,. \tag{2.37}$$

if the determinant $D = (v_{x,\text{near}} \cdot L_{x,\text{far}} - v_{x,\text{far}} \cdot L_{x,\text{near}})$ does not not vanish; the equations in the vertical plane can be obtained as before, by replacing x with y.

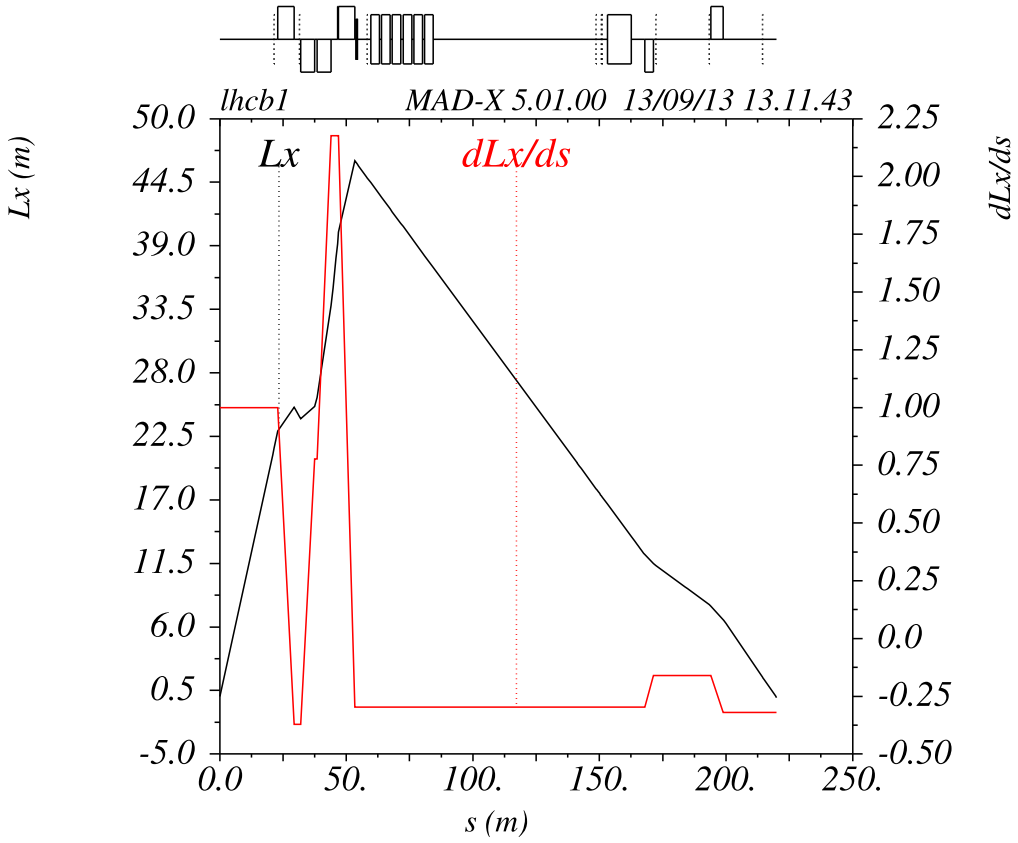

Figure 2.6: The evolution of the horizontal effective length L_x and its derivative $\mathrm{d}L_x/\mathrm{d}s$ between IP5 and the location of the Roman Pot stations in case of the LHC $\beta^* = 3.5$ m optics. The plot indicates that $L_x = 0$ close to the far RP unit, thus in the proton kinematics reconstruction $\mathrm{d}L_x/\mathrm{d}s$ is used instead of L_x.

The reconstruction formula of the scattering angle Eq. (2.37) can be rearranged into a more readable form

$$\vartheta_x^* = \frac{1}{\frac{\mathrm{d}L_x}{\mathrm{d}s}} \left(\vartheta_x - \frac{\mathrm{d}v_x}{\mathrm{d}s} x^* \right) , \tag{2.38}$$

where the derivative of the horizontal effective length is used in the form

$$\frac{\mathrm{d}L_x}{\mathrm{d}s} = \frac{L_{x,\mathrm{far}} - L_{x,\mathrm{near}}}{s_{\mathrm{far}} - s_{\mathrm{near}}} , \tag{2.39}$$

since there is no magnetic field present between the two RP units; the same applies to the derivative of the horizontal magnification $\mathrm{d}v_x/\mathrm{d}s$.

The rearranged formula Eq. (2.38) clearly shows how the contribution of the horizontal vertex distribution x^* is removed when the scattering angles are calculated. Due to $\Delta\mu_x = \pi$ (Figs. 2.4 and 2.5) the horizontal effective length vanishes $L_x = 0$ close to the

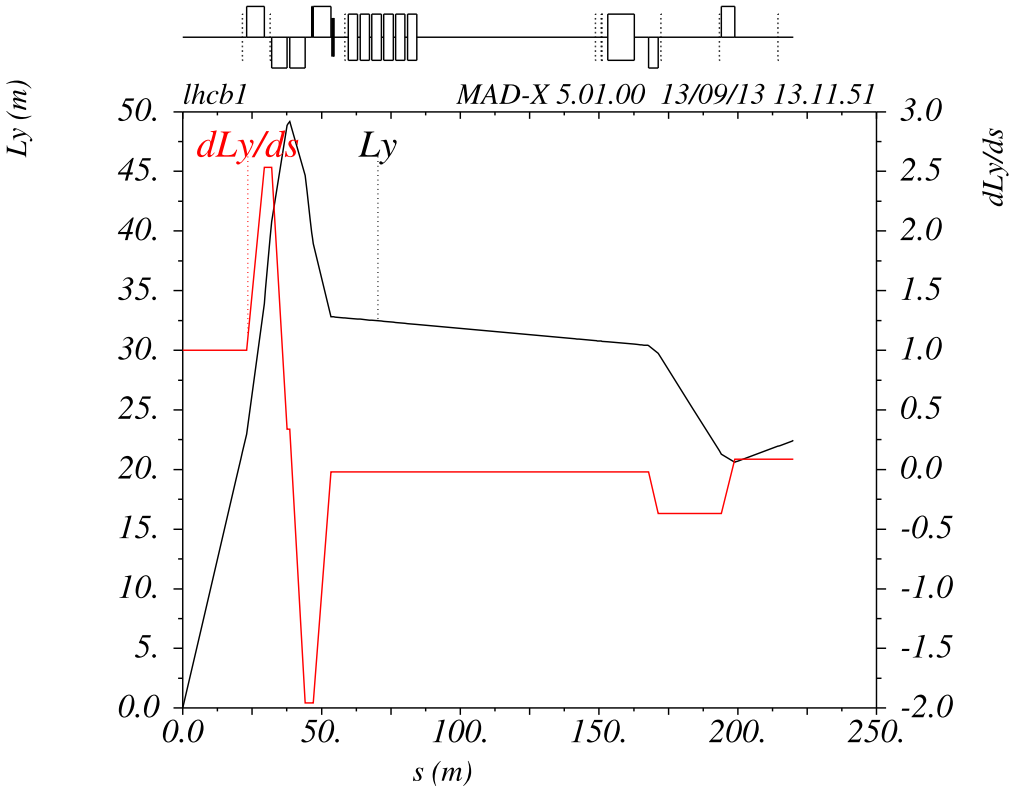

Figure 2.7: The evolution of the vertical effective length L_y and its derivative $\mathrm{d}L_y/\mathrm{d}s$ between IP5 and the location of the Roman Pot stations for the LHC $\beta^* = 3.5$ m optics.

far RP unit (Fig. 2.6), thus in the proton kinematics reconstruction the use of $\mathrm{d}L_x/\mathrm{d}s$ is preferred using Eq. (2.38).

According to Eq. (2.15) the transverse vertex size σ_y^* is small in case of the $\beta^* = 3.5\,\mathrm{m}$ optics, while the $\beta^* = 90\,\mathrm{m}$ optics has a vertical phase advance of $\Delta\mu_y = \pi/2$ close to the RP units, see Fig. 2.5. Thus, it follows from Eq. (2.30) that the vertical magnification v_y vanishes, see also Fig. 2.8. Therefore, in case of the two analyzed representative optics $\beta^* = 3.5\,\mathrm{m}$ and $90\,\mathrm{m}$, the vertical effective length L_y is large enough to simplify the transport formula in the vertical plane at each RP unit

$$y_{\mathrm{near}} \approx L_{y,\mathrm{near}} \cdot \vartheta_y^*\,, \quad y_{\mathrm{far}} \approx L_{y,\mathrm{far}} \cdot \vartheta_y^*\,, \tag{2.40}$$

which has to be compared with the horizontal case of Eq. (2.35).

Finally, the vertical scattering angle at the interaction point is reconstructed as the average of the near and far RP unit measurements

$$\vartheta_y^* \approx \frac{1}{2}\left(\frac{y_{\mathrm{near}}}{L_{y,\mathrm{near}}} + \frac{y_{\mathrm{far}}}{L_{y,\mathrm{far}}}\right)\,. \tag{2.41}$$

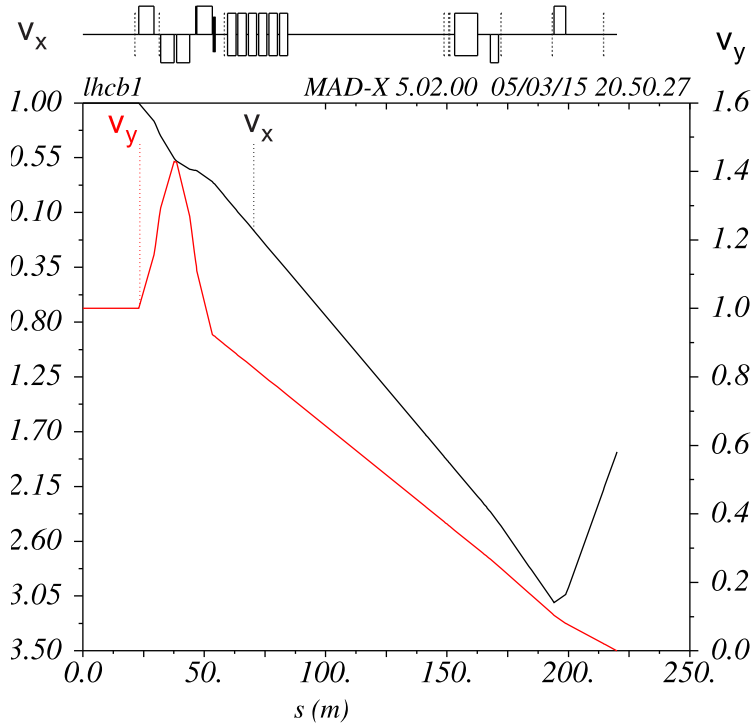

Figure 2.8: The evolution of the horizontal v_x and vertical magnification v_y in case of the LHC $\beta^* = 90$ m optics between IP5 and the location of the Roman Pot stations. Figure 2.5 shows that the vertical phase advance $\Delta\mu_y = \pi/2$ close to the far RP unit and according to Eq. (2.30) the vertical magnification v_y vanishes.

Elastic scattering events consist of two anti-parallel protons, detected with the RPs installed at Beam 1 and 2. The horizontal and vertical scattering angles of both protons are reconstructed with the use of Eqs. (2.38) and (2.41) and the results are averaged

$$\vartheta_x^* = \frac{1}{2}\left(\vartheta_{x,b_1}^* + \vartheta_{x,b_2}^*\right) , \quad \vartheta_y^* = \frac{1}{2}\left(\vartheta_{y,b_1}^* + \vartheta_{y,b_2}^*\right) , \tag{2.42}$$

where the subscripts b_1 and b_2 indicate Beam 1 and 2, respectively.

The squared four-momentum transfer t, defined with Eq. (A.2), of the elastic scattering pp process can be thus reconstructed

$$t \approx -p_0^2 \left(\vartheta_x^{*2} + \vartheta_y^{*2}\right) , \tag{2.43}$$

where Eq. (A.13) was applied [37, 45].

As the values of the reconstructed angles are inversely proportional to the optical functions, consider Eqs. (2.38) and (2.41), the errors of the optical functions have to be determined to estimate their contribution into the systematic errors of the final physics results.

2.4.2 Proton transport model at the LHC

The proton transport matrix $T(s;\mathcal{M})$, calculated with MAD-X [46], is defined by the machine settings $\mathcal{M}$, which are obtained on the basis of several data sources. The version V6.5 of the LHC sequence is used to describe the magnet lattice, while the nominal magnet strength file for a given beam optics is always updated using measured data: the currents of the magnet's power converters are first retrieved using TIMBER [47], which is an application to extract data from heterogeneous databases containing information about the whole LHC infrastructure.

First of all, for a given data taking period, the measured currents of the magnets' power converters I_{PC} are retrieved from the TIMBER database [47]. Then, the currents are converted to magnet strengths with the LHC Software Architecture (LSA) [48] which employs for this purpose the conversion curves described by the Field Description for the LHC (FIDEL) [49].

Through the WISE (Windows Interface to Simulation of Errors) interface [50] one has access to the database of the measured LHC imperfections (field harmonics, magnets displacement, rotations) included in $\mathcal{M}$, as well as statistical models describing the non-measured parameters' tolerances. Alignment uncertainties of the magnets are included into WISE based on measurements of the mechanical and magnetic axes. Other uncertainties for example relative and absolute measurement errors of hysteresis and power converters accuracy are also included for all magnets.

2.5 Machine imperfections

The real LHC machine [51] is subject to additional imperfections $\Delta\mathcal{M}$, not measured well enough so far, which alter the transport matrix by ΔT:

$$T\,(s;\,\mathcal{M}) \to T\,(s;\,\mathcal{M}+\Delta\mathcal{M}) = T\,(s;\,\mathcal{M}) + \Delta T. \tag{2.44}$$

The most important are [14, 52–55]:

- magnet current–strength conversion error: $\sigma(k)/k \approx 10^{-3}$
- beam momentum offset: $\sigma(p)/p \approx 10^{-3}$.

Their impact on the most relevant optical functions L_y and $\mathrm{d}L_x/\mathrm{d}s$ can be calculated with MAD-X, the results are presented in Table 2.1. It is clearly visible that the imperfections of the inner triplet (the so called MQXA and MQXB magnets) are of high influence on the transport matrix while the optics is less sensitive to the strength of the quadrupoles MQY and MQML.

Other imperfections that are of lower, but not negligible, significance:

- magnet rotations: $\delta\phi \approx 1$ mrad
- beam harmonics: $\delta B/B \approx 10^{-4}$
- power converter errors: $\delta I/I \approx 10^{-4}$
- magnet positions: $\delta x, \delta y \approx 100\,\mu$m.

Generally, as indicated in Table 2.1 and 2.2, the low-β^* optics sensitivity to the machine imperfections is significant and cannot be neglected. For high-β^* optics the magnitude of ΔT is smaller in the vertical plane but in the horizontal plane the $\beta^* = 3.5$ m and $\beta^* = 90$ m optics result is similar. Due to the sensitivity of L_x the $\beta^* = 90$ m optics is also investigated in the following sections.

The proton reconstruction is based on Eqs. (2.36) and (2.38). Thus it is necessary to know the effective lengths $L_{x,y}$ and their derivatives with an uncertainty better than 1–2 % in order to measure the total cross-section σ_{tot} with the aimed uncertainty of [56]. The currently available $\Delta\beta/\beta$ beating measurement with an error of $5-10$ % does not allow to estimate ΔT with the uncertainty, required by the TOTEM physics program [39, 40].

	$\delta L_{y,b_1,\text{far}}/L_{y,b_1,\text{far}}$ [%]		$\delta\left(\frac{\mathrm{d}L_{x,b_1}}{\mathrm{d}s}\right)/\frac{\mathrm{d}L_{x,b_1}}{\mathrm{d}s}$ [%]	
Perturbed element	$\beta^* = 3.5\,m$	$\beta^* = 90\,m$	$\beta^* = 3.5\,m$	$\beta^* = 90\,m$
MQXA.1R5	0.98	0.14	−0.46	−0.42
MQXB.A2R5	−2.24	−0.24	0.33	0.31
MQXB.B2R5	−2.42	−0.25	0.45	0.42
MQXA.3R5	1.45	0.20	−1.14	−1.08
MQY.4R5.B1	−0.10	−0.01	−0.02	0.00
MQML.5R5.B1	0.05	0.04	0.05	0.06
$\Delta \mathrm{p}_{b_1}/\mathrm{p}_{b_1}$	−2.19	0.01	−0.79	0.71
$\Delta\phi_{\text{quadrupoles}}$	0.01	$3 \cdot 10^{-3}$	0.01	0.01
$(\Delta x, \Delta y)_{\text{quadrupoles}}$	$6 \cdot 10^{-6}$	$1 \cdot 10^{-5}$	$3 \cdot 10^{-5}$	$2 \cdot 10^{-5}$
Total sensitivity	4.33	0.43	1.57	1.46

Table 2.1: Sensitivity of the vertical effective length L_{y,b_1} and $\mathrm{d}L_{x,b_1}/\mathrm{d}s$ to 1 ‰ deviations of magnet strengths or beam momentum for low- and high-β^* optics of the LHC Beam 1. The total sensitivity to the perturbations of the quadrupole magnets' transverse position ($\Delta x, \Delta y = 1$ mm) and rotation ($\Delta\phi = 1$ mrad) is also included. The subscript b_1 indicates Beam 1.

However, as it is shown in the following sections, ΔT can be determined well enough from the proton tracks in the Roman Pots, by exploiting the properties of the optics and those of the elastic *pp* scattering.

2.6 Correlations in the transport matrix

The transport matrix T defining the proton transport from IP5 to the RPs is a product of matrices describing the magnetic field of the lattice elements along the proton trajectory, see Eq. (2.27). The imperfections of the individual magnets alter the cumulative transport function. It turns out that independently of the origin of the imperfection (strength of any of the magnets, beam momentum offset) the transport matrix is altered in a similar

	$\delta L_{y,b_1,\text{far}}/L_{y,b_1,\text{far}}$ [%]	
Perturbed element	$\beta^* = 11\,m$	$\beta^* = 1000\,m$
MQXA.1R5	0.99	0.08
MQXB.A2R5	−2.24	−0.14
MQXB.B2R5	−2.43	−0.15
MQXA.3R5	1.48	0.14
MQY.4R5.B1	−0.25	$-4.1 \cdot 10^{-3}$
MQML.5R5.B1	0.08	0.04
$\Delta p_{b_1}/p_{b_1}$	2.27	−0.06
Total sensitivity	4.39	0.23

Table 2.2: Sensitivity of the vertical effective length L_y to 1 ‰ deviations of magnet strengths and beam momentum for the $\beta^* = 11$ m and $\beta^* = 1000$ m optics to be compared with Table 2.1. Only the most important contributions are summarized.

way, as can be described quantitatively with eigenvector decomposition, discussed in Section 2.6.1.

2.6.1 Correlation matrix of imperfections

Assuming that the imperfections discussed in Section 2.5 are independent, the covariance matrix describing the relations among the errors of the optical functions can be calculated:

$$V = \text{Cov}(\Delta T_r) = E\left(\Delta T_r \Delta T_r^T\right), \tag{2.45}$$

where T_r is the most relevant 8-dimensional subset of the transport matrix

$$T_r^{\text{T}} = (v_x, L_x, \frac{\mathrm{d}v_x}{\mathrm{d}s}, \frac{\mathrm{d}L_x}{\mathrm{d}s}, v_y, L_y, \frac{\mathrm{d}v_y}{\mathrm{d}s}, \frac{\mathrm{d}L_y}{\mathrm{d}s}), \tag{2.46}$$

which is presented as a vector for simplicity.

The optical functions contained in T_r differ by orders of magnitude and, are expressed in different physical units. Therefore, a normalization of V is necessary and the use of the correlation matrix C, defined as

$$C_{i,j} = \frac{V_{i,j}}{\sqrt{V_{i,i} \cdot V_{j,j}}}, \tag{2.47}$$

is preferred. An identical behavior of uncertainties for both beams was observed and therefore it is enough to study the Beam 1. In case of the $\beta^* = 3.5\,\mathrm{m}$ optics the following error correlation matrix is obtained using the MAD-X results of Section 2.5:

$$C = \begin{pmatrix} 1.00 & 0.74 & -0.42 & -0.80 & -0.51 & -0.46 & -0.61 & -0.44 \\ 0.74 & 1.00 & -0.63 & -1.00 & -0.25 & -0.30 & -0.32 & -0.29 \\ -0.42 & -0.63 & 1.00 & 0.62 & 0.03 & 0.07 & 0.01 & 0.08 \\ -0.80 & -1.00 & 0.62 & 1.00 & 0.29 & 0.33 & 0.37 & 0.32 \\ -0.51 & -0.25 & 0.03 & 0.29 & 1.00 & 0.99 & 0.98 & 0.98 \\ -0.46 & -0.30 & 0.07 & 0.33 & 0.99 & 1.00 & 0.96 & 1.00 \\ -0.61 & -0.32 & 0.01 & 0.37 & 0.98 & 0.96 & 1.00 & 0.95 \\ -0.44 & -0.29 & 0.08 & 0.32 & 0.98 & 1.00 & 0.95 & 1.00 \end{pmatrix} . \tag{2.48}$$

The non-diagonal elements of C, which are close to ± 1, indicate strong correlations between the elements of ΔT_r. Consequently, the machine imperfections alter *correlated* groups of optical functions.

This observation can be further quantified by the eigenvector decomposition of C, which yields the following vector of eigenvalues $\lambda(C)$ for the $\beta^* = 3.5\,\mathrm{m}$ optics:

$$\lambda(C) = (4.9,\, 2.3,\, 0.53,\, 0.27,\, 0.01,\, 0.01,\, 0.00,\, 0.00)\,. \tag{2.49}$$

Since the two largest eigenvalues $\lambda_1 = 4.9$ and $\lambda_2 = 2.3$ dominate the others, the correlation system is practically two dimensional with the following two eigenvectors

$$v_1 = (\ \ 0.35,\ \ 0.30, -0.16, -0.31, -0.40, -0.41, -0.41, -0.40)\ , \tag{2.50}$$

$$v_2 = (-0.26, -0.46,\ \ 0.47,\ \ 0.45, -0.29, -0.27, -0.25, -0.28)\ . \tag{2.51}$$

Therefore, contributions of the individual lattice imperfections cannot be evaluated, see later Fig. 2.12. On the other hand, as the imperfections alter approximately only a two-dimensional subspace, a measurement of a small set of weakly correlated optical functions would theoretically yield an approximate knowledge of ΔT_r.

2.6.2 Error estimation of the method

Let us assume for the moment that we can precisely reconstruct the contributions to ΔT_r of the two most significant eigenvectors while neglecting the others. The error of such reconstructed transport matrix can be estimated by evaluating the contribution of the remaining eigenvectors:

$$\delta \Delta T_{r,i} = \sqrt{E_{i,i} \cdot V_{i,i}}\,, \tag{2.52}$$

where

$$E = N \cdot \begin{pmatrix} 0 & 0 & 0 & 0 & 0 \\ 0 & 0 & 0 & 0 & 0 \\ 0 & 0 & \lambda_3 & 0 & 0 \\ \vdots & & & \ddots & \vdots \\ 0 & 0 & 0 & 0 & \lambda_8 \end{pmatrix} \cdot N^{\mathrm{T}} \tag{2.53}$$

and $N = (\nu_1, ..., \nu_8)$ is the basis change matrix composed of eigenvectors ν_i corresponding to the eigenvalues λ_i.

The relative optics uncertainty before and after the estimation of the most significant eigenvectors is summarized in Table 2.3. According to the table, even if we limit ourselves

	$v_{x,\mathrm{far}}$	$L_{x,\mathrm{far}}$	$\frac{\mathrm{d}v_x}{\mathrm{d}s}$	$\frac{\mathrm{d}L_x}{\mathrm{d}s}$
$T_{r,i}$	-3.1	$-1.32 \cdot 10^{-1}\,\mathrm{m}$	$3.1 \cdot 10^{-2}\,\mathrm{m}^{-1}$	$-3.21 \cdot 10^{-1}$
$\frac{\sqrt{V_{i,i}}}{\lvert T_{r,i}\rvert}$ [%]	$2.0 \cdot 10^{-1}$	$3.4 \cdot 10^{2}$	$4.2 \cdot 10^{-1}$	1.6
$\frac{\delta\Delta T_{r,i}}{\lvert T_{r,i}\rvert}$ [%]	$9.5 \cdot 10^{-2}$	$9.1 \cdot 10^{1}$	$2.6 \cdot 10^{-1}$	$3.4 \cdot 10^{-1}$

	$v_{y,\mathrm{far}}$	$L_{y,\mathrm{far}}$	$\frac{\mathrm{d}v_y}{\mathrm{d}s}$	$\frac{\mathrm{d}Ly}{\mathrm{d}s}$
$T_{r,i}$	-4.3	$2.24 \cdot 10^{1}$ m	$-6.1 \cdot 10^{-2}\,\mathrm{m}^{-1}$	$8.60 \cdot 10^{-2}$
$\frac{\sqrt{V_{i,i}}}{\lvert T_{r,i}\rvert}$ [%]	$6.8 \cdot 10^{-1}$	4.3	$5.9 \cdot 10^{-1}$	$1.5 \cdot 10^{1}$
$\frac{\delta\Delta T_{r,i}}{\lvert T_{r,i}\rvert}$ [%]	$6.1 \cdot 10^{-2}$	$6.4 \cdot 10^{-1}$	$8.3 \cdot 10^{-2}$	2.75

Table 2.3: Nominal values of the optical functions $T_{r,i}$ and their relative uncertainty before ($\sqrt{V_{i,i}}/\lvert T_{r,i}\rvert$) and after ($\delta\Delta T_{r,i}/\lvert T_{r,i}\rvert$) the determination of the two most significant eigenvectors ($\beta^* = 3.5\,\mathrm{m}$, Beam 1).

only to the first two most significant eigenvalues, the uncertainty of optical functions due to machine imperfections drops significantly. In particular, in case of $\mathrm{d}L_x/\mathrm{d}s$ and L_y a significant error reduction down to a per mil level is observed. Unfortunately, due to $\Delta\mu_x = \pi$ (Figure 2.4), the uncertainty of L_x, although importantly improved, remains very large and the use of $\mathrm{d}L_x/\mathrm{d}s$ for proton kinematics reconstruction should be preferred, according to Eq. (2.38).

In the following sections a practical numerical method of inferring the optics from

the RP proton tracks is presented and its validation with Monte Carlo calculations is reported.

2.7 Optics constraints from tracks in RPs

Elastically scattered protons can be selected with high purity and efficiency by the TOTEM experiment at LHC [6, 35]. The RP detector system, due to its high resolution ($\sigma(x,y) \approx 11\,\mu$m, $\sigma(\vartheta_{x,y}) \approx 2.9\,\mu$rad), can measure very precisely the proton angles, positions and the angle-position relations on an event-by-event basis, see Section 1.3.1.

The kinematical variables of the detected particles can be used to define a set of estimators, which provide information about the correlations between the elements of the transport matrix T, defined with Eq. (2.29), and also about the correlations between the transport matrices of the two LHC beams. Such a set of estimators $\hat{R}_1, ..., \hat{R}_{10}$ (defined in the next sections) is exploited to reconstruct, for both LHC beams, the transport matrix $T(\mathcal{M}) + \Delta T$ defined in Eq. (2.44).

2.7.1 Correlations between the two LHC beams

The momentum of the two LHC beams is identical, thus the elastically scattered protons are deflected symmetrically from their nominal trajectories of Beam 1 and 2

$$\vartheta^*_{x,b_1} = -\vartheta^*_{x,b_2}\,, \vartheta^*_{y,b_1} = -\vartheta^*_{y,b_2}\,, \tag{2.54}$$

which allows to compute ratios $R_{1,2}$ relating the effective lengths at the RP locations of the two beams. From Eqs. (2.28) and (2.54) one obtains

$$R_1 \equiv \frac{\vartheta_{x,b_1}}{\vartheta_{x,b_2}} \approx \frac{\frac{\mathrm{d}L_{x,b_1}}{\mathrm{d}s}\cdot\vartheta^*_{x,b_1}}{\frac{\mathrm{d}L_{x,b_2}}{\mathrm{d}s}\cdot\vartheta^*_{x,b_2}} = -\frac{\frac{\mathrm{d}L_{x,b_1}}{\mathrm{d}s}}{\frac{\mathrm{d}L_{x,b_2}}{\mathrm{d}s}}\,, \tag{2.55}$$

and

$$R_2 \equiv \frac{y_{b_1,\mathrm{far}}}{y_{b_2,\mathrm{far}}} \approx -\frac{L_{y,b_1,\mathrm{far}}}{L_{y,b_2,\mathrm{far}}}\,. \tag{2.56}$$

Approximations present in Eqs. (2.55) and (2.56) represent the impact of statistical effects such as detector resolution, beam divergence, primary vertex position distribution and longitudinal momentum spread of the particles.

The estimators $\hat{R}_1$ and $\hat{R}_2$ are obtained from the $(\vartheta_{x,b_1}, \vartheta_{x,b_2})$ and $(y_{b_1,far}, y_{b_2,far})$ distributions and are defined with the help of the distributions' principal eigenvector, as illustrated in Fig. 2.9 and reported in Table 2.4. The beam divergence and the vertex contribution widen the distributions defining the estimators uncertainty, see Table 2.4.

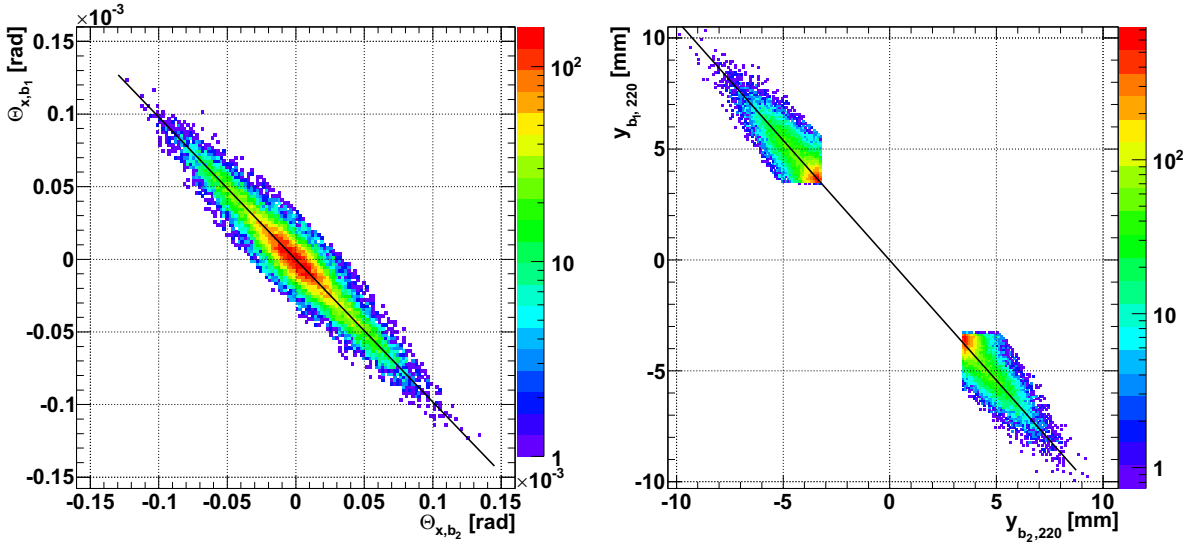

Figure 2.9: Beam 1 and 2 elastic scattering angle correlation in the horizontal plane $(\vartheta_{x,b_1}, \vartheta_{x,b_2})$ (left panel) and correlation between vertical positions (right panel) of elastically scattered protons detected by the RPs. The plots also illustrate the linear fit of the distributions whose slope parameter is the estimator $\hat{R}_1$ and $\hat{R}_2$, respectively.

2.7.2 Single beam correlations

The distributions of proton angles and positions measured by the Roman Pots define the ratios of certain elements of the transport matrix T, defined by Eqs. (2.28) and (2.29). First of all, $\mathrm{d}L_y/\mathrm{d}s$ and L_y are related by

$$R_3 \equiv \frac{\vartheta_{y,b_1}}{y_{b_1}} \approx \frac{\frac{\mathrm{d}L_{y,b_1}}{\mathrm{d}s}}{L_{y,b_1}}\,, \quad R_4 \equiv \frac{\vartheta_{y,b_2}}{y_{b_2}} \approx \frac{\frac{\mathrm{d}L_{y,b_2}}{\mathrm{d}s}}{L_{y,b_2}}\,. \tag{2.57}$$

The corresponding estimators $\hat{R}_3$ and $\hat{R}_4$ can be calculated as presented in Table. 2.4.

Similarly, we exploit the horizontal dependencies to quantify the relations between $\mathrm{d}L_x/\mathrm{d}s$ and L_x. As L_x is close to 0, see Fig. 2.6, instead of defining the ratio we rather estimate the position s_0 along the beam line (with the uncertainty of about 1 m), for

which $L_x = 0$. This is accomplished by resolving

$$\frac{L_x(s_0)}{\mathrm{d}L_x(s_1)/\mathrm{d}s} = \frac{L_x(s_1)}{\mathrm{d}L_x(s_1)/\mathrm{d}s} + (s_0 - s_1) = 0\,, \tag{2.58}$$

for s_0, where s_1 denotes the coordinate of the Roman Pot station along the beam with respect to IP5. Obviously, $\mathrm{d}L_x(s)/\mathrm{d}s$ is constant along the RP station as no magnetic fields are present at the RP location. The ratios $L_x(s_1)/\frac{\mathrm{d}L_x(s_1)}{\mathrm{d}s}$ for Beam 1 and 2, similarly to the vertical constraints R_3 and R_4, are defined by the proton tracks:

$$\frac{L_x}{\frac{\mathrm{d}L_x}{\mathrm{d}s}} \approx \frac{x}{\vartheta_x}\,, \tag{2.59}$$

which are reported in Table 2.4. In this way two further constraints and the corresponding estimators (for Beam 1 and 2) are obtained:

$$R_5 \equiv s_{b_1} \text{ and } R_6 \equiv s_{b_2}\,. \tag{2.60}$$

2.7.3 Coupling / rotation

In reality the coupling coefficients $m_{13}, ..., m_{42}$ cannot be always neglected, as it is assumed by Eq. (2.33). RP proton tracks can help to determine the coupling components of the transport matrix T as well, where it is especially important that L_x is close to zero at the RP locations. Always based on Eqs. (2.28) and (2.29), four additional constraints (for each of the two LHC beams and for each unit of the RP station) can be defined:

$$R_{7,...,10} \equiv \frac{x_{\mathrm{near(far)}}}{y_{\mathrm{near(far)}}} \approx \frac{m_{14,\mathrm{near(far)}}}{L_{y,\mathrm{near(far)}}}\,. \tag{2.61}$$

The subscripts "near" and "far" indicate the position of the RP along the beam with respect to the IP. Geometrically $R_{7,...,10}$ describe the rotation of the RP scoring plane about the beam axis. Analogously to the previous sections, the estimators $\hat{R}_{7,...,10}$ are obtained from track distributions as presented in Table 2.4.

Constraints' values

Table 2.4 reports the values of the estimators defined in the previous sections. The estimators R_7 and R_8 are calculated for the 'near' and 'far' RPs of Beam 1, while R_9 and R_{10} represent the values for Beam 2.

i of $\hat{R}_i$	Value	Uncertainty [%]	i of $\hat{R}_i$	Value	Uncertainty [%]
1	-0.9895	0.5	6	217.6	0.2
2	-1.0954	0.2	7	0.0436	1.6
3	0.00388	0.4	8	0.0390	1.3
4	0.00262	1.5	9	0.0369	2.4
5	217.0	0.2	10	0.0316	3.5

Table 2.4: The measured value and uncertainty of the optics constraints $\hat{R}_i$ in case of the $\beta^* = 3.5$ m optics.

2.7.4 Optical functions estimation

The machine imperfections $\Delta\mathcal{M}$, leading to the transport matrix change ΔT, are in practice determined with the χ^2 minimization procedure:

$$\widehat{\Delta\mathcal{M}} = arg\,min(\chi^2)\,, \tag{2.62}$$

defined on the basis of the estimators $\hat{R}_1, ..., \hat{R}_{10}$, where the $arg\,min$ function gives the phase space position where the χ^2 is minimized. As it was discussed in Section 2.6.1, although the overall alteration of the transport matrix ΔT can be determined precisely based on a few optical functions' measurements, the contributions of individual imperfections cannot be established. In terms of optimization, such a problem has no unique solution and additional constraints, defined by the machine tolerance, have to be added.

Therefore, the χ^2 function is composed of the part defined by the Roman Pot tracks' distributions and the one reflecting the LHC tolerances:

$$\chi^2 = \chi^2_{\text{Design}} + \chi^2_{\text{Measured}}\,. \tag{2.63}$$

The design part

$$\chi^2_{\text{Design}} = \sum_{i=1}^{12}\left(\frac{k_i - k_{i,\text{MAD-X}}}{\sigma(k_i)}\right)^2 + \sum_{i=1}^{12}\left(\frac{\phi_i - \phi_{i,\text{MAD-X}}}{\sigma(\phi_i)}\right)^2 + \sum_{i=1}^{2}\left(\frac{p_i - p_{i,\text{MAD-X}}}{\sigma(p_i)}\right)^2, \tag{2.64}$$

where k_i and ϕ_i are the nominal strength and rotation of the ith magnet, respectively. Thus Eq. (2.64) defines the nominal machine (k_i, ϕ_i, p_i) as an attractor in the phase space. Both LHC beams are treated simultaneously. Only the relevant subset of machine imperfections $\Delta\mathcal{M}$ was selected. The obtained 26-dimensional optimization phase space includes the magnet strengths (12 variables), rotations (12 variables) and beam momentum offsets (2 variables). Magnet rotations are included into the phase space, otherwise only the coupling coefficients $m_{13}, ..., m_{42}$ could induce rotations in the (x, y) plane Eq. (2.61), which could bias the result.

The measured part

$$\chi^2_{\text{Measured}} = \sum_{i=1}^{10} \left(\frac{\hat{R}_i - R_{i,\text{MAD-X}}}{\sigma(\hat{R}_i)} \right)^2 \tag{2.65}$$

contains the track-based estimators $\hat{R}_1, ..., \hat{R}_{10}$ (discussed in detail in Section 2.7) together with their uncertainty. The subscript "MAD-X" defines the corresponding values evaluated with the MAD-X software during the χ^2 minimization.

Table 2.5 presents the results of the optimization procedure for the $\beta^* = 3.5\,\text{m}$ optics used by LHC in October 2010 at beam energy $E_{\text{beam}} = 3.5\,\text{TeV}$. The obtained value of the effective length L_y of Beam 1 is close to the nominal one, while Beam 2 shows a significant change. The same pattern applies to the values of $\text{d}L_x/\text{d}s$. The error estimation of the procedure is discussed in Section 2.8. The $\beta^* = 90\,\text{m}$ results at $E_{\text{beam}} = 4\,\text{TeV}$ are also presented in Table 2.6.

	$\beta^* = 3.5$ m			
	$L_{y,b_1,\text{far}}$ [m]	$\text{d}L_{x,b_1}/\text{d}s$	$L_{y,b_2,\text{far}}$ [m]	$\text{d}L_{x,b_2}/\text{d}s$
Nominal	22.4	$-3.21 \cdot 10^{-1}$	18.4	$-3.29 \cdot 10^{-1}$
Estimated	22.6	$-3.12 \cdot 10^{-1}$	20.7	$-3.15 \cdot 10^{-1}$

Table 2.5: Selected optical functions of both LHC beams for the $\beta^* = 3.5$ m optics, obtained with the estimation procedure, compared to their nominal values.

	$\beta^* = 90$ m			
	$L_{y,b_1,\text{far}}$ [m]	$\mathrm{d}L_{x,b_1}/\mathrm{d}s$	$L_{y,b_2,\text{far}}$ [m]	$\mathrm{d}L_{x,b_2}/\mathrm{d}s$
Nominal	263.2	$-5.36 \cdot 10^{-1}$	263.2	$-5.36 \cdot 10^{-1}$
Estimated	264.1	$-5.25 \cdot 10^{-1}$	266.3	$-5.17 \cdot 10^{-1}$

Table 2.6: Selected optical functions of both LHC beams for the $\beta^* = 90$ m optics, obtained with the estimation procedure, compared to their nominal values.

The interplay between the detector alignment and the optics matching procedure is discussed in details in Ref. [8].

2.8 Monte Carlo validation

In order to demonstrate that the proposed $\hat{R}_i$ optics estimators are effective I have validated the method with Monte Carlo simulations.

In each Monte Carlo simulation the nominal machine settings $\mathcal{M}$ were altered with simulated machine imperfections $\Delta\mathcal{M}$ within their tolerances using Gaussian distributions. The simulated elastic proton tracks were used afterwards to calculate the estimators $\hat{R}_1, ..., \hat{R}_{10}$. The study included the impact of

- magnet strengths,
- beam momenta,
- magnet displacements, rotations and harmonics,
- settings of kickers,
- measured proton angular distribution.

The error distributions of the optical functions ΔT obtained for $\beta^* = 3.5\,\text{m}$ and $E_\text{beam} = 3.5\,\text{TeV}$ are presented in Figs. 2.10 and 2.11, also in Table 2.7, while the $\beta^* = 90\,\text{m}$ results at $E_\text{beam} = 4\,\text{TeV}$ are shown in Fig. 2.13 and Table 2.8.

	Simulated optics distribution		Reconstructed optics error	
Relative optics distribution	Mean [%]	RMS [%]	Mean [%]	RMS [%]
$\frac{\delta L_{y,b_1,\mathrm{far}}}{L_{y,b_1,\mathrm{far}}}$	0.39	4.2	$8.3 \cdot 10^{-2}$	0.16
$\frac{\delta \mathrm{d}L_{x,b_1}/\mathrm{d}s}{\mathrm{d}L_{x,b_1}/\mathrm{d}s}$	−0.97	1.6	−0.13	0.17
$\frac{\delta L_{y,b_2,\mathrm{far}}}{L_{y,b_2,\mathrm{far}}}$	−0.14	4.9	0.21	0.16
$\frac{\delta \mathrm{d}L_{x,b_2}/\mathrm{d}s}{\mathrm{d}L_{x,b_2}/\mathrm{d}s}$	0.10	1.7	$-9.7 \cdot 10^{-2}$	0.17

Table 2.7: The Monte-Carlo study of the impact of the LHC imperfections $\Delta\mathcal{M}$ on selected transport matrix elements $\mathrm{d}L_x/\mathrm{d}s$ and L_y for $\beta^* = 3.5\,\mathrm{m}$ at $E_{\mathrm{beam}} = 3.5$ TeV. The LHC parameters were altered within their tolerances. The relative errors of $\mathrm{d}L_x/\mathrm{d}s$ and L_y (mean value and RMS) characterize the optics uncertainty before and after optics estimation.

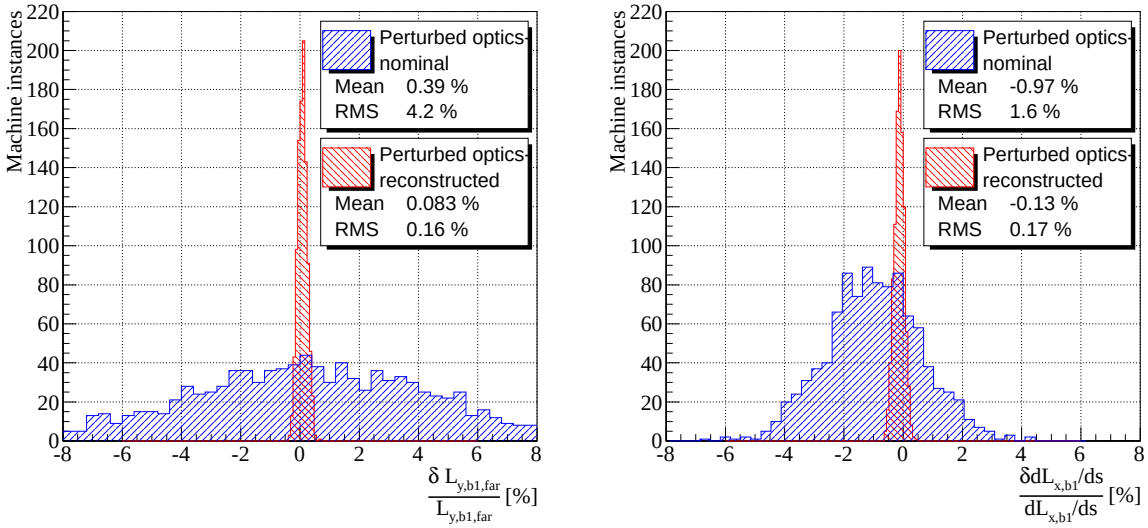

Figure 2.10: The MC error distribution of $\beta^* = 3.5$ m optical functions L_y and $\mathrm{d}L_x/\mathrm{d}s$ for Beam 1 at $E_{\mathrm{beam}} = 3.5$ TeV, before and after optics estimation.

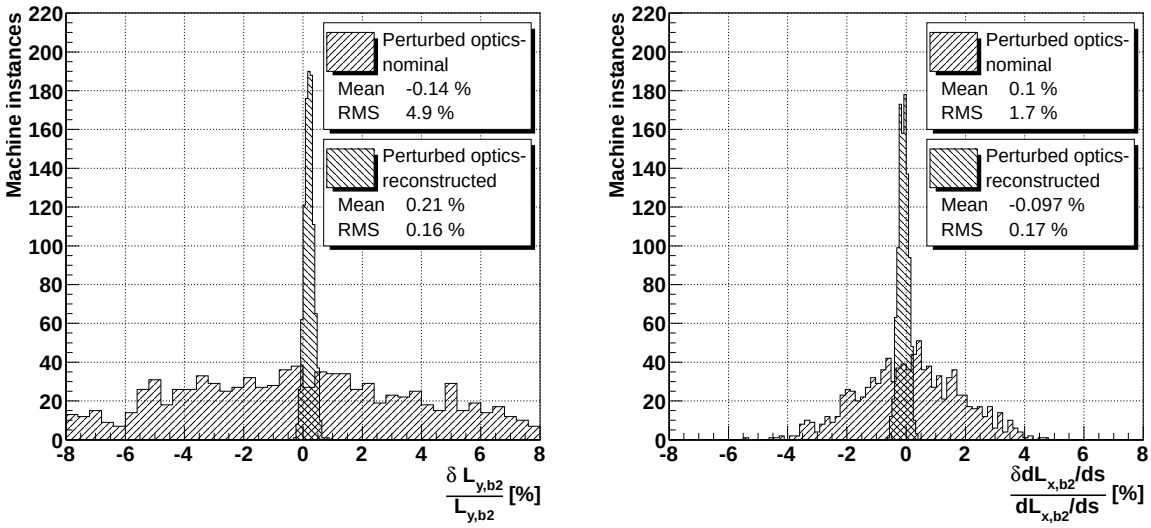

Figure 2.11: The MC error distribution of $\beta^* = 3.5$ m optical functions L_y and $\mathrm{d}L_x/\mathrm{d}s$ for Beam 2 at $E_{\mathrm{beam}} = 3.5$ TeV, before and after optics estimation.

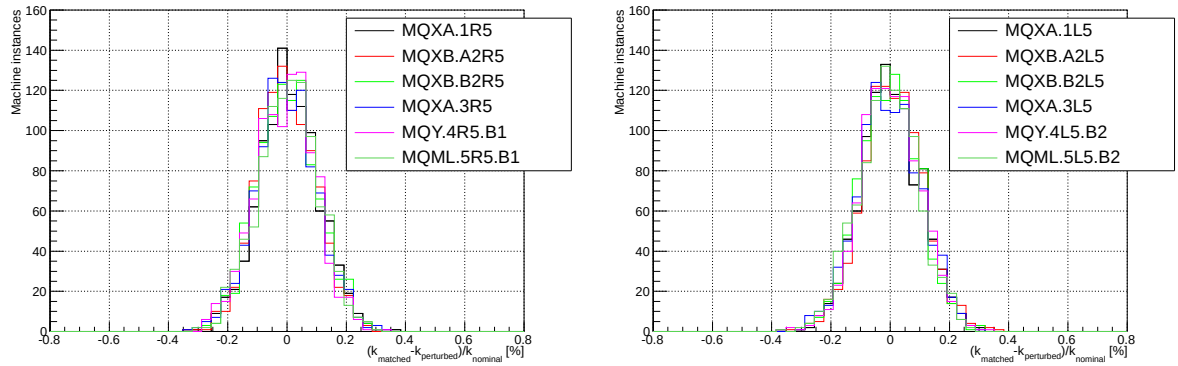

Figure 2.12: The distribution of the magnets' relative strength after optics estimation, Beam 1 (left panel) and Beam 2 (right panel), in case of $\beta^* = 3.5$ m optics at $E_{\mathrm{beam}} = 3.5$ TeV.

	Simulated optics distribution		Reconstructed optics error	
Relative optics distribution	Mean [%]	RMS [%]	Mean [%]	RMS [%]
$\frac{\delta L_{y,b_1,\mathrm{far}}}{L_{y,b_1,\mathrm{far}}}$	$2.2 \cdot 10^{-2}$	0.46	$5.8 \cdot 10^{-2}$	0.23
$\frac{\delta \mathrm{d}L_{x,b_1}/\mathrm{d}s}{\mathrm{d}L_{x,b_1}/\mathrm{d}s}$	$6.7 \cdot 10^{-3}$	1.5	$-6.4 \cdot 10^{-2}$	0.20
$\frac{\delta L_{y,b_2,\mathrm{far}}}{L_{y,b_2,\mathrm{far}}}$	$-5 \cdot 10^{-3}$	0.47	$5.8 \cdot 10^{-2}$	0.23
$\frac{\delta \mathrm{d}L_{x,b_2}/\mathrm{d}s}{\mathrm{d}L_{x,b_2}/\mathrm{d}s}$	$1.8 \cdot 10^{-2}$	1.5	$-7 \cdot 10^{-2}$	0.21

Table 2.8: The Monte-Carlo study of the impact of the LHC imperfections $\Delta\mathcal{M}$ on selected transport matrix elements $\mathrm{d}L_x/\mathrm{d}s$ and L_y for $\beta^* = 90\,\mathrm{m}$ at $E_{\mathrm{beam}} = 4$ TeV. The LHC parameters were altered within their tolerances. The relative errors of $\mathrm{d}L_x/\mathrm{d}s$ and L_y (mean value and RMS) characterize the optics uncertainty before and after optics estimation.

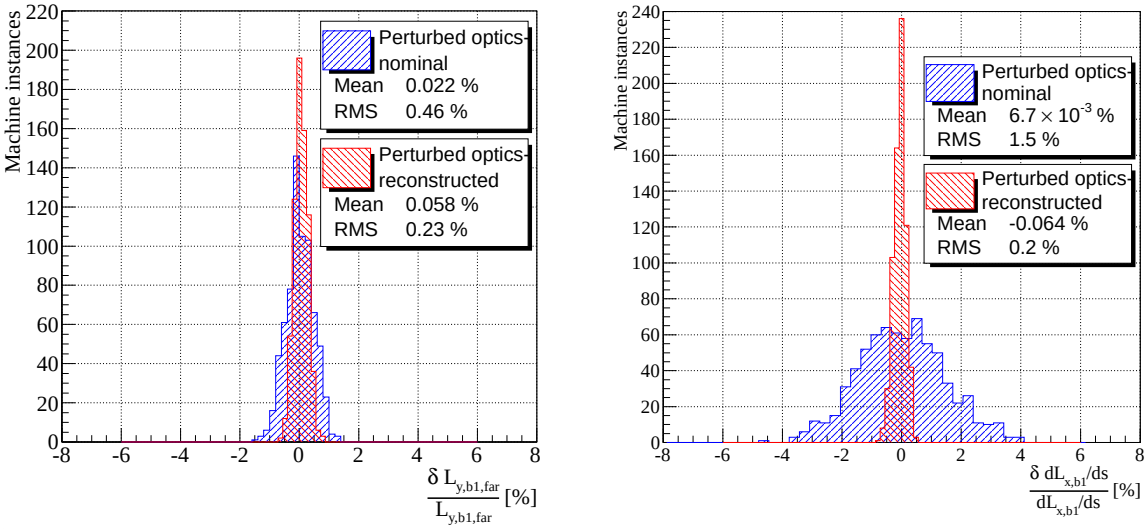

Figure 2.13: The MC error distribution of $\beta^* = 90$ m optical functions L_y and $\mathrm{d}L_x/\mathrm{d}s$ for Beam 1 at $E_{\mathrm{beam}} = 4$ TeV, before and after optics estimation.

First of all, the impact of the machine imperfections $\Delta\mathcal{M}$ on the transport matrix ΔT, as shown by the MC study, is identical to the theoretical prediction presented in

Table 2.3. The bias of the simulated optics distributions is due to magnetic field harmonics as reported by the LHC imperfections database [50]. The final value of mean after optics estimation procedure contributes to the total uncertainty of the method.

The errors of the reconstructed optical functions are significantly smaller than evaluated theoretically in Section 2.6.2. This results from the larger number of constraints, design and measured constraints Eq. (2.63), employed in the numerical estimation procedure of Section 2.7.4. In particular, the collinearity of elastically scattered protons was exploited in addition. Finally, the achieved uncertainties of $\mathrm{d}L_x/\mathrm{d}s$ and L_y are both lower than 2.5 ‰ for both beams.

Other non-published details about the recalibration of the LHC optics from TOTEM data are summarized in my TOTEM internal analysis note of Ref. [9].

2.9 Summary of Chapter 2

I have validated and applied a new method to estimate the LHC optics for the TOTEM collaboration. The main result of the method is the determination of the vertical effective length L_y and the derivative of the horizontal effective length $\mathrm{d}L_x/\mathrm{d}s$ optical functions with an uncertainty smaller than 2.5 ‰ [8, 9].

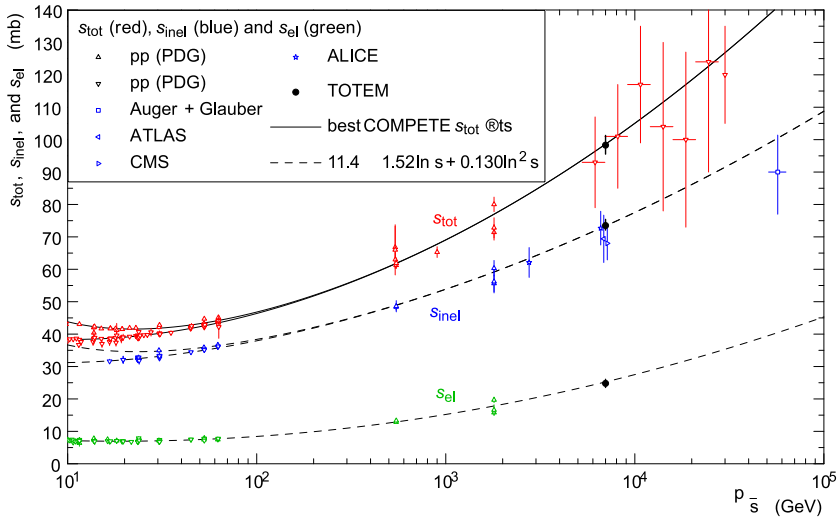

Figure 2.14: Compilation of the total cross-section σ_{tot} measurements from Ref. [6]. The TOTEM result demonstrates the impact of the optics estimation procedure.

The optics estimation method allows for the determination of the LHC optics with a per mil level uncertainty in case of low-β^* LHC optics, where machine imperfections have the highest influence, also allowing to estimate the transport matrix uncertainties. In case of high-β^* LHC optics the method remains effective and reduces the uncertainties to the per mil level. The method has been validated with Monte Carlo studies both for high- and low-β^* optics.

The optics estimation method, reported in this chapter, was successfully used by the TOTEM experiment to estimate the real optics for TOTEM physics runs; see especially Refs. [35] and [57], where the contribution of the LHC beam optics into the reconstruction of the squared four-momentum transfer $|t|$ is discussed in details; see also Fig. 2.14 about the compilation of the total cross-section $\sigma_{\rm tot}$ measurements from Ref. [6], where the TOTEM result demonstrates the impact of the optics estimation procedure.

Chapter 3

Test of the BB model at the LHC

3.1 Introduction

In Chapter 1 it was briefly discussed that the interpretation of the *pp* elastic scattering data at low values of the squared four-momentum transfer $|t|$ involves the geometrical scale of the proton (obstacle) size, which leads to an analogous behavior of the cross-sections in case of optical and high-energy particle diffraction [2, 58]. Chapter 2 gave insight into one of the experimental techniques used by the TOTEM experiment to obtain the measured elastic *pp* differential cross-section data. In the present Chapter I turn to interpret the measured data using the particular geometrical model of elastic *pp* scattering of Bialas and Bzdak (BB model).

The BB model is based on the so-called "eikonal picture" which is the high-energy particle physics analogue of optical Fraunhofer-diffraction [10]. In the eikonal picture the unitarity relation Eq. (3.4), the equivalent of $\sigma_{\rm el} + \sigma_{\rm inel} = \sigma_{\rm tot}$ in the so-called impact parameter space, determines the elastic scattering amplitude. The unitarity relation Eq. (3.4) can be straightforwardly derived in non-relativistic potential scattering theory [2, 59]. In accordance with the optical analogy, the quantum mechanical result is formally very similar to the optical formulae calculated from Kirchhoff's diffraction theory in the Fraunhofer limit. My PhD dissertation uses the framework of relativistic S-matrix theory, where the eikonal picture can be defined using the partial wave expansion [2]. On this theoretical ground the original BB model is defined in Sections 3.2 and 3.3. The fit method is briefly described in Section 3.4.

I have first confirmed the calculations and results of Bialas and Bzdak using the original BB model at ISR energies [11]. The method of Bialas and Bzdak does not allow to assess the fitted parameters' uncertainty, see Section 3.4 for details. I have determined the best values and uncertainties of the BB model parameters using the MINUIT minimization code [60]. I have fitted the BB model at ISR energies and at the LHC energy of $\sqrt{s} = 7$ TeV, the results are presented in Sections 3.3 and 3.5. My results demonstrate that the original BB model is not able to interpret the $\sqrt{s} = 7$ TeV pp elastic differential cross-section data measured by the TOTEM experiment. I have introduced an effective proton radius R_{eff}, and I have found that R^2_{eff} is proportional to the total pp cross-section at ISR energies [11].

I have generalized the original BB model by including a perturbatively small real part into the model's scattering amplitude in order to provide a better description of the measured elastic pp differential cross-section data [12]. I have fitted the improved model (αBB model) at ISR and LHC energies, the results are discussed in Chapter 4. I have shown that the new αBB model can be fitted at ISR energies reliably. However, even the new αBB model is not able to describe the $\sqrt{s} = 7$ TeV TOTEM data, which suggests the interpretation that the real part of the FSA becomes non-perturbatively large. In addition I have found a relation between the total pp cross-section and the position of the first diffractive minimum, motivated by the so-called "black disc" scattering model, which shows a similar but quantitatively different behavior.

To overcome the clear disagreement between data and model description at the LHC energy of $\sqrt{s} = 7$ TeV, I have further generalized the BB model using unitarity constraints [13]. I have fitted the new model (ReBB model) at ISR and also at the LHC energy of $\sqrt{s} = 7$ TeV. I have determined the energy dependence of the ReBB model parameters based on the good quality of the fits at ISR and LHC energies and I have extrapolated the ReBB model to future LHC energies and beyond. I have shown that the effective interaction radius of the proton, calculated from the ReBB model, is increasing substantially between ISR and LHC energies, while the proton's effective "edge" shows the same width. I have demonstrated that the ReBB model shows a non-exponential feature at low values of the squared four-momentum transfer $|t|$, which is in agreement with the new TOTEM finding at $\sqrt{s} = 8$ TeV [57]. My results with the ReBB model are

presented in Chapter 5.

3.2 The Eikonal Picture and cross-section formulae

In this section I turn to describe the eikonal picture, the framework of the original BB model, and the basic cross-section formulae.

The scattering or S-matrix is the unitary operator which transforms the initial state $|i\rangle$ of a scattering process into the final state: $|f\rangle = S\,|i\rangle$. The unitarity of the S matrix

$$SS^\dagger = I\,, \tag{3.1}$$

where I is the identity matrix, ensures that the sum of the probabilities $P_{i\to f} = |\langle f|\,S\,|i\rangle|^2$ for all possible outcomes of the scattering process is one. The decomposition $S = I + \mathrm{i}\,T$, where T is the transition matrix, leads the unitarity equation Eq. (3.1) to

$$T - T^\dagger = \mathrm{i}\,TT^\dagger\,. \tag{3.2}$$

In case of high-energy scattering it is useful to define the impact parameter b with

$$\ell = \frac{b\sqrt{s}}{2}\,, \tag{3.3}$$

where ℓ is the angular momentum and s is the squared center-of-mass energy. The unitarity equation Eq. (3.2) can be rewritten in the form [2, 61]

$$2\,\mathrm{Im}\,t_{\mathrm{el}}(s,b) = |t_{\mathrm{el}}(s,b)|^2 + \tilde{\sigma}_{\mathrm{inel}}(s,b)\,, \tag{3.4}$$

where $t_{\mathrm{el}}(s,b)$ is the so-called profile function (or forward scattering amplitude of elastic scattering), which corresponds to the ℓth partial wave amplitude $T_\ell(s)$, through Eq. (3.3) [2, 59]. The function $\tilde{\sigma}_{\mathrm{inel}}(s,b) = \mathrm{d}^2\sigma_{\mathrm{inel}}/\mathrm{d}^2b$ is the so-called inelastic overlap function and represents the probability of absorption at each value of the impact parameter b; similarly $|t_{\mathrm{el}}(s,b)|^2 = \mathrm{d}^2\sigma_{\mathrm{el}}/\mathrm{d}^2b$. Eq. (3.4) is the reformulation of $\sigma_{\mathrm{tot}} = \sigma_{\mathrm{el}} + \sigma_{\mathrm{inel}}$ using the impact parameter b, where σ_{tot}, σ_{el} and σ_{inel} are the total, elastic and inelastic cross-sections, respectively.

The unitarity relation Eq. (3.4) is a second order polynomial equation in terms of the (complex) profile function $t_{\mathrm{el}}(s,b)$. If one defines the opacity function $\Omega(s,b)$ [59, 61–65]

$$t_{\mathrm{el}}(s,b) = \mathrm{i}\left[1 - e^{-\Omega(s,b)}\right]\,, \tag{3.5}$$

the inelastic overlap function $\tilde{\sigma}_{\text{inel}}$ can be expressed as

$$\tilde{\sigma}_{\text{inel}}(s,b) = 1 - e^{-2\,\text{Re}\,\Omega(s,b)}\,. \tag{3.6}$$

The formula for t_{el} is the so called eikonal form. From Eq. (3.6) the real part of the opacity function $\Omega(s,b)$ can be expressed as

$$\text{Re}\,\Omega(s,b) = -\frac{1}{2}\ln\left[1 - \tilde{\sigma}_{\text{inel}}(s,b)\right]\,. \tag{3.7}$$

In the original BB model it is assumed that the real part of the profile function t_{el} vanishes. In this case Eqs. (3.5) and (3.7) imply that

$$t_{\text{el}}(s,b) = \text{i}\left[1 - \sqrt{1 - \tilde{\sigma}_{\text{inel}}(s,b)}\right]\,. \tag{3.8}$$

If the imaginary part $\text{Im}\,\Omega$ is taken into account in Eq. (3.5) the result is

$$t_{\text{el}}(s,b) = \text{i}\left[1 - e^{-\text{i}\,\text{Im}\,\Omega(s,b)}\sqrt{1 - \tilde{\sigma}_{\text{inel}}(s,b)}\right]\,, \tag{3.9}$$

where the concrete parametrization of $\text{Im}\,\Omega(s,b)$ is discussed later.

The profile function Eq. (3.5) has to be transformed into momentum space to obtain the elastic scattering amplitude

$$\begin{aligned} T(s,\Delta) &= \int_{-\infty}^{+\infty}\int_{-\infty}^{+\infty} e^{\text{i}\vec{\Delta}\cdot\vec{b}}\, t_{\text{el}}(s,b)\,\text{d}^2b \\ &= 2\pi\,\text{i}\int_0^{\infty} J_0\left(\Delta\cdot b\right)\left[1 - e^{-\Omega(s,b)}\right] b\,\text{d}b\,, \end{aligned} \tag{3.10}$$

where $b = |\vec{b}|$, $\Delta = |\vec{\Delta}|$ is the transverse momentum and J_0 is the zero order Bessel-function of the first kind. In the high energy limit, $\sqrt{s} \to \infty$, $\Delta(t) \simeq \sqrt{-t}$, where t is the squared four-momentum transfer, see also Eq. (A.17). According to the definition of the scattering amplitude the elastic differential cross-section can be evaluated as [2]

$$\frac{\text{d}\sigma}{\text{d}t} = \frac{1}{4\pi}\left|T\left(s,\Delta\right)\right|^2\,, \tag{3.11}$$

and the optical theorem tells us that the total cross-section Eq. (1.3) [2]

$$\sigma_{\text{tot}} = 2\,\text{Im}\,T(s,\Delta)\big|_{t=0}\,. \tag{3.12}$$

The ratio of the real to the imaginary FSA is abbreviated as

$$\rho = \frac{\text{Re}\,T(s,0)}{\text{Im}\,T(s,0)}\,. \tag{3.13}$$

3.3 The diquark scatters as a single entity

In this section I follow the lines of my research papers [11–13]. The original BB model [10] describes the proton as a bound state of a quark and a diquark, where both constituents have to be understood as "dressed" objects that effectively include all possible virtual gluons and $q\bar{q}$ pairs. The quark and the diquark are characterized with their positions with respect to the proton's center-of-mass using their transverse position vectors $\vec{s}_q$ and $\vec{s}_d$ in the plane perpendicular to the proton's incident momentum. Hence, the coordinate space H of the colliding protons is spanned by the vector $h = (\vec{s}_q, \vec{s}_d, \vec{s}\,'_q, \vec{s}\,'_d)$ where the primed coordinates indicate the coordinates of the second proton.

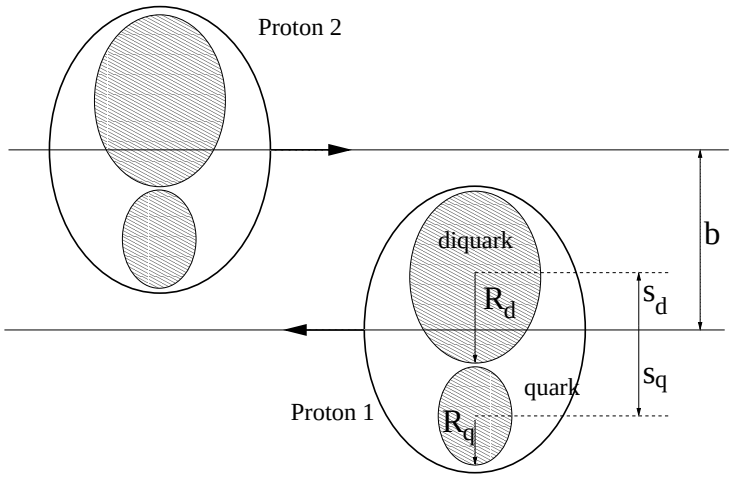

Figure 3.1: Scheme of the scattering of two protons in the impact parameter space, when the proton is assumed to have a quark-diquark structure and the diquark is assumed to be scattered as a single entity. This is just a snapshot and all the model parameters follow a Gaussian distribution.

The inelastic pp scattering probability $\tilde{\sigma}_{\rm inel}(s,b)$ of Eq. (3.8) is calculated as an average of "elementary" inelastic scattering probabilities $\sigma(h;\vec{b})$ over the coordinate space H [66]

$$\tilde{\sigma}_{\rm inel}(b) = \Big\langle \sigma(h;\vec{b}) \Big\rangle_H = \int_{-\infty}^{+\infty} \dots \int_{-\infty}^{+\infty} \mathrm{d}h\, p(h) \cdot \sigma(h;\vec{b})\,, \tag{3.14}$$

where the weight function $p(h)$ is a product of probability distributions

$$p(h) = D(\vec{s}_q, \vec{s}_d) \cdot D(\vec{s}\,'_q, \vec{s}\,'_d)\,. \tag{3.15}$$

The $D(\vec{s}_q, \vec{s}_d)$ function is a two-dimensional Gaussian, which describes the center-of-mass distribution of the quark and diquark with respect to the center-of-mass of the proton

$$D\left(\vec{s}_q, \vec{s}_d\right) = \frac{1+\lambda^2}{R_{qd}^2\,\pi} e^{-(s_q^2+s_d^2)/R_{qd}^2} \delta^2(\vec{s}_d + \lambda \vec{s}_q)\,, \tag{3.16}$$

where

$$\lambda = \frac{m_q}{m_d}\,, \tag{3.17}$$

is the dimensionless ratio of the quark m_q and diquark m_d masses.

The parameter R_{qd}, the standard deviation of the quark and diquark distance, is determined from the fit to the data. Note that the two-dimensional Dirac δ function preserves the proton's center-of-mass and reduces the dimension of the integral in Eq. (3.14) from eight to four.

It is assumed that the "elementary" inelastic scattering probability $\sigma(h;\vec{b})$ can be factorized in terms of binary collisions among the constituents with a Glauber expansion

$$\sigma(h;\vec{b}) = 1 - \prod_a \prod_b \left[1 - \sigma_{ab}(\vec{b} + \vec{s}\,'_a - \vec{s}_b)\right]\,, \quad a,b \in \{q,d\}\,, \tag{3.18}$$

where the indices a and b can be either quark q or diquark d.

The $\sigma_{ab}\left(\vec{s}\right)$ functions describe the probability of binary inelastic collision between quarks and diquarks and are assumed to be Gaussian

$$\sigma_{ab}\left(\vec{s}\right) = A_{ab} e^{-s^2/S_{ab}^2},\ S_{ab}^2 = R_a^2 + R_b^2, \quad a,b \in \{q,d\}\,, \tag{3.19}$$

where the R_q, R_d and A_{ab} parameters are fitted to the data.

The inelastic cross-sections of quark, diquark scatterings can be calculated by integrating the probability distributions Eq. (3.19) as

$$\sigma_{ab,\mathrm{inel}} = \int_{-\infty}^{+\infty}\int_{-\infty}^{+\infty} \sigma_{ab}\left(\vec{s}\right) \mathrm{d}^2 s = \pi A_{ab} S_{ab}^2\,. \tag{3.20}$$

In order to reduce the number of free parameters, it is assumed that the diquarks are bound very weakly, hence the ratios of the inelastic cross-sections $\sigma_{ab,\mathrm{inel}}$ satisfy

$$\sigma_{qq,\mathrm{inel}} : \sigma_{qd,\mathrm{inel}} : \sigma_{dd,\mathrm{inel}} = 1 : 2 : 4\,, \tag{3.21}$$

which means that in the BB model the diquark contains twice as many partons than the quark and also that these quarks and diquarks do not "shadow" each other during the

scattering process. This assumption is not trivial. Note, that the version of the BB model where the diquark is assumed to be composite object, introduced in Section 3.5, allows for different $\sigma_{qq,\mathrm{inel}} : \sigma_{qd,\mathrm{inel}} : \sigma_{dd,\mathrm{inel}}$ ratios.

Using the inelastic cross-sections Eq. (3.20) together with the assumption Eq. (3.21) the A_{qd} and A_{dd} parameters can be expressed with A_{qq}

$$A_{qd} = A_{qq}\frac{4R_q^2}{R_q^2 + R_d^2}\,,\ A_{dd} = A_{qq}\frac{4R_q^2}{R_d^2}\,. \tag{3.22}$$

In this way only five parameters have to be fitted to the data R_{qd}, R_q, R_d, λ, and A_{qq}.

The last step in the calculation is to perform the Gaussian integrals in the average Eq. (3.14) to obtain a formula for $\tilde{\sigma}_{\mathrm{inel}}(b)$. The Dirac δ function in Eq. (3.16) expresses the protons' diquark position vectors as a function of the quarks position

$$\vec{s}_d = -\lambda\,\vec{s}_q\,,\ \ \vec{s}\,'_d = -\lambda\,\vec{s}\,'_q\,. \tag{3.23}$$

After expanding the products in the Glauber expansion Eq. (3.18) the following sum of contributions is obtained

$$\begin{aligned}\sigma(h;\vec{b}) =& \sigma_{qq} + 2\cdot\sigma_{qd} + \sigma_{dd} - (2\sigma_{qq}\sigma_{qd} + \sigma_{qd}^2 + \sigma_{qq}\sigma_{dd} + 2\sigma_{qd}\sigma_{dd}) \\ &+ (\sigma_{qq}\sigma_{qd}^2 + 2\sigma_{qq}\sigma_{qd}\sigma_{dd} + \sigma_{dd}\sigma_{qd}^2) - \sigma_{qq}\sigma_{qd}^2\sigma_{dd}\,,\end{aligned} \tag{3.24}$$

where the arguments of the $\sigma_{ab}(\vec{s})$ functions are suppressed to abbreviate the notation.

The average over H in Eq. (3.14) has to be calculated for each term in the above expansion Eq. (3.24). Take the last, most general, term and calculate the average; the remaining terms are simple consequences of it. The result is

$$I = \left\langle -\sigma_{qq}\sigma_{qd}^2\sigma_{dd}\right\rangle_H = \int_{-\infty}^{+\infty}\ldots\int_{-\infty}^{+\infty}\mathrm{d}h\,p(h)\cdot(-\sigma_{qq}\sigma_{qd}^2\sigma_{dd}\,)\,, \tag{3.25}$$

where the $p(h)$ weight function Eq. (3.15) is a product of the quark-diquark distributions, given by Eq. (3.16). Substitute into this result Eq. (3.25) the definitions of the quark-diquark distributions Eq. (3.16)

$$I = -\frac{4v^2}{\pi^2}\int_{-\infty}^{+\infty}\int_{-\infty}^{+\infty}\mathrm{d}^2 s_q\mathrm{d}^2 s'_q\,e^{-2v\left(s_q^2+s_q'^2\right)}\prod_k\prod_l\sigma_{kl}(\vec{b}-\vec{s}_k+\vec{s}\,'_l),\quad k,l\in\{q,d\}\,, \tag{3.26}$$

where $v = (1+\lambda^2)/(2\cdot R_{qd}^2)$ and the integral over the coordinate space H is explicitly written out; it is only four dimensional due to the two Dirac δ functions in $p(h)$. Using

the definitions of the $\sigma_{ab}(\vec{s})$ functions Eq. (3.19) and the expression $A = A_{qq}A_{qd}A_{dq}A_{dd}$ the integral Eq. (3.26) can be rewritten, to make all the Gaussian integrals explicit

$$I = -\frac{4v^2 A}{\pi^2} \int_{-\infty}^{+\infty}\int_{-\infty}^{+\infty} \mathrm{d}^2 s_q \mathrm{d}^2 s'_q \, e^{-2v\left(s_q^2 + s_q'^2\right)} \prod_k \prod_l e^{-c_{kl}\left(\vec{b} - \vec{s}_k + \vec{s}'_l\right)^2} , \tag{3.27}$$

where the abbreviations $c_{kl} = S_{kl}^{-2}$ refer to the coefficients in Eq. (3.19). Finally, the four Gaussian integrals have to be evaluated in our last expression Eq. (3.27), which leads to

$$I = -\frac{4v^2 A}{B} e^{-b^2 \frac{\Gamma}{B}} , \tag{3.28}$$

where

$$\begin{aligned} B &= C_{qd,dq}\left(v + c_{qq} + \lambda^2 c_{dd}\right) + (1-\lambda)^2 D_{qd,dq} , \\ \Gamma &= C_{qd,dq} D_{qq,dd} + C_{qq,dd} D_{qd,dq} , \end{aligned} \tag{3.29}$$

and

$$\begin{aligned} C_{kl,mn} &= 4v + (1+\lambda)^2 (c_{kl} + c_{mn}) , \\ D_{kl,mn} &= v\,(c_{kl} + c_{mn}) + (1+\lambda)^2 c_{kl} c_{mn} . \end{aligned} \tag{3.30}$$

Each term in Eq. (3.14) can be obtained from the master formula Eq. (3.28), by setting one or more coefficients to zero, $c_{kl} = 0$ and the corresponding amplitude to one, $A_{kl} = 1$.

3.4 Fit method

Bialas and Bzdak used the total inelastic cross-section, the slope of elastic cross-section at $t = 0$, the position of the dip and the height of the maximum after the dip to determine the value of the fit parameters by solving 4 equations with 4 unknowns in their original publication Ref. [10]. They found, that the resulting parameters provide a good overall description of elastic scattering data at ISR energies. However, neither the errors of the parameters nor the fit quality description with a χ^2/NDF test were provided.

I have used the CERN MINUIT fitting package to determine the best values of the model parameters together with their errors [60], with the χ^2 function

$$\chi^2 = \sum_{i=1}^{N} \left\{ \frac{\mathrm{d}\sigma_i/\mathrm{d}t - \gamma \cdot \mathrm{d}\sigma_{\mathrm{th},i}/\mathrm{d}t}{\sigma_i} \right\}^2 , \tag{3.31}$$

where the sum runs over the fitted data points [67]. The upper bound N of the sum in Eq. (3.31) is the number of fitted data points, $\mathrm{d}\sigma_i/\mathrm{d}t$ is the ith measured differential cross-section data point and $\mathrm{d}\sigma_{\mathrm{th},i}/\mathrm{d}t$ is the corresponding theoretical value at the ith data point calculated from the investigated model. The value σ_i is the mere statistical uncertainty of the ith data point.

In Chapter 5 I apply an additional term in the χ^2 function, which takes into account the luminosity uncertainty [60]

$$\chi^2_{\mathrm{lumi}} = \chi^2 + \frac{(\gamma_0 - \gamma)^2}{\sigma^2_{\mathrm{lumi}}}\,. \tag{3.32}$$

In this case the parameter γ becomes an additional parameter to be minimized. The constant $\gamma_0 \equiv 1$ abbreviates the unscaled value, while σ_{lumi} is the relative luminosity uncertainty reported by the measurement. I set parameter σ_{lumi} to a conservative value of 5 % at each ISR energy [1]. In case of the TOTEM data sets it is set to 4 %, which is determined by the uncertainty of the CMS luminosity [35, 68].

3.4.1 Fit results

In this section the MINUIT fit results are presented for the ISR [1, 69] and TOTEM [35] pp elastic scattering data considering the scenario when the diquark is assumed to act as a single entity in the scattering process. The BB model is fitted with Eq. (3.31) without the use of the luminosity error.

In a preliminary analysis all model parameters were optimized [70], including also the values of λ and A_{qq}, resulting in large parameter errors due to the strong correlations among the fit parameters [70]. In the fits presented in this PhD thesis I fix the values of the BB model parameters

$$\lambda = 0.5\,, \quad A_{qq} = 1.0\,, \tag{3.33}$$

where the latter assumption means that head-on qq collisions are inelastic with a probability of 1, according to Eq. (3.19).

Our corresponding results are shown in Fig. 3.2. The confidence levels, and model parameters together with their errors are presented in Table 3.1. The calculated elastic cross-sections, including their uncertainty, were evaluated from the MINUIT fits to the differential cross-section data. At the end of this section I also study and discuss, what

happens when the measured total cross-sections are also added, as additional data points, to the optimalization procedure.

The ratios of the inelastic cross-sections were fixed with Eq. (3.21), in order to decrease the number of free fit parameters, therefore these ratios will be provided only for the case, when the diquark is assumed to be a composite object.

The original form of the BB model shows a singular behavior at the diffractive minima, which unphysical region may completely dominate the fit results. To obtain a meaningful fit result, I have excluded 3 data points from the optimalization procedure, that were closest to the dip region at the ISR energies. These points are shown in red (color online) on the plots. I have checked that leaving out 5 or 7 points do not change the results.

Another important remark is that the TOTEM data covers the $|t|$ range from 0.36 GeV^2 up to 2.5 GeV^2 and this range is applied in my analysis to allow a comparison between the ISR and TOTEM results.

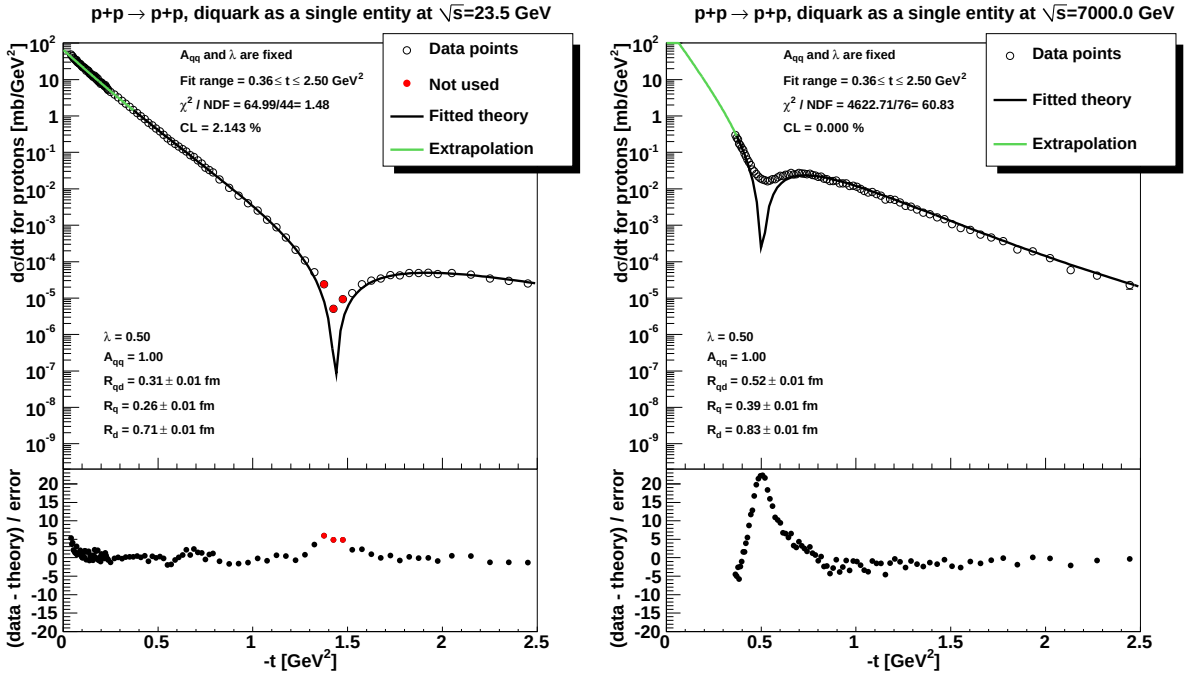

Figure 3.2: Results of MINUIT fits with the original BB model at ISR energy of $\sqrt{s}$ = 23.5 GeV (left) and LHC energy of $\sqrt{s}$ = 7 TeV (right) in the 0.36 to 2.5 GeV^2 $|t|$ fit range, when the diquark is assumed to scatter as a single entity. The BB model is singular at the dip, hence 3 data points at the dip, indicated with filled (red) circles, are left out from the fit of the ISR data.

$\sqrt{s}$ [GeV]	23.5	30.7	52.8	62.5	7000
R_{qd} [fm]	0.31 ± 0.01	0.34 ± 0.01	0.36 ± 0.01	0.31 ± 0.01	0.52 ± 0.01
R_q [fm]	0.26 ± 0.01	0.25 ± 0.01	0.25 ± 0.01	0.28 ± 0.01	0.39 ± 0.01
R_d [fm]	0.71 ± 0.01	0.71 ± 0.01	0.71 ± 0.01	0.75 ± 0.01	0.83 ± 0.01
χ^2/NDF	65.0/44	26.7/32	57.2/33	52.9/33	4622.7/76
CL [%]	2.14	73.05	0.55	1.56	0.0
σ_{elastic} [mb]	6.2 ± 0.1	5.1 ± 0.3	5.0 ± 0.3	7.3 ± 0.3	17.9 ± 0.2

Table 3.1: The BB model fit quality and resulting parameters of the fit at ISR energies including the LHC result at $\sqrt{s} = 7$ TeV, in the 0.36 to 2.5 GeV^2 $|t|$ range. The diquark is assumed to be a single entity.

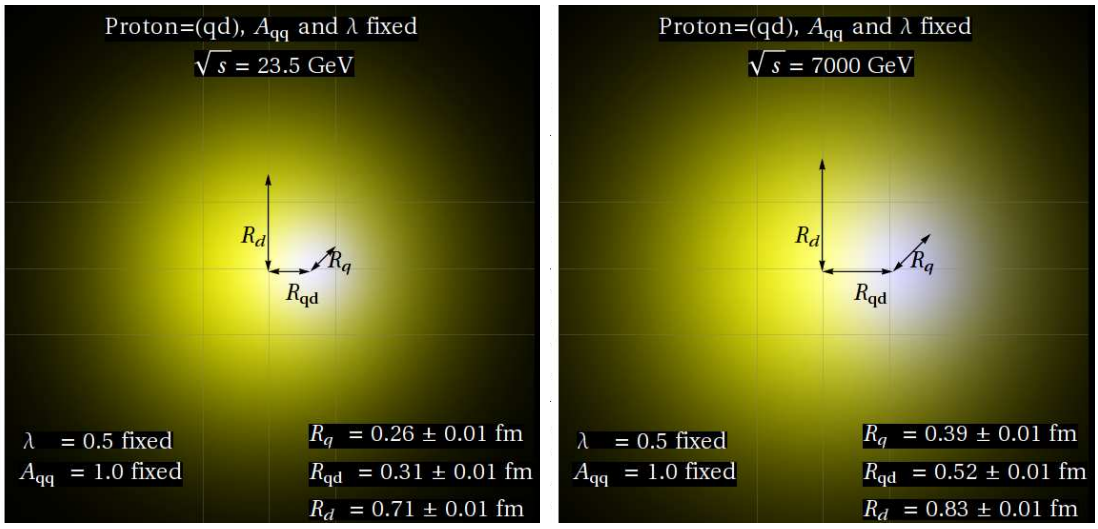

Figure 3.3: Visualization of the obtained R_{qd}, R_q and R_d BB model parameters for the case when the proton is assumed to scatter as a quark-diquark composite, $p = (q, d)$. The main observation is that the proton seems to be much larger at the LHC energy than in the ISR regime. This is mainly due to an increase in the R_{qd} parameter, that characterizes the separation of the quark and the diquark. However, as the CL of the fit to the TOTEM data at $\sqrt{s} = 7$ TeV is too low, much smaller than 0.1 %, the conclusion about R_{qd} needs to be re-evaluated in the light of more precise description of the TOTEM data, see in particular the subsequent Chapters 4 and 5.

3.5 The diquark scatters as a composite object

The collision of the two protons is illustrated in Fig. 3.4, in case the diquark scatters as a composite object including two constituent quarks. Bialas and Bzdak [10] supposed that the two quarks follow a Gaussian distribution inside the diquark

$$D\left(\vec{s_{q1}}, \vec{s_{q2}}\right) = \frac{1}{\pi d^2} e^{-\left(s_{q1}^2 + s_{q2}^2\right)/2d^2} \delta^2\left(\vec{s_{q1}} + \vec{s_{q2}}\right) , \tag{3.34}$$

where the transverse positions of the quarks are indicated with $\vec{s_{q1}}$, $\vec{s_{q2}}$. The distance d is the RMS of the separation of the quarks inside the diquark. It is defined as

$$d^2 = R_d^2 - R_q^2, \tag{3.35}$$

which expresses that the diquark is composed of two quarks which are separated by a distance d. In the present case the inelastic cross-sections σ_{qd}, σ_{dq} and σ_{dd} have to be factorized using the σ_{qq} inelastic cross-section using expansion (3.18). The formula for σ_{qd} and σ_{dq} is the following

$$\sigma_{qd}\left(\vec{s}\right) = \frac{4A_{qq}R_q^2}{R_d^2 + R_q^2} e^{-s^2 \frac{1}{R_d^2 + R_q^2}} - \frac{A_{qq}^2 R_q^2}{R_d^2} e^{-s^2/R_q^2}, \tag{3.36}$$

σ_{dd} is more complicated, and is given in details in Refs. [10, 11, 71–73]. The inelastic cross-section (3.14) can be calculated using the master formula (3.28) as before.

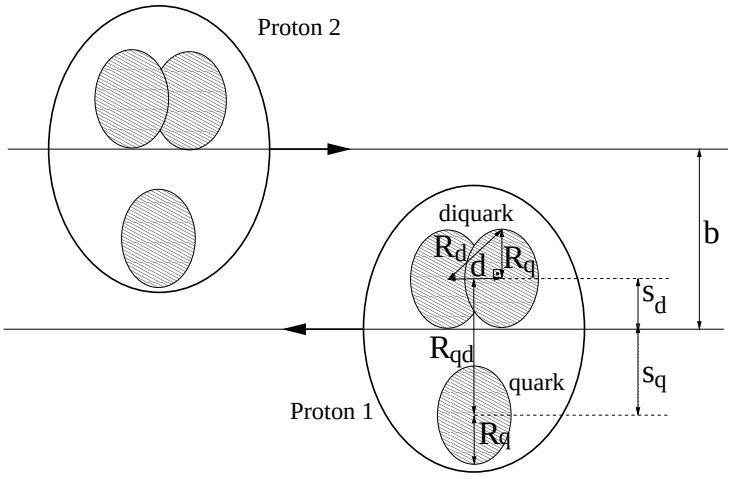

Figure 3.4: Snapshot about the two scattering protons in the $p = (q, (q, q))$ model. Protons are described as a quark-diquark system, where the diquark is assumed to scatter as a quark-quark composite object. This is an illustration only, actually all the model parameters follow a Gaussian distribution, based on Refs. [10, 11, 71–73].

In this subsection, similar MINUIT fit results are presented as in the previous subsection, the main modification is a change in the model assumption: now I assume that the diquark scatters as a composite object that contains two quarks. I present the final fit results to pp elastic scattering data both at ISR [1, 69] and at the LHC energy of $\sqrt{s} = 7$ TeV [35]. The results are illustrated in Fig. 3.5. The confidence levels, and model parameters with their errors are summarized in Table 3.2.

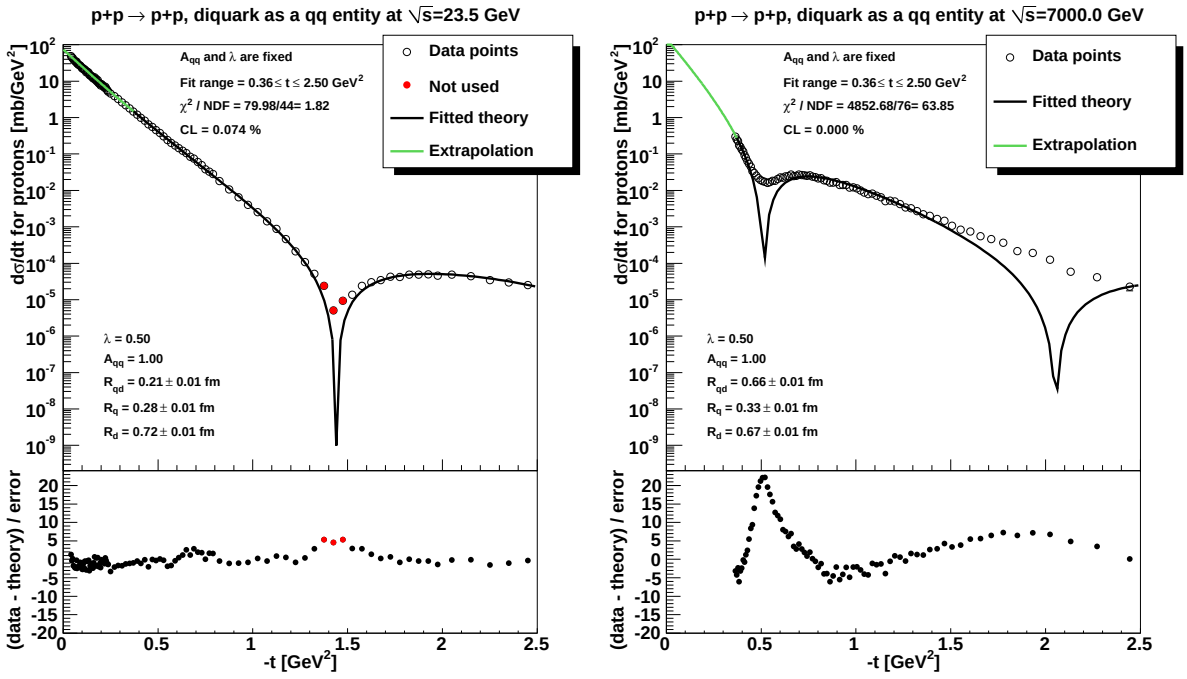

Figure 3.5: BB model fit result as Fig. 3.2, but the diquark is assumed to have a composite (q, q) substructure.

3.6 Inelastic cross-sections

The inelastic cross-sections for the quark-quark, quark-diquark and diquark-diquark subcollisions were analyzed on the basis of formula Eq. (3.20). The detailed results are collected in Table 3.3, while the average of these ratios for the described ISR energies are

$$\sigma_{qq} : \sigma_{qd} : \sigma_{dd} = 1 : (1.93 \pm 0.03) : (3.65 \pm 0.1)\,, \tag{3.37}$$

which is close to the ideal 1: 2 : 4 ratio, confirming the assumption of having two quarks inside the diquark, amended with some shadowing which is 4 % and 9 % respectively. At

$\sqrt{s}$ [GeV]	23.5	30.6	52.8	62.5	7000
R_{qd} [fm]	0.21 ± 0.01	0.23 ± 0.01	0.25 ± 0.01	0.23 ± 0.01	0.66 ± 0.01
R_q [fm]	0.28 ± 0.01	0.28 ± 0.01	0.28 ± 0.01	0.29 ± 0.01	0.33 ± 0.01
R_d [fm]	0.72 ± 0.01	0.74 ± 0.01	0.76 ± 0.01	0.76 ± 0.01	0.67 ± 0.01
χ^2/NDF	80.0/44	32.1/32	65.4/33	68.6/33	4852.7/76
CL [%]	0.07	46.30	0.07	0.03	0.0
σ_{elastic} [mb]	6.9 ± 0.1	6.6 ± 0.1	6.6 ± 0.1	7.2 ± 0.1	9.8 ± 0.1

Table 3.2: The BB model fit quality and resulting parameters of the fit at the ISR energies including the LHC result at $\sqrt{s} = 7$ TeV in the 0.36 to 2.5 GeV^2 $|t|$ fit range. The diquark is assumed to be a $d = (q, q)$ composit entity.

$\sqrt{s} = 7$ TeV the ratios are different from Eq. (3.37)

$$1 : (1.88 \pm 0.01) : (3.43 \pm 0.02)\,, \tag{3.38}$$

which shows that shadowing is stronger, 6 % and 14 % percent respectively, and a significant decrease compared to the ideal ratio can be observed.

$\sqrt{s}$ [GeV]	23.5	30.6	52.9	62.5	7000
σ_{qd}/σ_{qq}	1.92 ± 0.01	1.93 ± 0.01	1.93 ± 0.01	1.93 ± 0.01	1.88 ± 0.01
σ_{dd}/σ_{qq}	3.64 ± 0.02	3.66 ± 0.01	3.67 ± 0.01	3.65 ± 0.01	3.43 ± 0.02

Table 3.3: The ratios of the total inelastic cross-sections for the quark-quark, quark-diquark and diquark-diquark processes for the ISR and LHC energies using the composite diquark hypothesis.

3.7 Model comparison

The comparison of Table 3.1 and 3.4 shows that the fit quality is similar for both versions of the BB model. However, the best fit parameters are quite different at each colliding energy and the picture of the proton, as shown in Figs. 3.3 and 3.6, are also different. I found one combination of the model parameters, an effective radius that is obtained from the quadratic sum of R_q, R_d and R_{qd}, that seems to be the same in both models

$$R_{\text{eff}} = \sqrt{R_q^2 + R_d^2 + R_{qd}^2}\,, \tag{3.39}$$

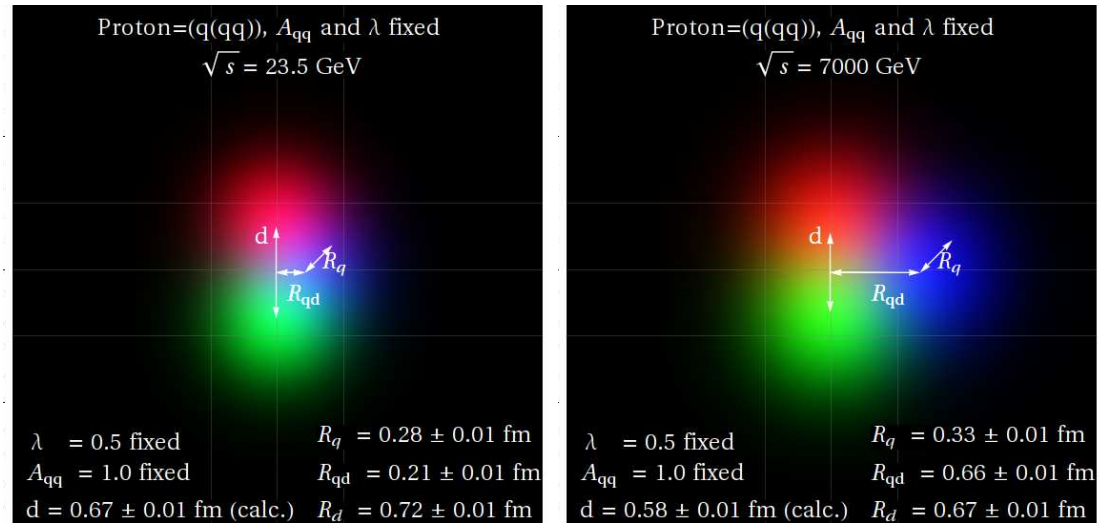

Figure 3.6: Visualization of the obtained R_{qd}, R_q and R_d BB model parameters when the diquark is assumed to be a qq entity. The proton seems to be much larger at the LHC energies than in the ISR regime. This is mainly due to an increase in the R_{qd} parameter, that characterizes the separation of the quark and the diquark, which is further decomposed as (q,q) state in this class of models. However, as the CL of the fit to the TOTEM data at $\sqrt{s} = 7$ TeV is too low, much smaller than 0.1 %, the conclusion about R_{qd} needs to be re-evaluated in the light of more precise description of the TOTEM data, see in particular the subsequent Chapters 4 and 5.

and which is related in a simple way to the measured total cross-section by

$$\sigma_{\rm tot} = 2\pi \cdot R^2_{\rm eff}\,. \tag{3.40}$$

The $\sqrt{s}$ dependence of the effective radius $R_{\rm eff}$ and the relationship between the effective radius and the measured total cross-section is shown in Fig. 3.7.

$\sqrt{s}\,[GeV]$	23.5	30.6	52.9	62.5	7000
data [mb]	38.94 ± 0.17	40.14 ± 0.17	42.67 ± 0.19	43.32 ± 0.23	98.3 ± 0.2
p=(q,d)					
$\sigma_{\rm tot}$ [mb]	38.5 ± 0.2	40.0 ± 0.2	42.5 ± 0.2	43.2 ± 0.3	79.0 ± 1.1
χ^2/NDF	107.2/45	62.2/33	110.7/34	56.1/34	4667.67/77
CL [%]	0.00	0.16	0.00	1.00	0.00
p=(q,(q,q))					
$\sigma_{\rm tot}$ [mb]	38.6 ± 0.1	39.7 ± 0.2	41.6 ± 0.2	42.6 ± 0.2	74.2 ± 1.3
χ^2/NDF	86.8/45	60.2/33	154.2/34	95.3/34	5059.57/77
CL [%]	0.02	0.26	0.00	0.00	0.00

Table 3.4: Measured and fitted BB model values of the total cross-sections, when the measured values of the total cross-sections are *included* into the earlier fitting procedure, as another, additional data point.

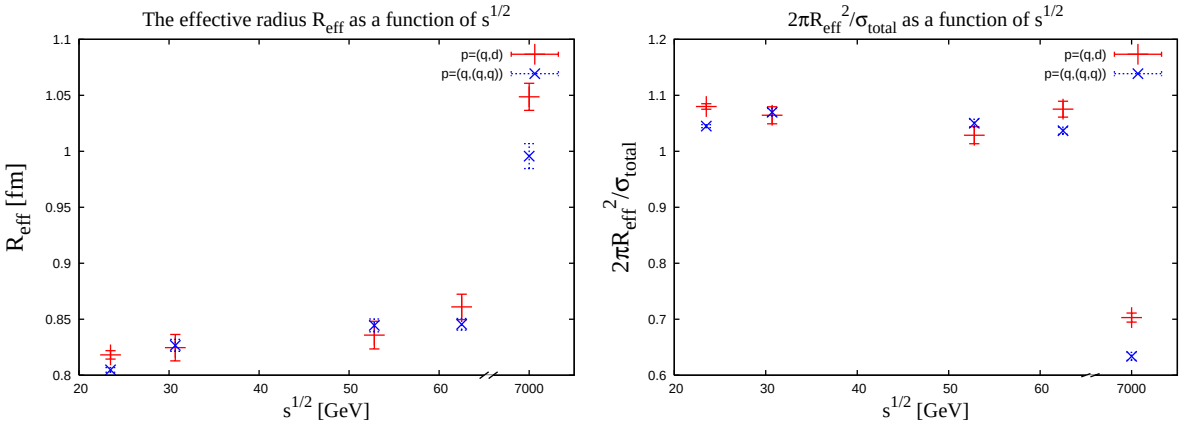

Figure 3.7: The effective radius parameter $R_{\rm eff}$ (left) and the quantity $2\pi \cdot R_{\rm eff}^2$ normalized with the measured total pp cross-section as a function of the center-of-mass energy $\sqrt{s}$.

3.8 Summary of Chapter 3

A systematic study of fit quality as well as the fit parameters under similar circumstances have been performed for the BB model [10] in a wide energy range from ISR to the LHC energies using the same kinematic interval and the same method at each energy. The model gives a good description of the ISR data, which means that the CL is acceptable on the ISR energies if 3 data points at the first diffractive minimum were left out from

the fit.

An important shortcoming of the quark-diquark BB model of protons is that it ignores the real part of the elastic scattering amplitude. This leads to a singular behavior at the diffractive minimum, which is apparently a more and more serious model limitation with increasing *pp* collision energy. Due to this reason, the BB model fails to describe in detail the structure of the first diffractive minimum at the LHC energies of $\sqrt{s} = 7$ TeV.

I found a combination of the BB model parameters, an effective radius that is obtained as the quadratic sum of quark, diquark radii and the separation between the quark and the center of mass of the diquark, that seems to be the same in both models and which is related in a simple, intuitive way to the measured total cross-section, as given by Eqs. (3.39) and (3.40).

Chapter 4

Perturbatively extended BB model

In the previous Chapter 3 I have fitted the original BB model to ISR and LHC energies. In this Chapter 4 the BB model of elastic pp scattering is generalized to the case when the real part of the parton-parton level forward scattering amplitude is non-vanishing, which enables the model to describe well the dip region of the differential cross-section of elastic scattering at the ISR energies, and improves significantly the ability of the model to describe also the recent TOTEM data at $\sqrt{s} = 7$ TeV LHC energy. The presentation of the results in this Chapter 4 follows the lines of Ref. [12].

The expression for the profile function $t_{\rm el}$ of Eq. (3.9) is derived from the unitarity relation Eq. (3.4) and allows one to introduce a real part to the FSA in a systematic way. At the beginning of our data analysis, using the BB model, I have assumed that the real part of the FSA is small enough to provide it in a perturbative way. Thus, in the so-called αBB model, I introduced the real part of the FSA with a purely imaginary factor using a new parameter α

$$\tilde{\sigma}_{{\rm inel},\alpha}(s,b) = (1 - {\rm i}\,\alpha)\,\tilde{\sigma}_{\rm inel}(s,b)\,. \tag{4.1}$$

The new parameter α is determined from the analysis of data. Note, that the $\alpha = 0$ case corresponds to a situation, when the proton always scatters elastically if its constituents scatter elastically. Parameter α is introduced in a way that is motivated by the α parameter of the Glauber-Velasco model of Refs. [74, 75].

Using the parametrization for $\tilde{\sigma}_{{\rm inel},\alpha}(s,b)$ of Eq. (4.1) the profile function of the original

BB model, see Eq. (3.8), is modified

$$t_{\rm el}(s,b) = \mathrm{i}\left[1 - \sqrt{1 - \tilde{\sigma}_{\rm inel,\alpha}(s,b)}\right] , \tag{4.2}$$

where the profile function $t_{\rm el}(s,b)$ is a complex valued function in this case.

In this section the results of our MINUIT fits with the αBB model are presented for the ISR [1, 69] and TOTEM [6, 35] pp elastic scattering data. The scenario when the diquark is assumed to scatter as a single entity is considered first, which is followed by the fit results for the case when the diquark is considered as composite object. To provide a fair comparison among the model descriptions on the different dataset at different $\sqrt{s}$, the $|t|$ region of the fits is limited to the first TOTEM publication. In the discussion section, the fit quality is also studied in special fits to the TOTEM data in the low $|t|$ region. As we shall see, even the αBB model cannot describe the TOTEM data in the whole $|t|$ region.

The results show that thanks to the new parameter α, which generates the real part of the forward scattering amplitude, the fits improve significantly and describe the data also in the dip region, as compared to the $\alpha = 0$ case presented in Refs. [10, 11, 71–73]. This phenomenon can be interpreted such that the proton does not necessarily scatter elastically even if all its constituents are scattered elastically. This effect is small at lower collision energies, however it becomes more and more prominent with increasing energies.

4.1 The diquark is assumed to scatter as a single entity

In this subsection the fit results are collected in case the diquark is assumed to scatter as a single entity. This version of the model was fitted to the pp elastic scattering data both at ISR [1, 69] and at LHC [35] energy as well. The αBB model is fitted with Eq. (3.31) without the use of the luminosity error. The results are illustrated in Fig. 4.1 and a visualization of the model parameters is provided in Fig. 4.2. The confidence levels, and model parameters with their errors are summarized in Table 4.1.

The figures contain two phenomenological relations below the legend, the effective radius $R_{\rm eff}$ of Eq. (3.39) and also the relation Eq. (3.40) calculated from the αBB model.

This formula was originally proposed for the BB model in [11], and was found to be model independently valid in both the $p = (q, d)$ and in the $p = (q, (q, q))$ models with a precision of $10 - 15\%$. Here I validate this formula for the $\alpha \neq 0$ case.

Numerically, I have found another phenomenological formula, which indicates that the $|t|$ position of the first diffractive minimum $|t_{\rm dip}|$ multiplied with the total cross-section $\sigma_{\rm tot}$ is nearly constant

$$\frac{|t_{\rm dip}| \cdot \sigma_{\rm tot}}{C} \approx 1, \tag{4.3}$$

where $C = 54.8 \pm 0.7\,\text{mb GeV}^2$. The test of these relations for each energy with both the $p = (q, d)$ and $p = (q, (q, q))$ models is given on the figures and the results are collected and described in our Discussion part.

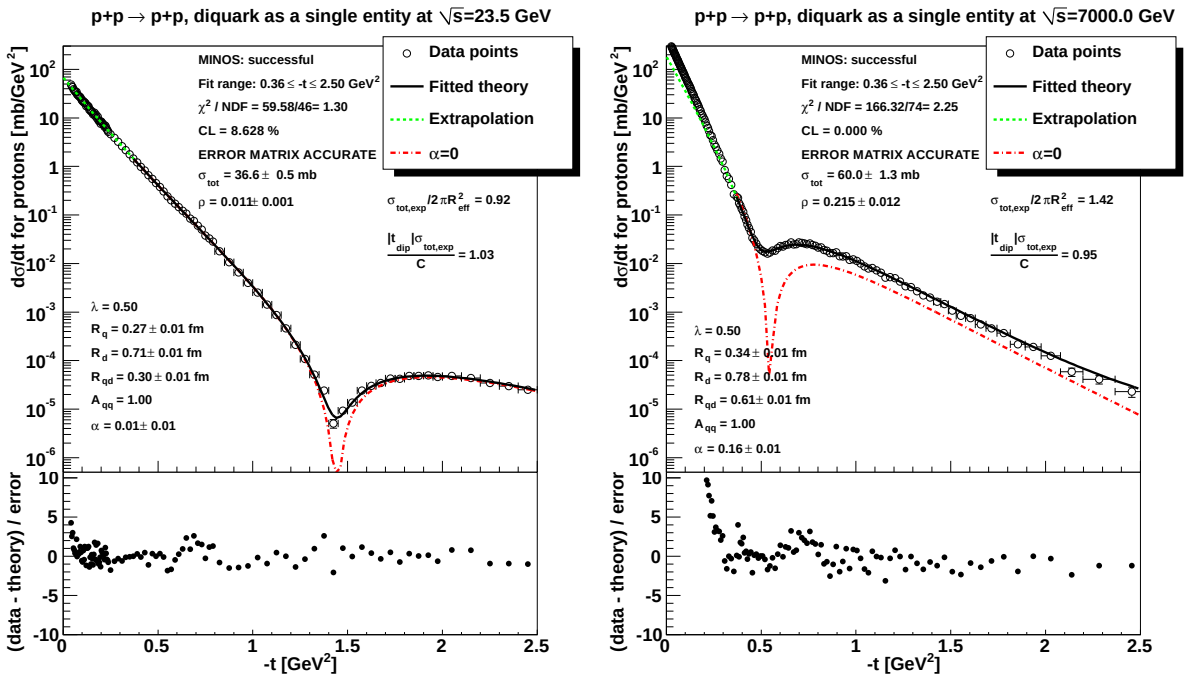

Figure 4.1: αBB fit result at ISR energy of $\sqrt{s} = 23.5$ GeV (left) and LHC energy of $\sqrt{s} = 7$ TeV (right) in the 0.36 to 2.5 GeV^2 $|t|$ fit range in case the diquark is assumed to be a single entity. Note that although α is not significantly different from 0, a tiny value of α makes the fit behavior in the dip region significantly better, than the $\alpha = 0$ case, indicated by a dashed line, see also the corresponding result with the BB model in Fig. 3.2. The total cross-section $\sigma_{\rm tot,exp}$ is from Ref. [6].

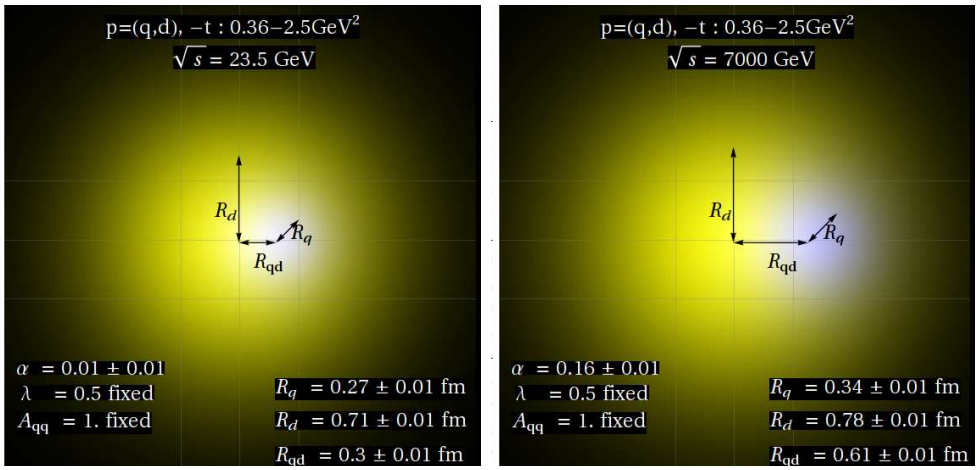

Figure 4.2: Visualization of the αBB fit results of Fig. 4.1.

$\sqrt{s}$ [GeV]	23.5	30.7	52.8	62.5	7000
R_q [fm]	0.27 ± 0.01	0.25 ± 0.01	0.26 ± 0.01	0.29 ± 0.01	0.34 ± 0.01
R_d [fm]	0.71 ± 0.01	0.71 ± 0.01	0.73 ± 0.01	0.77 ± 0.01	0.78 ± 0.01
R_{qd} [fm]	0.30 ± 0.01	0.34 ± 0.01	0.35 ± 0.01	0.29 ± 0.01	0.61 ± 0.01
α	0.01 ± 0.01	0.01 ± 0.01	0.02 ± 0.01	0.01 ± 0.01	0.16 ± 0.01
χ^2/NDF	59.58/46	29.89/34	62.29/35	52.09/35	166.32/74
CL [%]	8.63	66.94	0.30	3.16	0.00

Table 4.1: The $\sqrt{s}$ dependence of the confidence levels and the αBB fit parameters obtained in the 0.36 to 2.5 GeV^2 $|t|$ fit range in case the diquark is assumed to be a single entity.

4.2 The diquark scatters as composite object

The MINUIT fit results of the αBB model are presented as in the previous subsection, except that it is assumed that the diquark scatters as a composite object which contains two quarks. This version of the model was fitted to the pp elastic scattering data both at ISR [1, 69] and at LHC [35] energy as well. The results are illustrated in Fig. 4.3, while the visualization of the obtained parameters is given in Fig. 4.4. The confidence levels, and model parameters with their errors are summarized in Table 4.2.

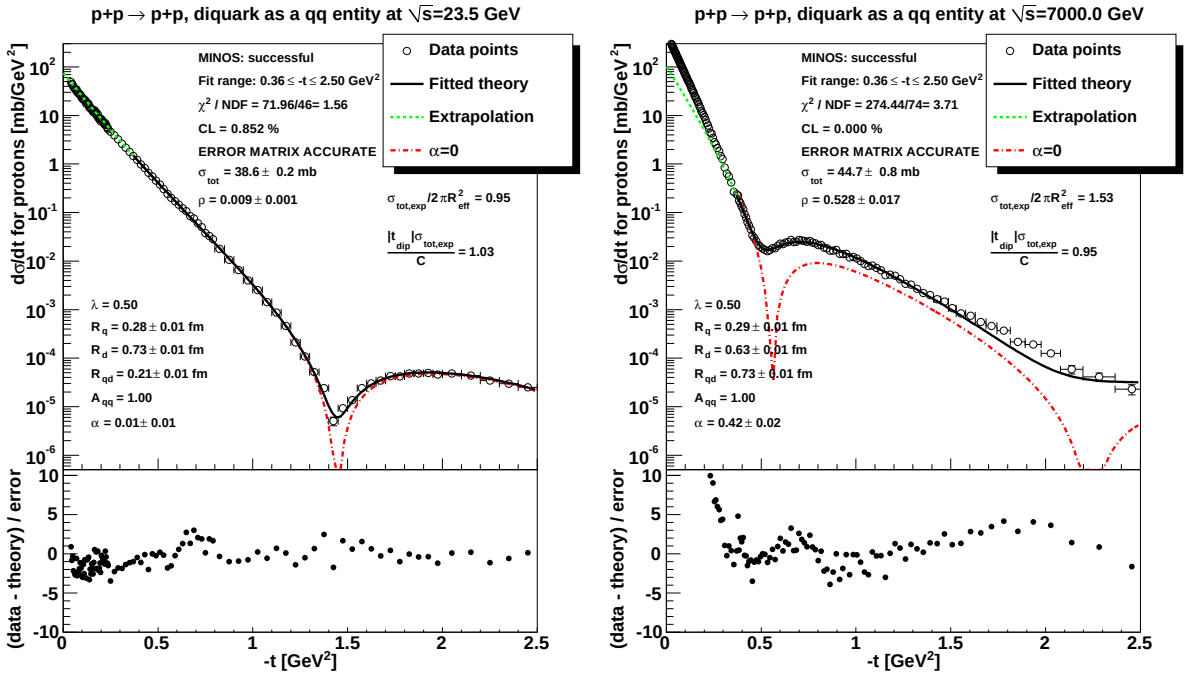

Figure 4.3: αBB fit result at ISR energy of $\sqrt{s} = 23.5$ GeV (left) and LHC energy of $\sqrt{s} = 7$ TeV (right) in the 0.36 to 2.5 GeV^2 $|t|$ fit range in case the diquark is assumed to be a composite object. Dashed line indicates the fit result when the parameter α is set to zero, see also the BB model fit result in Fig. 3.5.

$\sqrt{s}$ [GeV]	23.5	30.7	52.8	62.5	7000
R_q [fm]	0.28 ± 0.01	0.28 ± 0.01	0.28 ± 0.01	0.29 ± 0.01	0.29 ± 0.01
R_d [fm]	0.73 ± 0.01	0.74 ± 0.01	0.76 ± 0.01	0.76 ± 0.01	0.63 ± 0.01
R_{qd} [fm]	0.21 ± 0.01	0.23 ± 0.01	0.25 ± 0.01	0.23 ± 0.01	0.73 ± 0.01
α	0.01 ± 0.01	0.00 ± 0.01	0.02 ± 0.01	0.01 ± 0.01	0.42 ± 0.02
χ^2/NDF	71.96/46	38.47/34	48.96/35	82.00/35	274.44/74
CL [%]	0.85	27.42	5.88	0.00	0.00

Table 4.2: The $\sqrt{s}$ dependence of the confidence levels and the αBB fit parameters in case the diquark is assumed to be a composite entity. Note that the quark-diquark distance R_{qd} increases significantly at the LHC, but note also that the fit quality is not statistically acceptable at $\sqrt{s} = 7$ TeV.

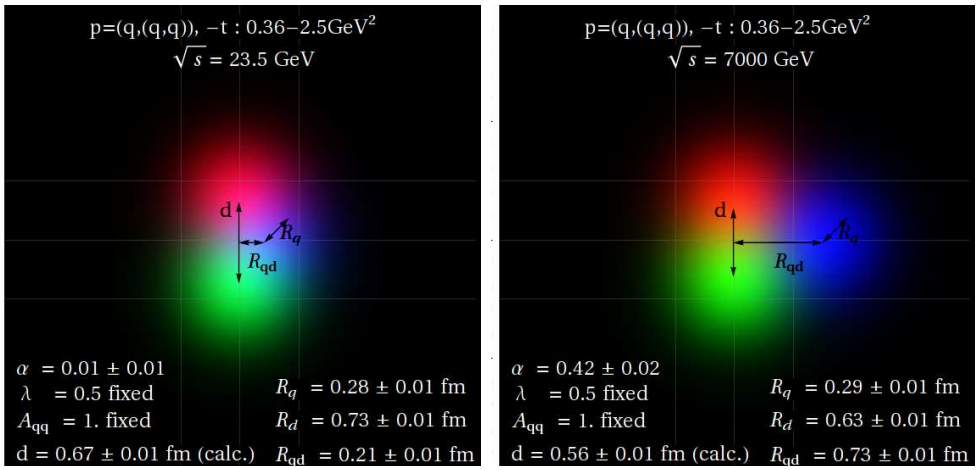

Figure 4.4: Visualization of the αBB fit results of Fig. 4.3.

4.3 Total cross-section estimation based on low-$|t|$ TOTEM data

Note that even the generalized αBB model failed on the TOTEM data when it was fitted in the $0.36 \leq -t \leq 2.5$ GeV^2 region. In this section I investigate the fit range dependence of this negative result. The total cross-section is estimated based on the small $|t|$ data which was measured by the TOTEM experiment. The fit is repeated in a low $|t|$ range of $0.0 \leq -t \leq 0.8$ GeV^2 and the total cross-section value is *included* into the fits as one additional data point to show how well it can be described by the αBB model. The results are illustrated in Fig. 4.5.

In the low $|t|$-range a reasonable description cannot be achieved with the single entity version of the model, neither in the case when the diquark is assumed to be composite. In addition, when the fits are limited to the low $|t|$ region, the extrapolated fit curves deviate from the data significantly in the large $|t|$ region for both the $p = (q, d)$ and the $p = (q, (q, q))$ model.

Note also that I could not find a fit with statistically acceptable quality, when the fit region was increased to $0.0 \leq -t \leq a$ GeV^2, where $a > 0.8$ GeV^2. This indicates that the αBB model does not describe TOTEM elastic scattering data in the whole measured t range.

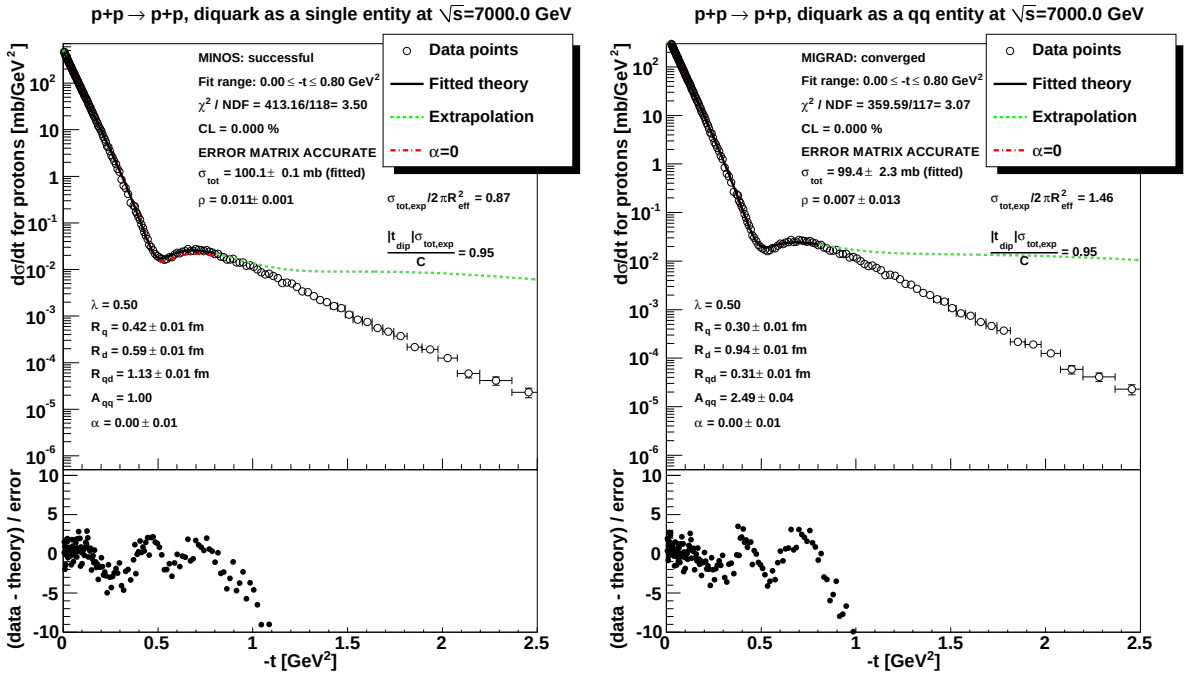

Figure 4.5: αBB fit result at $\sqrt{s} = 7$ TeV in the low $|t|$ range of $0.0 \leq -t \leq 0.8$ GeV^2, including the measured total cross-section value, as additional data point. The diquark is assumed to be a single entity (left) and a composite object (right). Both fits are unsatisfactory, $CL < 0.1$ %.

4.4 Discussion of the αBB model results

The comparison between the αBB model results, shown in Figs. 4.1 and 4.3, and the ones made with the original BB model, given in Figs. 3.2 and 3.5, shows that the αBB model significantly improves the description of the dip region.

Although the αBB model fit quality improved and become reasonable in the dip region, I still could not find a reasonable description of the TOTEM dataset, that would work both in the low-$|t|$, in the dip and in the large-$|t|$ region. For example, if the low-$|t|$ region is not included in the fit, this region is under-estimated by the extrapolated curve and also the total cross-section is under-estimated by 17.7 %. Fig. 4.5 indicates, that if I include the measured total cross-section to the fit as an additional data point, but still keeping the fitted t range to $0.16 \leq |t| \leq 2.5$ GeV^2, the description improves at the low values of $|t|$ but the fit deviates more from the data in the dip region. The radius parameter of the quarks R_q and that of the diquarks R_d together with the quark-diquark distance R_{qd}

increase after adding the measured total cross-section.

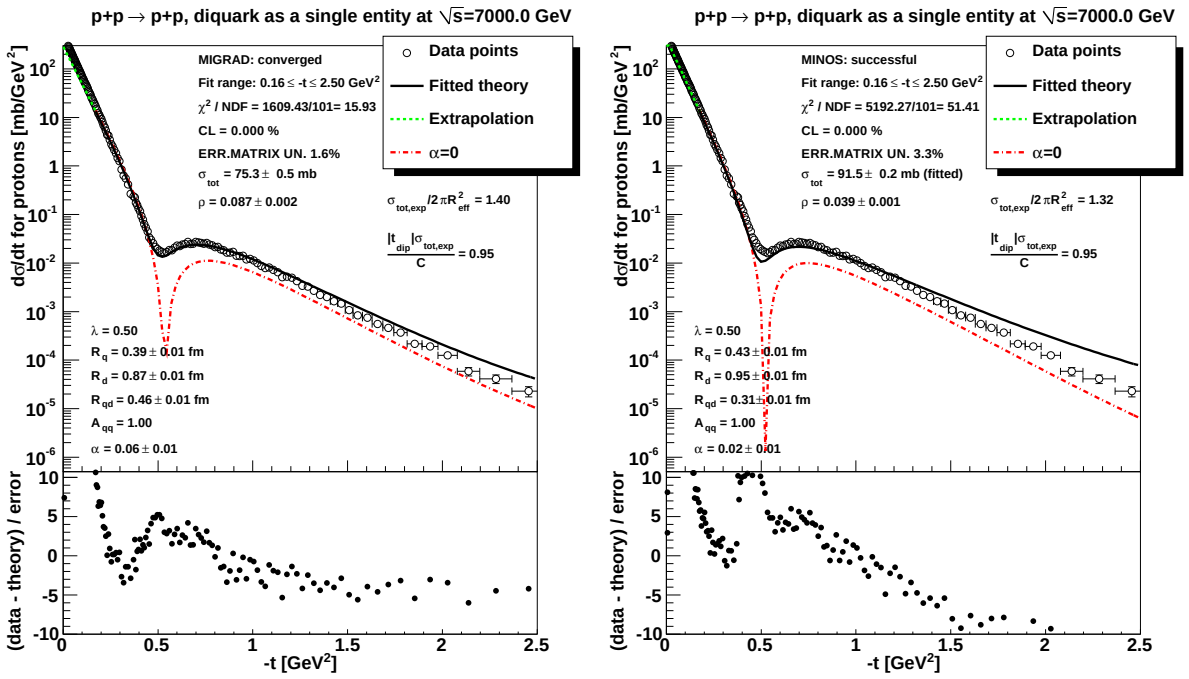

Figure 4.6: αBB fit result at $\sqrt{s} = 7$ TeV in the $0.16 \leq -t \leq 2.5$ GeV^2 range shown on the left hand side plot. The case when the measured total cross-section is added to the fit as one additional data point is shown on the right hand side plot. The diquark is assumed to be a single entity.

Although parameter α is introduced to have a successful data description at the dip region, and it can be considered as the ρ parameter Eq. (3.13) of parton-parton level scattering, our method to introduce α is based on an analogy with the Glauber-Velasco model and can be considered valid in the leading order, $|\alpha| << 1$ limit only.

The α parameter as a function of $\sqrt{s}$ is plotted in Fig. 4.7, which shows the increasing role of this parameter at LHC energies. The increase of α can be interpreted as the proton becomes more and more fragile with increasing $\sqrt{s}$.

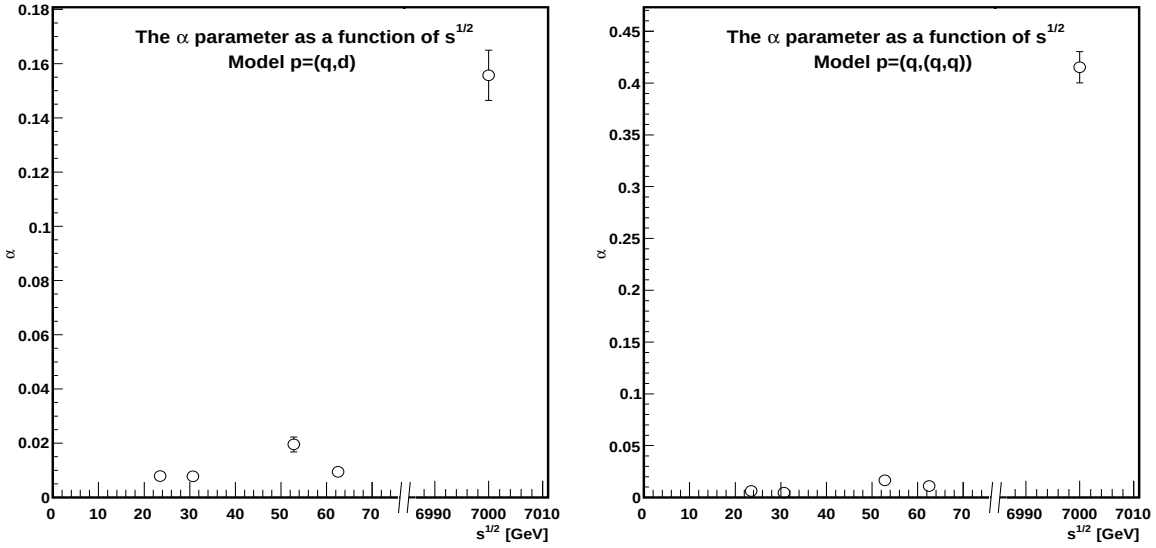

Figure 4.7: The $\sqrt{s}$ dependence of the parameter α using the αBB model fit results. This plot shows, that α becomes more important at LHC energies, than at ISR, indicating that it is more probable at LHC that a proton does not scatter elastically even if all of its constituents happened to scatter elastically. According to these results, the pp collisions become more and more "fragile" with increasing $\sqrt{s}$.

The phenomenological relation Eq. (4.3), which relates the position of the first diffractive minimum $t_{\rm dip}$ and the total cross-section, is model independent, and well satisfied for both ISR and LHC energies, according to Table 4.5 and Fig. 4.8. The relation Eq. (4.3) is motivated by the formulae of photon scattering on a black disk with radius $R_{\rm black}$, where the elastic differential cross-section is given with [2, 76]

$$\frac{{\rm d}\sigma_{\rm black}}{{\rm d}t} = \pi R_{\rm black}^4 \left[\frac{J_1(qR_{\rm black})}{qR_{\rm black}}\right]^2 , \tag{4.4}$$

with $q = \sqrt{-t}$, and the total cross-section of the scattered light on the black disk can be calculated with the optical theorem [2]

$$\sigma_{\rm tot,black} = 2\pi R_{\rm black}^2 \, . \tag{4.5}$$

In this simple theoretical model the position of the first diffractive minimum, following from Eq. (4.4), and the total cross-section Eq. (4.5) satisfies

$$C_{\rm black} = |t_{\rm dip,black}| \cdot \sigma_{\rm tot,black} = 2\pi \cdot j_{1,1}^2 (\hbar c)^2 \approx \ 35.9\,{\rm mb\ GeV}^2 \, , \tag{4.6}$$

where $j_{1,1}$ is the first root of the Bessel function $J_1(x)$.

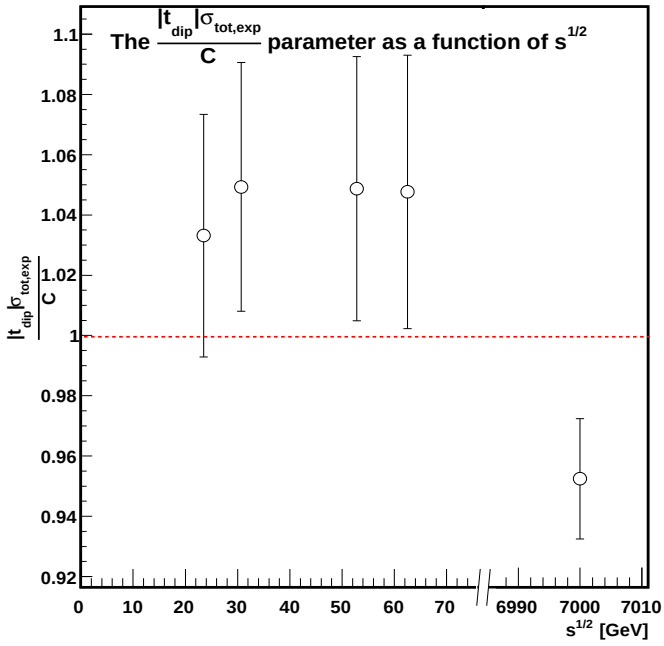

Figure 4.8: The $\frac{|t_{\rm dip}|\cdot\sigma_{tot,exp}}{C}$ ratio, directly obtained from experimental data. The dashed line indicates the ratio 1.

In case of the phenomenological relation Eq. (4.3) the constant C was fitted to the measured data, to obtain the best possible description. It is clear that this fitted constant $C = 54.8 \pm 0.7\,\text{mb GeV}^2$ is significantly different from the number $C_{\rm black}$ of Eq. (4.6) one may expect from light scattering on a black disc.

In this sense, although Eq. (4.3) is satisfied by ISR as well as TOTEM data, the value of the constant indicates a more complex scattering phenomena, than the photon black disc scattering, mentioned above.

The observed $|t_{\rm dip}|\cdot\sigma_{\rm tot} \approx C$ relationship may in fact be a reflection of a deeper scaling property of the differential cross-section of elastic pp scattering. To guide our intuition, it is again useful to consider the scattering of light on a black disk. The differential cross-section Eq. (4.4) can be written as

$$\frac{\mathrm{d}\sigma_{\rm black}}{\mathrm{d}t} = \frac{\sigma_{\rm tot,black}}{2|t|} J_1\left(\sqrt{\frac{|t|\sigma_{\rm tot,black}}{2\pi}}\right)^2 . \tag{4.7}$$

The result Eq. (4.7) can be scaled to a universal scaling curve

$$\frac{|t|}{\sigma_{\text{tot,black}}}\frac{\mathrm{d}\sigma_{\text{black}}}{\mathrm{d}t} = \frac{1}{2}J_1\left(\sqrt{\frac{y}{2\pi}}\right)^2 = F_{\text{black}}(y), \tag{4.8}$$

where $F_{\text{black}}(y)$ is a dimensionless function of the variable $y = |t| \cdot \sigma_{\text{tot,black}}$, and is the same for all black discs regardless of their radius. The function $F_{\text{black}}(y)$ can be expressed in terms of the dimensionless variable $z = |t|/|t_{\text{dip,black}}| = y/C_{\text{black}}$. From Eq. (4.6) and Eq. (4.8)

$$\frac{|t||t_{\text{dip,black}}|}{C_{\text{black}}}\frac{\mathrm{d}\sigma_{\text{black}}}{\mathrm{d}t} = \frac{1}{2}J_1\left(\sqrt{\frac{zC_{\text{black}}}{2\pi}}\right)^2 = G_{\text{black}}(z)\,, \tag{4.9}$$

Both of the above dimensionless functions can be generalized to the real experimental case, leading to $F(y)$ and $G(z)$, where $y = |t|\sigma_{\text{tot}}$ and $z = y/C$. I have thus plotted both the $F(y)$ and the $G(z)$ functions for all the ISR and LHC data available for us. The results are shown in Fig. 4.9, where the scaling functions of the black disc $F_{\text{black}}(y)$ and $G_{\text{black}}(z)$ are also presented. The plots indicate, that ISR and LHC data on $\mathrm{d}\sigma/\mathrm{d}t$ approximately satisfy these newly found scaling relation, but with some scaling violating terms.

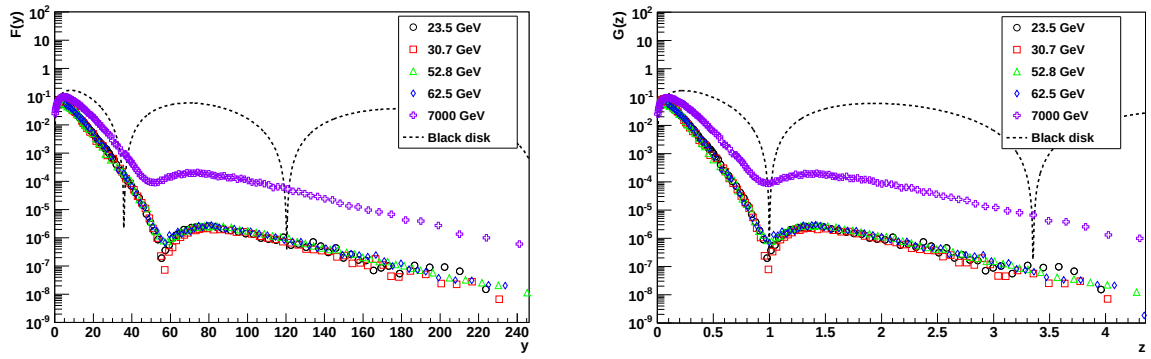

Figure 4.9: The $F(y)$ and $G(z)$ scaling functions showing the ISR and TOTEM data. The scaling functions of the black disc $F_{\text{black}}(y)$ and $G_{\text{black}}(z)$ are also shown.

The data indicate that the pp elastic differential cross-section $\mathrm{d}\sigma/\mathrm{d}t$ data collapse to an energy independent scaling function at the ISR energies of $\sqrt{s} = 23.5 - 62.5$ GeV, and data at $\sqrt{s} = 7$ TeV are significantly and qualitatively different, move closer to the scaling functions that characterize the black disc limit. However, even at $\sqrt{s} = 7$ TeV, the data are significantly different from the scaling function of the black disc limit. In particular, the secondary minimum of the black disc limit is not observed, so scaling violating terms

are still important. It remains to be seen if this trend of approaching better the black disc limit continues with increasing colliding energies, or not. Plotting the $F(z)$ and the $G(z)$ scaling functions seems to be a useful tool to investigate, to understand how the data approach this possible limiting behaviour.

$\sqrt{s}$ [GeV]	23.5	30.7	52.8	62.5	7000
ρ	0.01 ± 0.01	0.01 ± 0.01	0.03 ± 0.01	0.01 ± 0.01	0.21 ± 0.01
$\sigma_{\rm tot,exp}/(2\pi R^2_{\rm eff})$	0.92 ± 0.01	0.93 ± 0.03	0.95 ± 0.03	0.91 ± 0.03	1.42 ± 0.05

Table 4.3: The ρ parameter and the $\sigma_{\rm tot,exp}/(2\pi R^2_{\rm eff})$ ratio in case the diquark is assumed to be a single entity. Fit range is the same $0.36 \leq -t \leq 2.5$ GeV^2 for all datasets. Note that the fit quality is not acceptable at $\sqrt{s} = 7$ TeV.

$\sqrt{s}$ [GeV]	23.5	30.7	52.8	62.5	7000
ρ	0.01 ± 0.01	0.01 ± 0.01	0.02 ± 0.01	0.02 ± 0.01	0.53 ± 0.02
$\sigma_{\rm tot,exp}/(2\pi R^2_{\rm eff})$	0.95 ± 0.01	0.93 ± 0.01	0.94 ± 0.01	0.96 ± 0.01	1.53 ± 0.06

Table 4.4: The ρ parameter and the $\sigma_{\rm tot,exp}/(2\pi R^2_{\rm eff})$ ratio, the diquark is assumed to be a composite entity. Fit range is the same $0.36 \leq -t \leq 2.5$ GeV^2 for all datasets. Note that the fit quality is not acceptable at $\sqrt{s} = 7$ TeV.

$\sqrt{s}$ [GeV]	23.5	30.7	52.8	62.5	7000
$\frac{\lvert t_{\rm dip}\rvert\, \sigma_{tot,exp}}{C}$	1.03 ± 0.04	1.05 ± 0.04	1.05 ± 0.04	1.05 ± 0.05	0.95 ± 0.02

Table 4.5: The $\frac{|t_{\rm dip}|\,\sigma_{\rm tot,exp}}{C}$ ratio, model independently. Precise up to 5 % (within errors).

One can ask the question, why and at what range of squared four-momentum transfer $|t|$ such a simple model should work. Apparently, for sufficiently large $|t|$ one starts to probe a distance that becomes smaller than 0.2 fm, the size of a constituent quark in the Bialas-Bzdak picture, or, the even larger diquark scale. Thus, for a large enough $|t|$ the simple Bialas-Bzdak model, and even its generalized version presented in the current manuscript, are expected to fail.

4.5 Summary of Chapter 4

In this work I have generalized the geometrical Bialas-Bzdak model of elastic pp scattering by allowing for a real part of the forward scattering amplitude using the same geometrical picture, but assuming that a pp scattering may become inelastic even in the case when all scattering of the constituents of the colliding protons is elastic (but not completely collinear). This generalization, the αBB model, resulted in a successful description of the dip region of elastic pp scattering in the ISR energy region and resulted in a significant, qualitative improvement of the ability of this model to describe elastic pp scattering at $\sqrt{s} = 7$ TeV colliding energy as measured by the TOTEM Collaboration. The comparison between the αBB model results, see Fig. 4.1 and 4.3 also Fig. 4.6, and the BB model ones, given in Figs. 3.2 and 3.5, clearly shows that I have improved significantly on the description of the dip region using the αBB model.

I have also found that the αBB model is able to describe only the small $|t|$ data set and therefore the total cross-section $\sigma_{\rm tot}$ at LHC, if the fit range is limited to a relatively low $|t|$ range. However, even the αBB model model fails, if the large $|t|$ region data of TOTEM is included, more precisely I find no good quality fits in the $0.0 \leq -t \leq a$ GeV^2 region, where $a \geq 0.8$ GeV.

Based on the geometrical picture behind the Bialas-Bzdak model, I have identified and tested the validity of two simple phenomenological formulas. Our first formula relates the total pp scattering cross-section to an effective radius, that is the quadratic sum of the radii of a quark and a diquark as well as the distance between the center of mass of the diquark and the quark inside the proton. Regardless of the detailed structure of the diquarks, and independently of the values of the real part of the forward scattering amplitude, this formula gives a model independent estimate for the total cross-section with a typical 10 % precision at ISR energies, that becomes worse at LHC energies.

Our second formula establishes a relation between the total cross-section of pp scattering and the position of the dip in the differential cross-section, see Fig. 4.8 and Table 4.5. In particular, I find that the product of these two quantities is a model independent constant. I also demonstrated that this formula is remarkably precise, it is satisfied by the ISR data within one standard deviations, while at LHC the formula is also satisfied by the data within 3 standard deviations.

Chapter 5

The ReBB model

I have learnt from the analysis of the ISR and $\sqrt{s} = 7$ TeV TOTEM data at LHC, explained in Chapters 3 and 4, that the real part of the FSA is perturbatively small at ISR energies, it becomes non-perturbative at LHC but the scattering is still dominated by the imaginary part of the scattering amplitude. In this Chapter I apply the consequence Eq. (3.9) of the unitarity constraint Eq. (3.4) which provides a simple way to handle the real part of the FSA at LHC. According to Eq. (3.9), in this case one has to define $\mathrm{Im}\,\Omega(s,b)$.

I have studied several possible choices. One possibility is to introduce the imaginary part of the opacity function so that it is proportional to the probability of inelastic scatterings, which is known to be a decreasing function of the impact parameter b. A possible interpretation of this assumption may be that the inelastic collisions arising from non-collinear elastic collisions of quarks and diquarks follow the same spatial distributions as the inelastic collisions of the same constituents

$$\mathrm{Im}\,\Omega(s,b) = -\alpha \cdot \tilde{\sigma}_{\mathrm{inel}}(s,b)\,, \tag{5.1}$$

where α is a real number, corresponding to the shape parameter of the differential cross-section of elastic pp scattering.

The above proportionality Eq. (5.1) between $\mathrm{Im}\,\Omega(s,b)$ and $\tilde{\sigma}_{\mathrm{inel}}(s,b)$ provided the best fits from among the relations that I have tried but it is far from being a unique possibility for an ansatz. Note, that the $\alpha = 0$ case corresponds to the $p = (q,d)$ version of the original BB model of Chapters 3 and Ref. [10], where the FSA has a vanishing real part.

In the $\alpha < 0.1$ perturbative limit the αBB model of Ref. [12] can also be obtained as follows. The αBB model can be defined by the relation

$$\mathrm{Im}\,\Omega(s,b) = \frac{\alpha \cdot \tilde{\sigma}_{\mathrm{inel}}(s,b)}{\tilde{\sigma}_{\mathrm{inel}}(s,b) - 2}\,. \tag{5.2}$$

This definition is equivalent to the original form of the definition of the αBB model in Ref. [12] where $\sigma_{\mathrm{inel}}(s,b)$ in Eq. (3.8) was allowed to have a small imaginary part, in the form of $\sigma_{\mathrm{inel}}(s,b) \;\to\; (1+i\alpha)\cdot\sigma_{\mathrm{inel}}(s,b)$. This condition was satisfied for fits at ISR energies, with $\alpha \approx 0.01$, however, at LHC energies the αBB model did not describe the TOTEM data in a satisfactory manner [12].

I have also investigated the assumption that the real and the imaginary parts of the opacity function are proportional to one another

$$\mathrm{Im}\,\Omega(s,b) = -\alpha \cdot \mathrm{Re}\,\Omega(s,b)\,. \tag{5.3}$$

However, as the results using Eq. (5.3) were less favorable than the results obtained with Eq. (5.1), I do the data analysis part, described in the next section, using Eq. (5.1). I mention this possibility to highlight that here some phenomenological assumptions are necessary as the ReBB model does allow for a broad range of possibilities for the choice of the imaginary part of the opacity function.

In this way, the ReBB model is fully defined, and applying convention Eq. (3.33) at a given colliding energy only four parameters have to be fitted: the three geometrical parameters R_q, R_d, R_{qd} and parameter α of Eq. (5.1).

I have studied the version when the diquark is assumed to be a composition of two quarks, referred as the $p = (q,(q,q))$, see Section 3.5. Our earlier studies using the αBB model indicated [12], that the $p = (q,d)$ case gives somewhat improved confidence levels as compared to the $p = (q,(q,q))$ case. So I discuss ReBB results with the $p = (q,d)$ scenario only, however, it is straightforward to extend the investigations to the $p = (q,(q,q))$ case. I have performed these calculations but the details are not presented here as the results are not acceptable at $\sqrt{s} = 7$ TeV. To demonstrate that the $p = (q,(q,q))$ model does not work, I report only the rather unsatisfactory fit quality when the data analysis is discussed.

5.1 Fit results with the ReBB model

The ReBB model, defined with Eqs. (3.9) and (5.1), was fitted to the data at ISR energies and at LHC energy of $\sqrt{s} = 7$ TeV. The relation between the imaginary part of $\Omega(s, b)$ and α is defined with Eq. (5.1). In the course of the minimization of the ReBB model I take into account the uncertainty of the overall scale factor of the measured data, with the χ^2_{lumi} function of Eq. (3.32).

First I attempted to fit the ReBB model in the $0 < |t| < 2.5$ GeV^2 range, fitting simultaneously both the low-$|t|$ TOTEM measurement of Ref. [68] and the one containing the dip region [35], see Fig. 5.1.

Note, that in this particular fit two normalization parameter were used in the χ^2_{lumi} function Eq. (3.32): γ_1 below and γ_2 above $|t_{\text{sep}}|$, since the pp elastic differential cross-section data measured by the TOTEM experiment at $\sqrt{s} = 7$ TeV is a compilation of two subsequent measurements [6, 35, 68], which are (almost) independent measurements. The squared four-momentum transfer value $t_{\text{sep}} = -0.375$ GeV^2 separates the two data sets.[1] Note also, that the two datasets were taken with two very different settings of the machine optics of the LHC accelerator.

This fit provides $\chi^2/\text{NDF} = 289.04/158 = 1.83$ and $CL = 9 \times 10^{-9} \ll 0.1\%$, which is statistically not an acceptably good fit quality, although, as indicated in Fig. 5.1, the fit looks reasonably good by eye. So, unfortunately, I could not get a unified and statistically acceptable description of the differential cross-section of elastic pp scattering in the whole measured squared four-momentum transfer t interval using the ReBB model.

It is important to note, however, that I determined the fit quality using the statistical and the luminosity uncertainty only, where the latter is a t-independent systematic uncertainty. According to the original TOTEM publications [35, 68], the systematic uncertainties of the two TOTEM data sets are very different due to different data taking conditions, especially due to the different LHC machine optics. The t-dependent part of the systematic errors allow the data points, as a function of $|t|$, to be slightly moved in a correlated and t dependent way, which could, in principle, improve our fit quality.

However, this part of the systematics is rather difficult to handle correctly in the

[1] The squared four-momentum transfer value t_{sep} separates the bin centers at the common boundary, the two bins actually overlap [6, 35, 68].

present analysis. So I decided to analyze the two TOTEM data sets separately. If the *separated* fits to $\sqrt{s} = 7$ TeV elastic differential cross-section $\mathrm{d}\sigma/\mathrm{d}t$ data are evaluated, below and above the separation $|t_{\mathrm{sep}}|$, quality results can be obtained, which are shown in Figs. 5.2 and 5.3, and are summarized in Table 5.1. As detailed below, this strategy leads to reasonable fit qualities (CL = 1.8 %, statistically acceptable fit in the cone region and CL = 0.04 %, statistically marginal fit in the dip region), with a remarkable stability of fit parameters.[2]

$\sqrt{s}$ [GeV]	23.5	30.7	52.8	62.5	7000	
$\lvert t\rvert$ [GeV^2]	$(0, 2.5)$				$(0, \lvert t_{\mathrm{sep}}\rvert)$	$(\lvert t_{\mathrm{sep}}\rvert, 2.5)$
χ^2/NDF	124.7/101	95.6/46	96.1/47	76.2/46	109.9/81	120.4/73
CL [%]	5.5	2×10^{-3}	3×10^{-3}	0.3	1.8	4×10^{-2}
R_q [fm]	0.27±0.01	0.28±0.01	0.28±0.01	0.28±0.01	0.45±0.01	0.43±0.01
R_d [fm]	0.72±0.01	0.74±0.01	0.74±0.01	0.75±0.01	0.94±0.01	0.91±0.01
R_{qd} [fm]	0.30±0.01	0.29±0.01	0.31±0.01	0.32±0.01	0.32±0.05	0.37±0.02
α	0.03±0.01	0.02±0.01	0.04±0.01	0.04±0.01	0.11±0.04	0.12±0.01
γ	1.01±0.05	0.98±0.05	0.90±0.06	0.97±0.05	1.00±0.04	1.00 (fixed)

Table 5.1: The values of the fitted ReBB model parameters from ISR to LHC energies. At the $\sqrt{s} = 7$ TeV LHC energy, the pp elastic $\mathrm{d}\sigma/\mathrm{d}t$ data measured by the TOTEM experiment is a composition of two subsequent measurements, which are separated at $t_{\mathrm{sep}} = -0.375$ GeV^2. The errors and the values are rounded up to two valuable decimal digits.

The calculated total cross-section of the low-$|t|$ fit is $\sigma_{\mathrm{tot}} = 99.3 \pm 3.8$ mb, where the uncertainty is the propagated uncertainty of the fit parameters, including that of the shape parameter that can be relatively badly determined in the cone region. This result nevertheless agrees very well with the value $\sigma_{\mathrm{tot}} = 98.0 \pm 2.5$ mb measured by the TOTEM experiment at $\sqrt{s} = 7$ TeV [25] in a luminosity-independent way, and the calculated value

[2]The αBB version of the BB model, discussed in the previous Chapter 4, has been fitted at ISR in the restricted $0.36 < |t| < 2.5$ GeV^2 range in order to be consistent with the t-range of the available TOTEM data set of that time [35], while in this chapter concerning the ReBB model the low $|t|$ data are also included at each analyzed energy. The more limited fit range explains the seemingly better χ^2/NDF and CL values reported in Section 4 and in our earlier publication Ref. [12] using the αBB model.

for the parameter $\rho = 0.09 \pm 0.03$ is also reasonable, as within its errors it is consistent with the measured value of $\rho = 0.145 \pm 0.091$ as reported by the TOTEM experiment [25]. Note, that the uncertainty of the value of our ρ parameter is the propagated uncertainty of the ReBB model fit parameters as it is given in Fig. 5.2, consequently, it contains the effects of propagated statistical and luminosity uncertainties only.

On the other hand, if one checks the fit at the dip region, with $\gamma = 1$ fixed, a remarkable stability of the shape of the differential cross-section can be found at low values of $|t|$ that still yield reasonable values for the total cross-section ($\sigma_{\rm tot} = 91.9 \pm 2.6$ mb) and similarly reasonable values for the parameter $\rho = 0.10 \pm 0.01$. The stability and consistency of the model description is visible also in Figs. 5.2 and 5.3.

For the sake of completeness, I present also one of our fits at the ISR energy of $\sqrt{s} = 23.5$ GeV, as indicated in Fig. 5.4 [1, 6, 68, 69]. The parameters of the best fits and the parameters' errors at each analyzed ISR energy are summarized in Table 5.1.

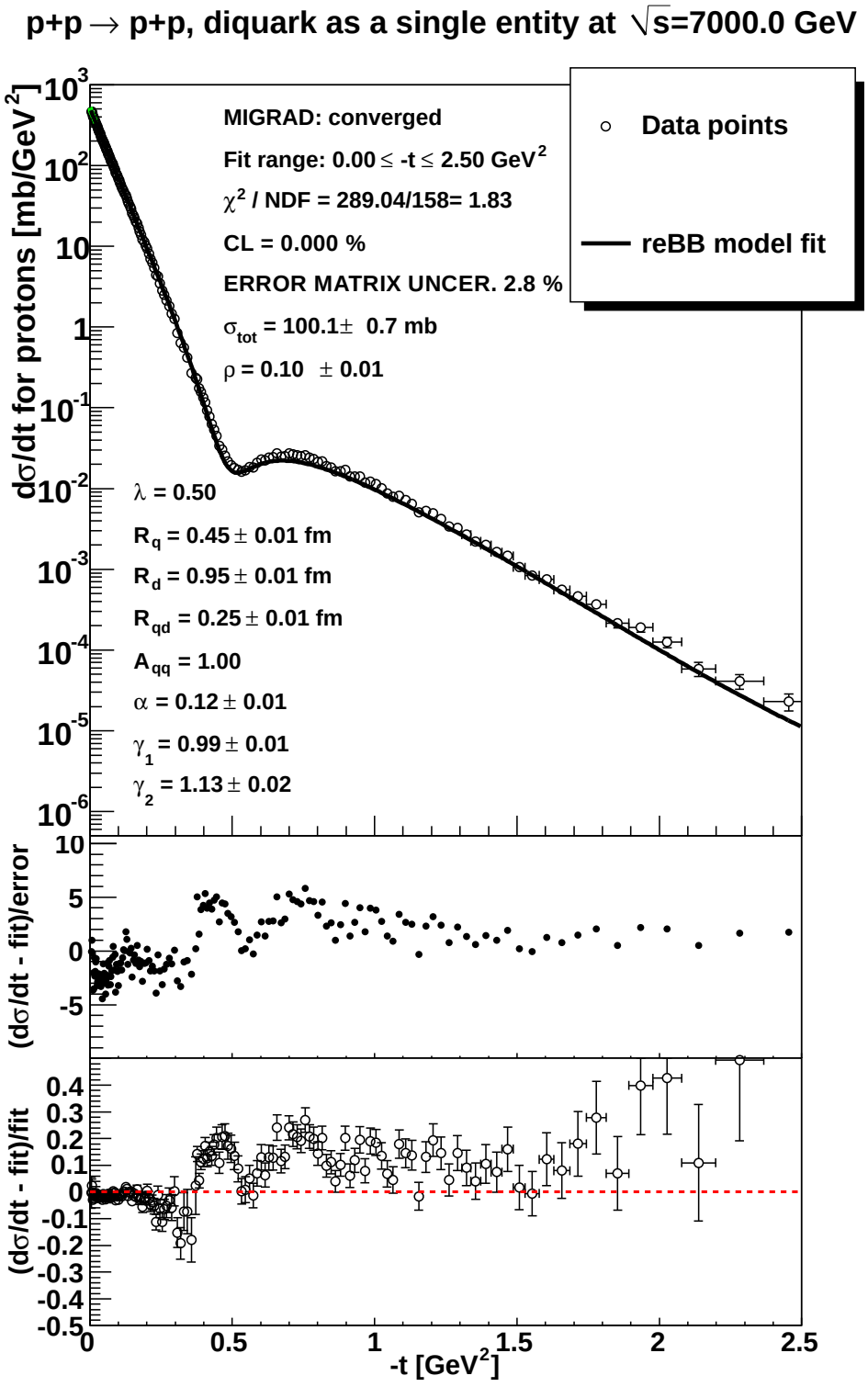

Figure 5.1: The fit of the ReBB model in the whole $0 < |t| < 2.5$ GeV^2 range at $\sqrt{s} = 7$ TeV. The fit method uses the luminosity error according to Eq. (3.32), applying two normalization parameters γ_1 below $|t_{\rm sep}|$ and γ_2 above. Parameters without errors were fixed during the optimization and their value is rounded up to two decimal digits.

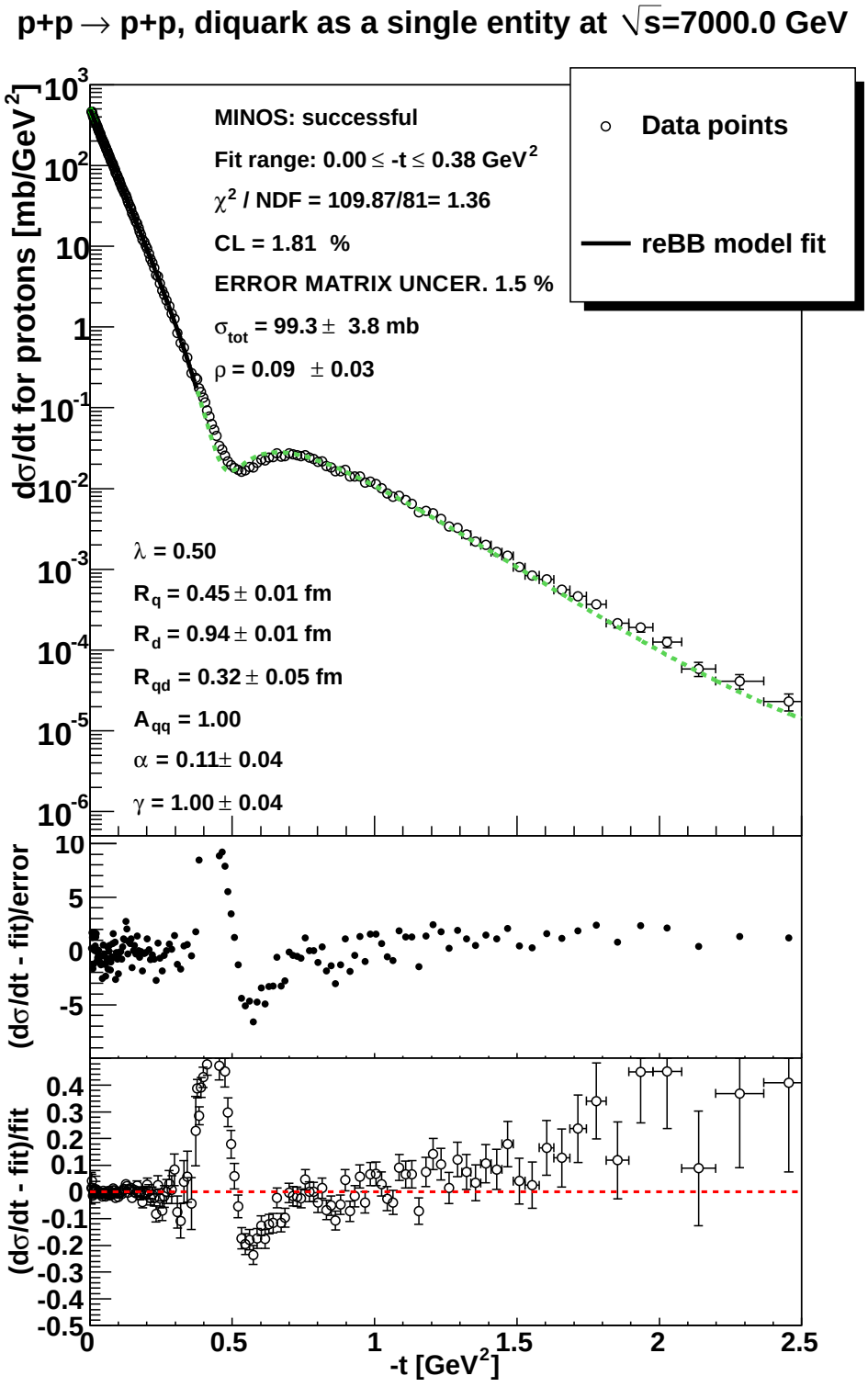

Figure 5.2: The same as Fig. 5.1, but the fit is performed in the $0 < |t| < |t_{\rm sep}|$ range. The fit quality is satisfactory, CL $> 0.1\%$.

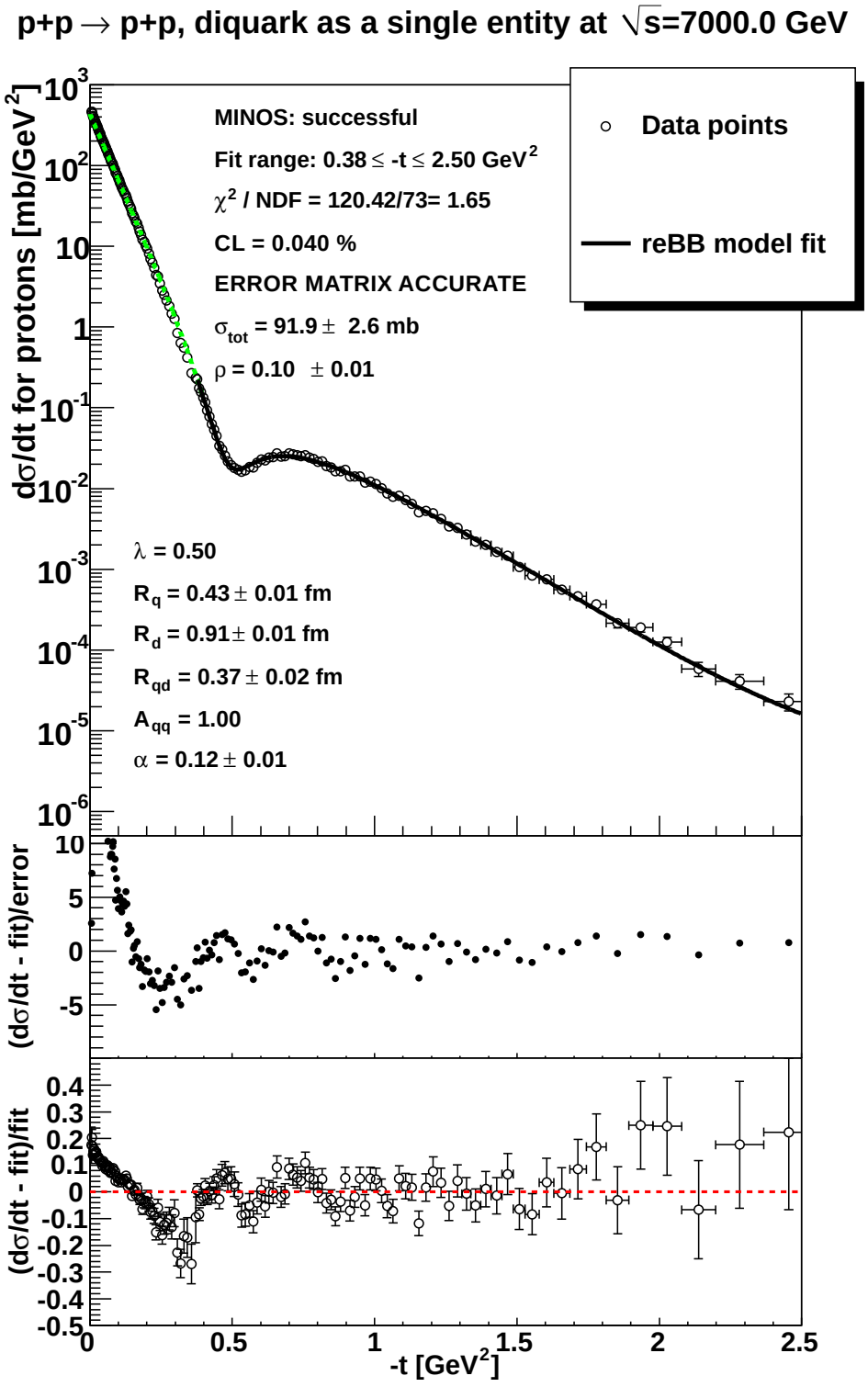

Figure 5.3: The same as Fig. 5.2, but the fit is performed in the $|t_{\rm sep}| < |t| < 2.5$ GeV^2 range. I present the results for the $\gamma = 1$ fixed case.

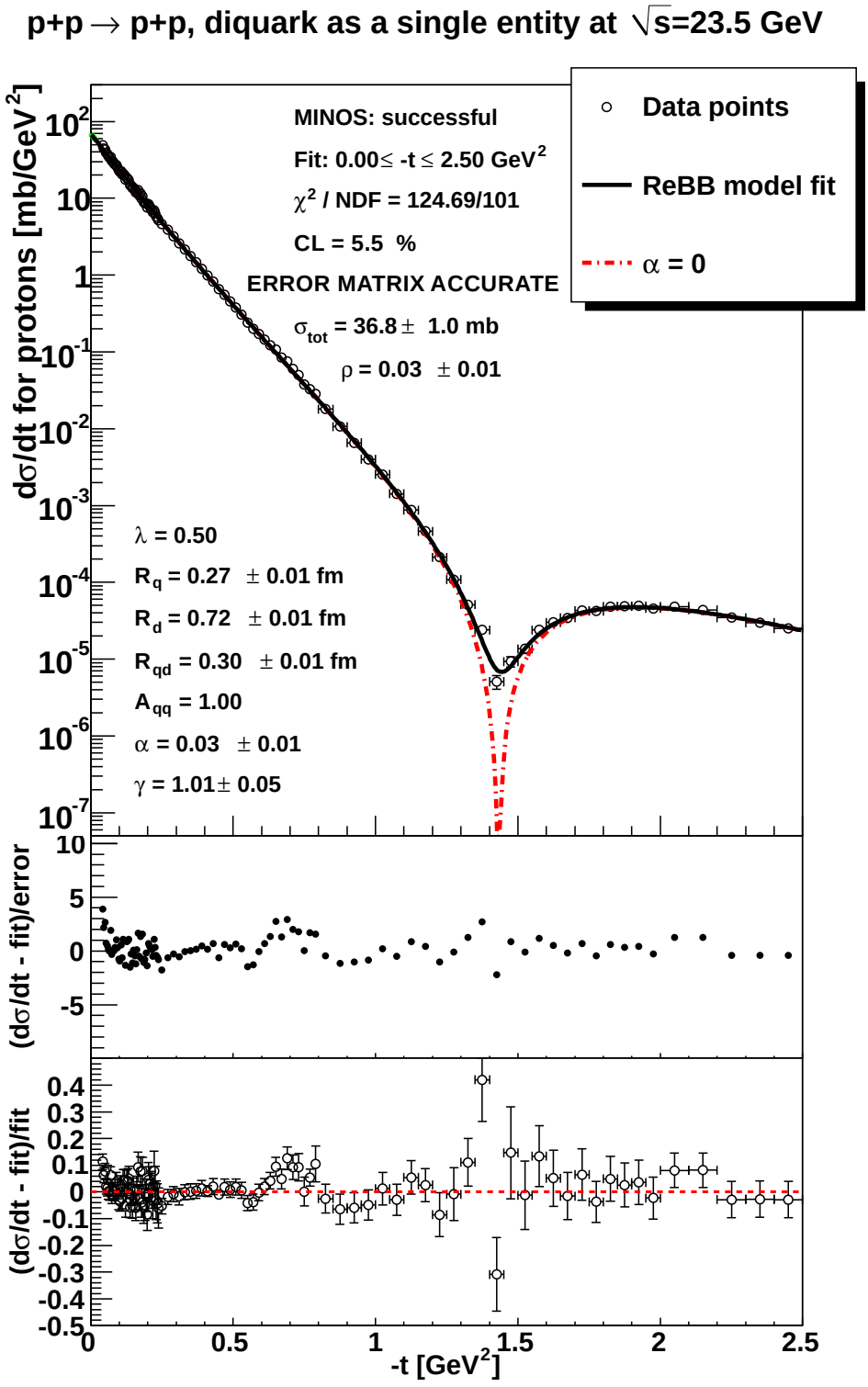

Figure 5.4: The fit of the ReBB model at $\sqrt{s} = 23.5$ GeV in the $0 < |t| < 2.5$ GeV^2 squared four-momentum transfer $|t|$ range. The fit uses the statistical errors of the data points and the luminosity error of the systematic uncertainty according to Eq. (3.32). Parameter values are rounded up to two valuable decimal digits.

If the two parameters A_{qq} and λ are released and included into the set of fitted parameters of the ReBB model, the fit quality improves at each analyzed energy from the point of view of mathematical statistics. In case of $\sqrt{s} = 30.7$ GeV the improvement is quite significant as the confidence level of the fit reaches $CL = 8\,\%$ instead of $2 \times 10^{-3}\,\%$. However, the two new fitted parameters introduce more correlations, which lead to large fit uncertainties, and the parameters λ and A_{qq} within errors remain in the range of their values that were fixed for the fits reported in Table 5.1, however, due to the correlations between the fit parameters when A_{qq} and λ are released, the fit parameters fluctuate more when evaluated as a function of $\sqrt{s}$, consequently their trend is more difficult to determine. Therefore, in order to determine the excitation function of the model parameters, I utilized the results of the ReBB fit results as listed in Table 5.1, where these two parameters are fixed according to Eq. (3.33).

Also note that if $\mathrm{Im}\,\Omega(s,b)$ is defined to be proportional to $\mathrm{Re}\,\Omega(s,b)$, according to Eq. (5.3), the MINUIT fit result of $\chi^2/\mathrm{NDF} = 504.9/159 = 3.2$ is obtained at $\sqrt{s} = 7$ TeV in the $0 < |t| < 2.5$ GeV^2 range, which is disfavored as compared to fits with Eq. (5.1), see also Fig. 5.1.

In Section 3.5 the $p = (q,(q,q))$ version of the BB model, and the ReBB model as well, has been defined, the case when the diquark is assumed to be a composition of two quarks [12]. At $\sqrt{s} = 7$ TeV in the $0 < |t| < 2.5$ GeV^2 range the $p = (q,(q,q))$ scenario provides a fit result with $\chi^2/\mathrm{NDF} = 15509/159 \approx 97.5$, which means that the $p = (q,(q,q))$ ReBB version can be rejected. The failure of the $p = (q,(q,q))$ version is due the wrong shape of the differential cross-section: the second diffractive minimum appears too close to the first one.

5.2 Discussion

5.2.1 Shadow profile functions and saturation

The fits, from which the model parameters were determined, also permit us to evaluate the so-called shadow profile function in order to characterize the absorption in the impact parameter b-space

$$A(s,b) = 1 - \left|\exp\left[-\Omega(s,b)\right]\right|^2 , \tag{5.4}$$

where $\Omega(s,b)$ is the opacity function of Eq. (3.5).

The obtained curves to $A(s,b)$ are shown in Fig. 5.5. The shadow profile functions at ISR energies exhibit a Gaussian like shape, which smoothly change with the center-of-mass energy $\sqrt{s}$. In this case, the $A(s,b=0)<1$ value indicates that the protons are not completely "black" at the ISR energies, even at their centre they do not scatter with the maximum possible probability per unit area. At the LHC energy of $\sqrt{s}=7$ TeV something new appears: the innermost part of the distribution shows a saturation, which means that around $b=0$ the shadow profile function becomes almost flat and stays close to $A(b)\approx 1$. Consequently, the shape of the shadow profile function $A(b)$ becomes non-Gaussian and somewhat "distorted" with respect to the shapes found at ISR. At the same time, the width of the edge of the shadow profile function $A(b)$, which can be visualized as the proton's "skin-width", remains approximately independent of the center-of-mass energy $\sqrt{s}$.

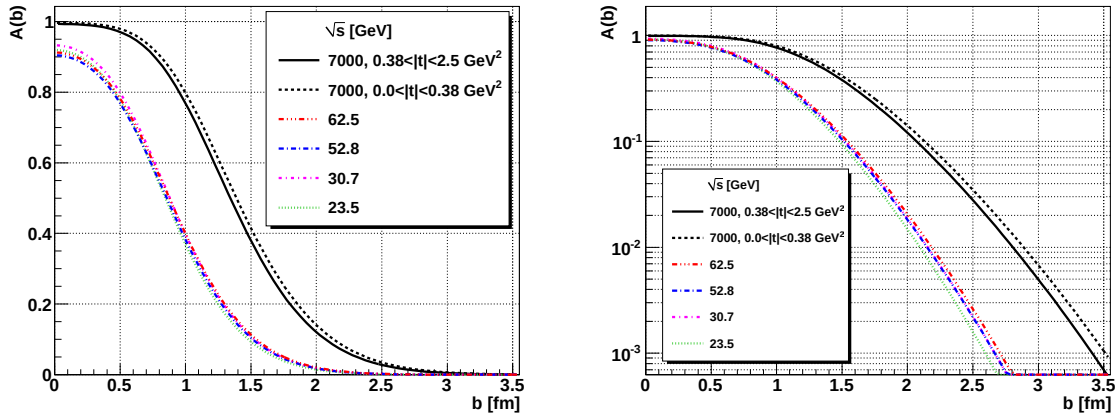

Figure 5.5: The shadow profile functions $A(b)$ of the ReBB fit results indicate a saturation effect at LHC, while at ISR energies a Gaussian shape can be observed. Note that the 7 TeV (black dashed) curve is based on the statistically acceptable fit result in the $0<|t|<0.38$ GeV^2 range. The distributions' edge shows approximately the same width at each energy, corresponding to a constant "skin-width" of the proton.

5.2.2 Non-exponential behavior of $\mathrm{d}\sigma_{\mathrm{el}}/\mathrm{d}t$

To compare the obtained low-$|t|$ ReBB fit of Fig. 5.2 with a *purely* exponential distribution the following exponential parametrization is used

$$\frac{\mathrm{d}\sigma_{\mathrm{el}}}{\mathrm{dt}} = \left.\frac{\mathrm{d}\sigma_{\mathrm{el}}}{\mathrm{dt}}\right|_{t=0} \cdot e^{-B\cdot|t|}\,, \tag{5.5}$$

where $\mathrm{d}\sigma_{\mathrm{el}}/\mathrm{dt}|_{t=0} = 506.4$ mb/GeV^2 and the slope parameter of $B = 19.89$ GeV^{-2} is applied, according to the TOTEM paper of Ref. [68].

The result, shown in Fig. 5.6, indicates a clear non-exponential behavior of the elastic differential cross-section in the $0.0 \leq |t| \leq 0.2$ GeV^2 range at $\sqrt{s}$ =7 TeV.

A very similar structure, a deviation from an exponential behavior was also reported as early as in 1984 in the analysis of proton-antiproton elastic scattering at 546 GeV by Glauber and Velasco [74]. Such a non-exponential behavior at the CERN LHC energy of 8 TeV were made public by the TOTEM experiment [57] interpreted in the theoretical works of Ref. [77, 78].

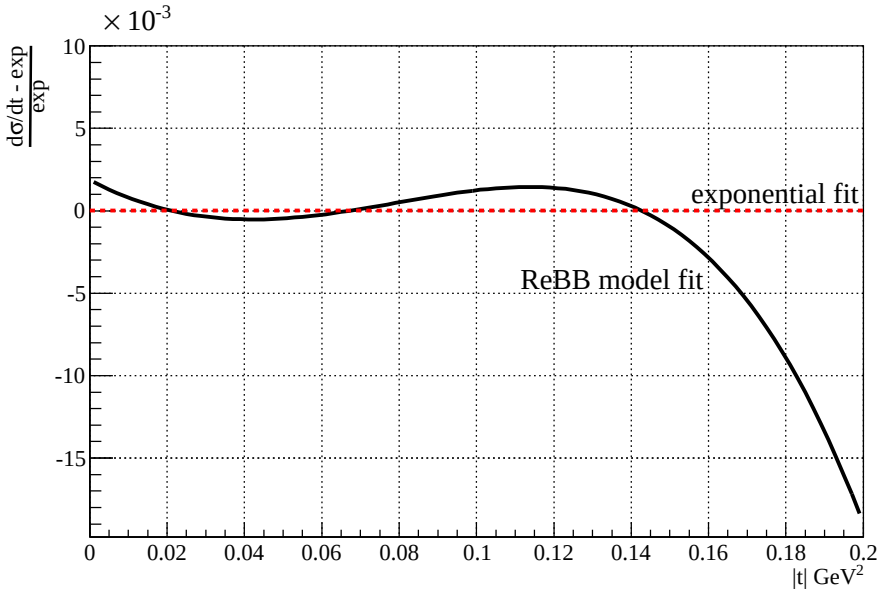

Figure 5.6: The ReBB model fit result, shown in Fig. 5.2, with respect to the exponential fit of Eq. (5.5). In the plot only the $0.0 \leq |t| \leq 0.2$ GeV^2 range is shown, but the ReBB model is fitted to 7 TeV TOTEM data in the low-t interval of $(0, t_{\mathrm{sep}})$. The ReBB fit result indicates a significant deviation from the simple exponential at low-$|t|$ values.

5.3 Extrapolation to future LHC energies and beyond

The ReBB model can be extrapolated to energies which have not been measured yet at LHC. The fit results of Table 5.1 and the parametrization

$$P(s) = p_0 + p_1 \cdot \ln(s/s_0) \tag{5.6}$$

is applied for each parameter $P \in \{R_q, R_d, R_{qd}, \alpha\}$, where $s_0 = 1$ GeV^2. The parametrization Eq. (5.6) implies that the four free parameters of the original ReBB model that were fitted at each colliding energy independently are now replaced with eight parameters p_i that prescribe their energy dependence. The fits of the ReBB model parameters are shown in Fig. 5.7 and the fit parameters are collected in Table 5.2.

The logarithmic dependence of the geometric parameters on the center-of-mass energy $\sqrt{s}$ in the parametrization Eq. (5.6) is motivated by the so-called "geometric picture" based on a series of studies [18–20, 79–81]. In case of the α parameter, which is not a geometrical property of the proton, the logarithmic $\sqrt{s}$ dependence is an additional assumption. As indicated by Fig. 5.7 and Table 5.2, such an energy dependence of the α shape parameter is consistent with the currently available data.

Table 5.2 shows that the rate of increase with $\sqrt{s}$, parameter p_1, is an order of magnitude larger for R_q and R_d than for R_{qd}. The saturation effect, described in Section 5.2.1, is consistent with this observation as the increasing components of the proton, the quark and the diquark, are confined into a volume which is increasing slower than that.

Parameter	R_q [fm]	R_d [fm]	R_{qd} [fm]	α
χ^2/NDF	6.2/3	2.4/3	7.5/3	1.2/3
CL [%]	10.2	49.4	5.8	75.3
p_0	0.15 ± 0.01	0.59 ± 0.01	0.30 ± 0.01	-0.04 ± 0.01
p_1	0.017 ± 0.001	0.019 ± 0.001	0.002 ± 0.001	0.009 ± 0.001

Table 5.2: The parametrization Eq. (5.6) is applied to each parameter of the ReBB model and the fits are shown in Fig. 5.7. Numerical values are rounded up to two valuable decimal digits. The fit quality information is provided in the first and second row of the table. Note that the fit quality is acceptable for each parameter as CL>0.1 % for each fit.

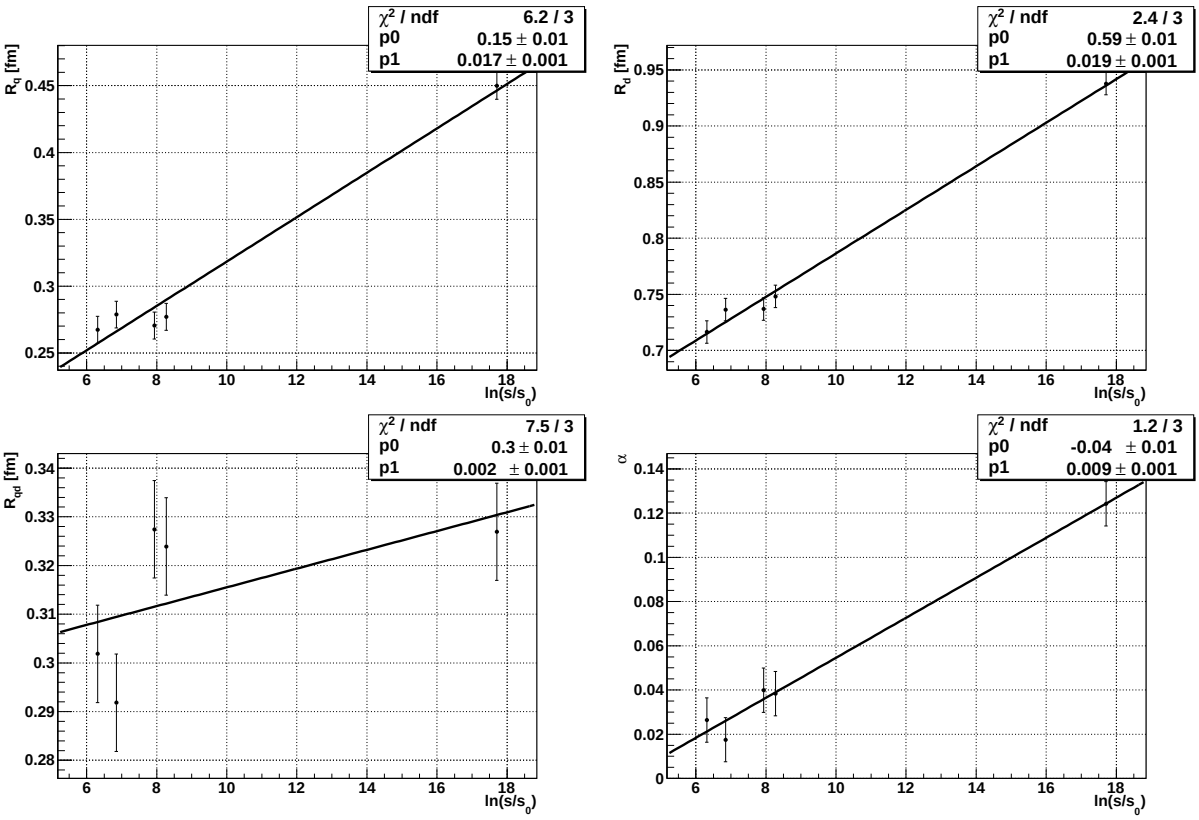

Figure 5.7: The excitation function of the parameters of the ReBB model, collected in Table 5.1, is determined from fits with Eq. (5.6) to each of the parameters R_q, R_d, R_{qd} and α. The plots about the resulting fits are collected here, while the parameters of the excitation functions are collected in Table 5.2. The statistically acceptable quality of these fits allow the ReBB model to be extrapolated to center-of-mass energies which have not been measured yet at LHC.

Using the extrapolation formula Eq. (5.6) and the value of the parameters from Table 5.2 it is straightforward to calculate the values of the parameters at 8 TeV, where the TOTEM measurement of the total cross-section is published [26], and at expected future LHC energies of $\sqrt{s}$ =13, 14, 15 TeV and also at 28 TeV, which is beyond the LHC capabilities. Using the extrapolated values of the parameters I plot the predicted pp elastic differential cross-section curves at each mentioned energy in Fig. 5.8. The shadow profile functions $A(b)$ can be also extrapolated, see Fig. 5.9. The shadow profile functions even allow us to visualize the increasing effective interaction radius of the proton in the impact parameter space in Fig. 5.10.

It is also important to see how the most important features change with center-of-mass

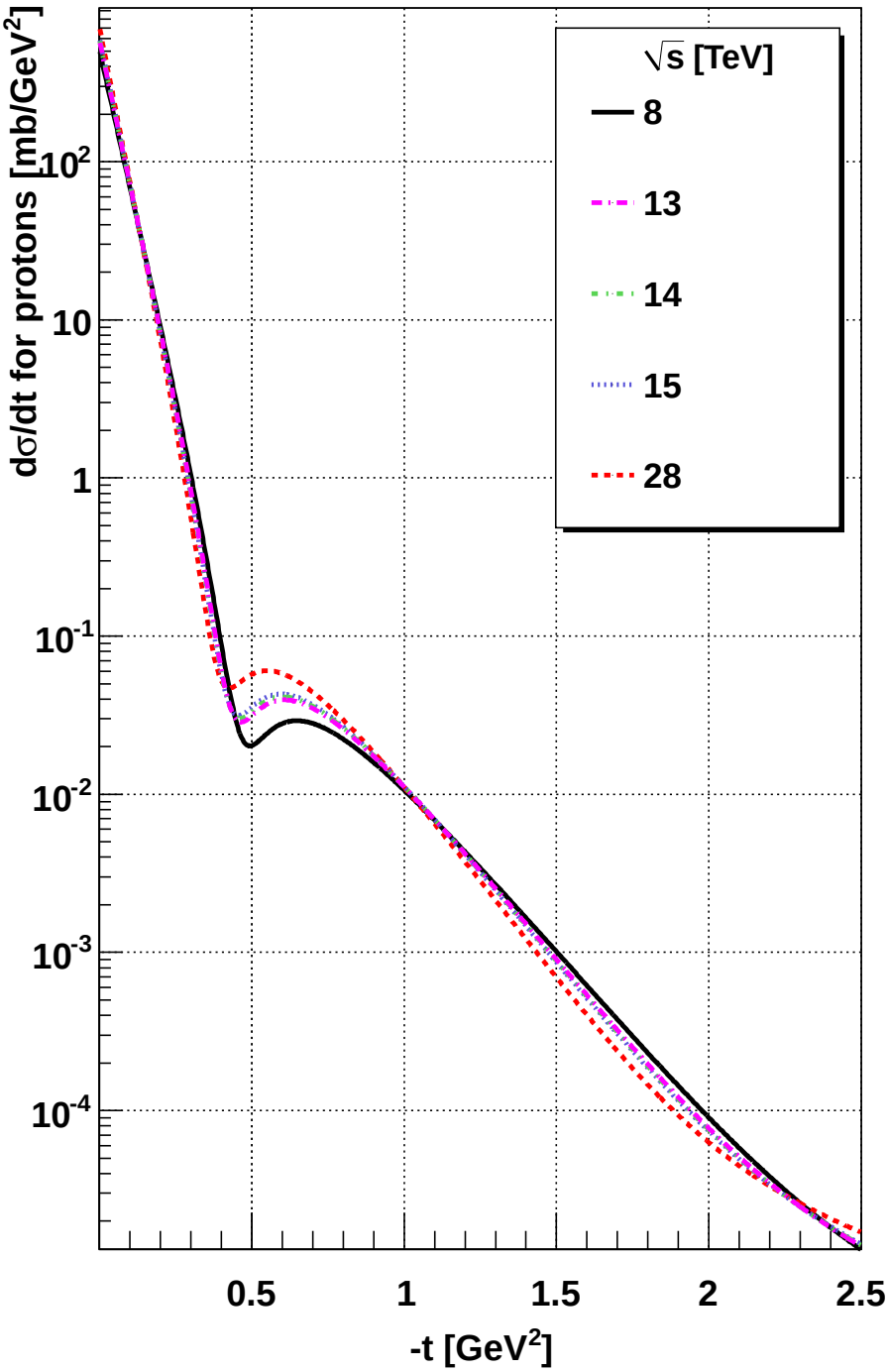

Figure 5.8: The *pp* elastic differential cross-section is extrapolated to 8 TeV as well as to future LHC energies and beyond.

energy $\sqrt{s}$: the extrapolated values of the total cross-section $\sigma_{\rm tot}$, the position of the first diffractive minimum $|t_{\rm dip}|$ and the parameter ρ is given in Table 5.3.

Our calculated value at $\sqrt{s} = 8$ TeV is $\sigma_{\rm tot} = 99.6$ mb, which is consistent with the total cross-section $\sigma_{\rm tot} = 101.7 \pm 2.9$ mb at $\sqrt{s} = 8$ TeV, measured with a luminosity-independent method by the TOTEM experiment [26].

According to Table 5.3, the predicted value of $|t_{\rm dip}|$ and $\sigma_{\rm tot}$ moves more than 10 % when $\sqrt{s}$ increases from 8 TeV to 28 TeV, while the value of $C = |t_{\rm dip}| \cdot \sigma_{\rm tot}$ changes only about 2 %, which is an approximately constant value, within the errors of the extrapolation.

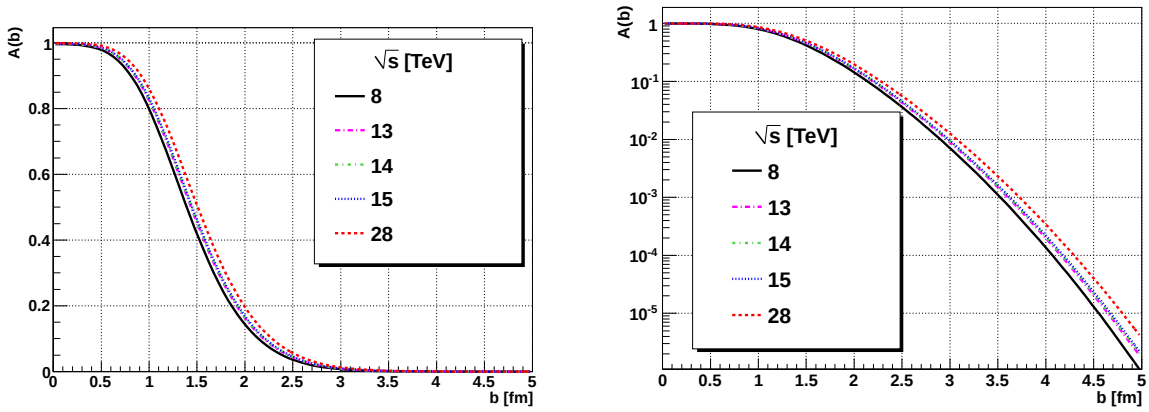

Figure 5.9: The shadow profile functions at the extrapolated energies $\sqrt{s}$. The results show the increase of the proton interaction radius with increasing $\sqrt{s}$ energies. Also note that the "edge" of the distributions remains of approximately constant width and shape.

I have reported a similar, and exact, scaling of the black disk scattering model with Eq. (4.6) [76]. However, the scaling behavior indicated by the stability of the value C, is different from the black disk model, described by Eq. (4.6), as the corresponding value $C_{\rm black}$ is significantly different

$$C_{\rm black} \neq C\,. \tag{5.7}$$

In this sense the value of C indicates a more complex scattering phenomena, than the scattering of a photon on a black disc, however, the constancy of the product suggests the validity of an asymptotic geometric picture, in agreement with the recent observations in Refs. [12, 82–84].

$\sqrt{s}$ [TeV]	$\sigma_{\rm tot}$ [mb]	$\lvert t_{\rm dip}\rvert$[GeV^2]	ρ	$C_{\rm extr} = \lvert t_{\rm dip}\rvert \cdot \sigma_{\rm tot}$ [mb GeV^2]
8	99.6	0.494	0.103	49.20
13	106.4	0.465	0.108	49.48
14	107.5	0.461	0.108	49.56
15	108.5	0.457	0.109	49.58
28	117.7	0.426	0.114	50.14

Table 5.3: The extrapolated values of the total cross-section $\sigma_{\rm tot}$ at future LHC energies and beyond. The position of the first diffractive minimum $|t_{\rm dip}|$, the parameter ρ and the $|t_{\rm dip}| \cdot \sigma_{\rm tot}$ value is also provided at each energy. Note, that the predicted value of $|t_{\rm dip}|$ and $\sigma_{\rm tot}$ moves more than 10% when $\sqrt{s}$ increases from 8 TeV to 28 TeV, while the value of $C_{\rm extr}$ increases with about 2 %. Note also, that the C value of Eq. (4.3) is higher than any of the quoted $C_{\rm extr}$ values of the table; the reason is that the ReBB model predicts a shallow minimum for $C_{\rm extr}$ at $\sqrt{s} = 200$ GeV.

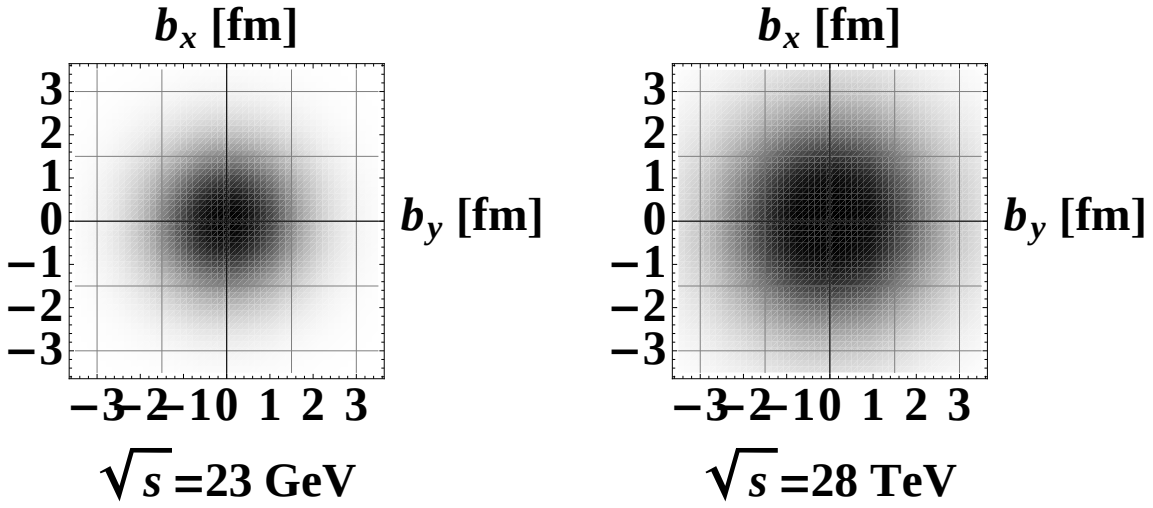

Figure 5.10: Visualization of the shadow profile functions $A(b)$ in the transverse plane of the impact parameter vector (b_x, b_y). The figures show the increase of the proton effective interaction radius in the impact parameter space with increasing center-of-mass energy $\sqrt{s}$. It can be also observed that the black innermost core of the distributions is increasing, while the thickness of the proton's "skin", the gray transition part of the distributions, remains approximately independent of the center-of-mass energy $\sqrt{s}$.

5.4 Summary of Chapter 5

To overcome the clear disagreement between data and model description at LHC energy of $\sqrt{s} = 7$ TeV, I have further generalized the BB model using unitarity constraints [13]. I have fitted the new model (ReBB model) at ISR and also at LHC energy of $\sqrt{s} = 7$ TeV. I have determined the energy dependence of the ReBB model parameters based on the good quality of the fits at ISR and LHC energies and I have extrapolated the ReBB model to future LHC energies and beyond. I have shown that the effective interaction radius of the proton, calculated from the ReBB model, is increasing substantially between ISR and LHC energies, while the proton's effective "edge" shows the same width. I have demonstrated that the ReBB model shows a non-exponential feature at low values of the squared four-momentum transfer $|t|$, which is consistent with the TOTEM data at $\sqrt{s} = 8$ TeV.

Chapter 6

Conclusions and Summary

For the TOTEM experiment I have calibrated the LHC beam optics at IP5 by exploiting the proton-proton data measured by the TOTEM RP detectors [8, 9]. The new calibration method reduced the largest systematic error of the total proton-proton cross-section measurement with approximately an order of magnitude, see Fig. 2.10. With this optics calibration result, I made it possible to measure the total proton-proton cross-section $\sigma_{\rm tot}$ with very good accuracy at CERN LHC $\sqrt{s} = 7$ and 8 TeV energies

I have checked and confirmed the published results of the Bialas-Bzdak model, and I have determined the best value and uncertainty of the model parameters at ISR and LHC energies. I have successfully fitted both the $p = (q, d)$ and $p = (q, (q, q))$ model versions to the ISR data, and I have demonstrated, that the original Bialas-Bzdak model is not able to describe the data, measured at the LHC [11]. I have defined an effective proton radius $R_{\rm eff}$, which takes the same value for both model versions, and I have shown that $R^2_{\rm eff}$ is proportional to the total proton-proton cross-section $\sigma_{\rm tot}$ at ISR energies [11].

I have generalized the Bialas-Bzdak model by adding a perturbatively small real part to its elastic scattering amplitude. I have fitted the improved model, αBB model, to data measured at ISR and LHC energies [12]. I have achieved, that the αBB model can be fitted to the ISR data without adjusting the fit range. On the other hand I have found that even the αBB model is not able to interpret the data measured at LHC energy of $\sqrt{s} = 7$ TeV. I have diagnosed that the interpretation of the LHC data requires an increased real part in the elastic scattering amplitude, which is too large to be treated perturbatively.

I have discovered, that the product of the total proton-proton cross-section σ_{tot} and the squared four-momentum transfer position of the dip t_{dip} leads to a value which is approximately independent from the collision energy. I have also found that the so-called "black disk" model shows a similar and exact behavior, however, the exact value differs from the measured one. With this observation I have shown that the "black disk" limit is not reached at the LHC energy of $\sqrt{s} = 7$ TeV.

Using unitarity constraints I have generalized the BB model by adding an arbitrarily large real part to its scattering amplitude in a systematic way. I have shown that the improved model, ReBB model, is able to describe the data measured at ISR and LHC energies in a statistically acceptable manner [13].

Based on the good quality of the ReBB fit results, I found a statistically acceptable description of the energy dependence of the ReBB model parameters, with which I was able to estimate the expected value of the total proton-proton cross-section at future LHC energies and beyond [13].

I have shown as well, that the effective interaction radius of the proton is substantially increasing with increasing colliding energy between ISR and LHC. I have also found that the probability of having inelastic collision within this effective radius is also increasing, and becomes almost certain at LHC. At the same time the "edge" of the probability distribution remains approximately constant.

I have discovered that for low values of the squared four-momentum transfer $|t|$ the ReBB model predicts a non-exponential behavior in the elastic proton-proton differential cross-section, which observation is in agreement with a TOTEM result currently under the review process [13, 57].

I would like to continue my research as a member of the TOTEM collaboration with the experimental analysis and theoretical interpretation of the proton-proton scattering data, which is expected to be measured soon at the LHC energy of $\sqrt{s} = 13$ and 14 TeV

Chapter 7

Acknowledgments

I am grateful to my PhD supervisor Prof. Tamás Csörgő and to my Co-Supervisor Dr. Máté Csanád for their knowledgeable support along my PhD research and also to Dr. János Sziklai who helped me in the TOTEM experiment. I would like to thank my CERN supervisor Dr. Hubert Niewiadomski for the many illuminating and widespread discussions over the years and the leader of my PhD school Prof. László Palla for his support.

I would like to express my gratitude to the TOTEM Collaboration at CERN for their support and also to my institutes in Hungary: the Eötvös University and the WIGNER Research Centre for Physics at Budapest.

I would like to stress my gratitude to Prof. Karsten Eggert and Prof. Simone Giani, the former and present Spokespersons and Analysis Coordinators of the TOTEM Collaboration for their trust and support and also to Dr. Joachim Baechler, the CERN Group Leadear and Technical Coordinator of the TOTEM experiment, to his help. I am also very grateful to Valentina Avati, Dr. Mario Deile, Prof. Marco Bozzo, Prof. Nicola Turini, Prof. Giuseppe Latino and to Dr. Kenneth Oesterberg the Physics Coordinator of the TOTEM experiment for the discussions and their helpful advices.

I learnt countless analysis techniques from Dr. Jan Kašpar, thank you! My colleagues Dr. Mirko Berretti, Dr. Fabrizio Ferro, Jiři Procházka, Dr. Leszek Grzanka, Dr. Jošef Kopal, Dr. Michele Quinto, Adrian Fiergolski, Edoardo Bossini, Nicola Minafra and Liliana Losurdo helped me a lot during my work, thank you!

Let me also to thank Prof. Angelo Scribano the Collaboration Board Chairperson of

the TOTEM experiment, Prof. Ernst Radermacher, Dr. Francesco Cafagna, Emilio Radicioni, Gabriella Catanesi the TOTEM Editorial Board Chairperson, Beatrice Bressan the TOTEM Outreach Coordinator, Gueorgui Antchev, Ivan Atanassov and Prof. Vincenzo Berardi for the common work. The TOTEM secretariats Adele Saredo Parodi and Tania Martucci managed me very efficiently, thank you!

Let me thank Prof. Vojtěch Kundrát, Prof. László Jenkovszky and Prof. Gosta Gustafson for their important theoretical guidance and Dr. Matteo Giordano and Prof. Takeshi Kodama for the inspiring discussions.

I am grateful to my Parents. I would like to thank the two Ildikó-s, my aunt and my cousin for their encouragement. And last, but not least, I am grateful to Pavla Kašparová for the svíčková and for the discussions.

Appendix A

Basic formulae

The basic formulae are collected here, to define the notation. The kinematics for two-body reactions [2]

$$1 + 2 \to 3 + 4\,, \tag{A.1}$$

can be described with the *Mandelstam invariants*

$$\begin{aligned} s &= (p_1 + p_2)^2 = (p_3 + p_4)^2\,, \\ t &= (p_1 - p_3)^2 = (p_2 - p_4)^2\,, \\ u &= (p_1 - p_4)^2 = (p_2 - p_3)^2\,. \end{aligned} \tag{A.2}$$

Process Eq. (A.1) is a so-called s-channel process by means of the Mandelstam variable s, which is the square of the total center-of-mass energy.

The Mandelstam variables obey the identity

$$s + t + u = \sum_{i=1}^{4} m_i^2\,, \tag{A.3}$$

which is a consequence of the conservation of the four-momentum and the definitions Eq. (A.2). Hence, only two of them are independent. I use the variables s and t throughout this PhD thesis.

In case of the s-channel reaction (A.1), the definition of the center-of-mass (CM) system is

$$\vec{p}_1 + \vec{p}_2 = 0\,. \tag{A.4}$$

Assume that particle 1 and 2 travel along the z-axis. In this case the four-momenta

of the incoming and outgoing particles can be given as

$$\begin{aligned} p_1 &= (E_1, \quad \vec{p}) = (E_1, 0, 0, \quad p_z)\,, \\ p_2 &= (E_2, -\vec{p}) = (E_2, 0, 0, -p_z)\,, \\ p_3 &= (E_3, \quad \vec{p}') = (E_3, \quad \vec{\Delta}, \quad p'_z)\,, \\ p_4 &= (E_4, -\vec{p}') = (E_4, -\vec{\Delta}, -p'_z)\,, \end{aligned} \tag{A.5}$$

where the conservation of the three-momentum and definition (A.4) was used. The scattering angle ϑ, in the s-channel, is defined by

$$p'_z = |\vec{p}'|\cos\vartheta\,, \quad |\vec{\Delta}| = |\vec{p}'|\sin\vartheta\,. \tag{A.6}$$

The energies E_i can be expressed in terms of the CM variables

$$E_1 = \frac{1}{2\sqrt{s}}(s + m_1^2 - m_2^2)\,, \quad E_2 = \frac{1}{2\sqrt{s}}(s + m_2^2 - m_1^2)\,, \tag{A.7}$$

and E_3, E_4 can be obtained from Eq. (A.7) by replacing the indices $1 \to 3$ and $2 \to 4$ respectively. The particle momenta can be also expressed with CM variables

$$\begin{aligned} |\vec{p}|^2 &= p_z^2 = E_1^2 - m_1^2 = \frac{1}{4s}\lambda(s, m_1^2, m_2^2)\,, \\ |\vec{p}'|^2 &= |\vec{\Delta}|^2 + p_z^2 = E_3^2 - m_3^2 = \frac{1}{4s}\lambda(s, m_3^2, m_4^2)\,, \end{aligned} \tag{A.8}$$

where λ is the *triangle function*

$$\lambda(x, y, z) = x^2 + y^2 + z^2 - 2xy - 2yz - 2xz\,. \tag{A.9}$$

If the particle masses are identical $m_i = m$ or in the *high energy limit*

$$s \to \infty\,, \tag{A.10}$$

according to Eq. (A.7) and Eq. (A.8), each particle energy and momentum approaches the same limit

$$E_i \simeq \frac{\sqrt{s}}{2}\,, \quad |\vec{p}|, |\vec{p}'| \simeq \frac{\sqrt{s}}{2}\,. \tag{A.11}$$

The squared four-momentum transfer can be expressed with the center-of-mass variables using Eq. (A.5)

$$t = (p_1 - p_3)^2 = m_1^2 + m_3^2 - 2E_1E_3 + 2|\vec{p}||\vec{p}'|\cos\vartheta\,. \tag{A.12}$$

If the particles have equal masses

$$t = -2|\vec{p}|^2(1 - \cos\vartheta)\,, \tag{A.13}$$

and

$$\cos\vartheta = 1 + \frac{2t}{s - 4m^2}\,. \tag{A.14}$$

In the high energy limit, or in the massless case, Eq. (A.14) simplifies to

$$\cos\vartheta = 1 + \frac{2t}{s}\,. \tag{A.15}$$

This expression (A.15) and the definition of the scattering angle Eq. (A.6) lead to

$$t \simeq -\Delta^2\,, \tag{A.16}$$

where $\Delta = |\vec{\Delta}|$, which is also useful in the form

$$\Delta \simeq \sqrt{-t}\,. \tag{A.17}$$

Bibliography

[1] U. Amaldi and K. R. Schubert *Nucl.Phys.* **B166** (1980) 301.

[2] V. Barone and E. Predazzi, *High-Energy Particle Diffraction.* Springer-Verlag, Berlin Heidelberg New York, 1 ed., 2002.

[3] K. Gottfried and V. Weisskopf, *Concepts of particle physics*, vol. 2. Oxford University Press, Oxford, 1986.

[4] L. Landau and I. Pomeranchuk *Zh. Eksp. Teor. Fiz.* **24** (1953) 505.

[5] G. Anelli *et al. JINST* **3** (2008) S08007.

[6] G. Antchev, P. Aspell, I. Atanassov, V. Avati, J. Baechler, *et al. Europhys.Lett.* **96** (2011) 21002, arXiv:1110.1395 [hep-ex].

[7] B. Abelev *et al. Eur.Phys.J.* **C73** no. 6, (2013) 2456, arXiv:1208.4968 [hep-ex].

[8] G. Antchev *et al. New J.Phys.* **16** (2014) 103041, arXiv:1406.0546 [physics.acc-ph].

[9] F. Nemes and H. Niewiadomski. https://cds.cern.ch/record/2016034. CERN-TOTEM-NOTE-2015-001.

[10] A. Bialas and A. Bzdak *Acta Phys.Polon.* **B38** (2007) 159–168, arXiv:hep-ph/0612038 [hep-ph].

[11] F. Nemes and T. Csörgő *Int.J.Mod.Phys.* **A27** (2012) 1250175, arXiv:1204.5617 [hep-ph].

[12] T. Csörgő and F. Nemes *Int.J.Mod.Phys.* **A29** (2014) 1450019, arXiv:1306.4217 [hep-ph].

[13] F. Nemes, T. Csörgő, and M. Csanád *Int.J.Mod.Phys.* **A30** (2015) 1550076, arXiv:1505.01415 [hep-ph].

[14] O. S. Bruning, P. Collier, P. Lebrun, S. Myers, R. Ostojic, *et al.*, *LHC Design Report: The LHC Main Ring*, vol. 1. 2004.

[15] G. Aad *et al. JHEP* **1504** (2015) 117, arXiv:1501.04943 [hep-ex].

[16] S. Chatrchyan *et al. Nature Phys.* **10** (2014) 557–560, arXiv:1401.6527 [hep-ex].

[17] A. Team, "The four main LHC experiments," tech. rep., Jun, 1999. http://cds.cern.ch/record/40525.

[18] H. Cheng and T. T. Wu *Phys.Rev.* **182** (1969) 1852–1867.

[19] H. Cheng and T. Wu, *Expaning protons: scattering at high-energies*. MIT Press, Cambridge, USA, 1987.

[20] H. Cheng and T. T. Wu *Phys.Rev.* **182** (1969) 1868–1872.

[21] E. A. Kuraev, L. N. Lipatov, and V. S. Fadin *Sov.Phys.JETP* **44** (1976) 443–450.

[22] L. Lipatov *Adv.Ser.Direct.High Energy Phys.* **5** (1989) 411–489.

[23] E. Avsar, G. Gustafson, and L. Lonnblad *JHEP* **0507** (2005) 062, arXiv:hep-ph/0503181 [hep-ph].

[24] J. Cudell *et al. Phys.Rev.Lett.* **89** (2002) 201801, arXiv:hep-ph/0206172 [hep-ph].

[25] G. Antchev *et al. Europhys.Lett.* **101** (2013) 21004.

[26] G. Antchev *et al. Phys.Rev.Lett.* **111** no. 1, (2013) 012001.

[27] S. Chatrchyan *et al. Eur.Phys.J.* **C74** no. 10, (2014) 3053, arXiv:1405.0722 [hep-ex].

[28] G. Antchev *et al. Europhys.Lett.* **98** (2012) 31002, arXiv:1205.4105 [hep-ex].

[29] G. Antchev *et al. Eur.Phys.J.* **C75** no. 3, (2015) 126, arXiv:1411.4963 [hep-ex].

[30] G. Antchev *et al. Phys.Rev.Lett.* **111** no. 26, (2013) 262001, arXiv:1308.6722 [hep-ex].

[31] C. CMS and C. TOTEM. http://cds.cern.ch/record/1954840.

[32] "TOTEM Upgrade Proposal," Tech. Rep. CERN-LHCC-2013-009. LHCC-P-007, CERN, Geneva, Jun, 2013. http://cds.cern.ch/record/1554299.

[33] "Timing Measurements in the Vertical Roman Pots of the TOTEM Experiment," Tech. Rep. CERN-LHCC-2014-020. TOTEM-TDR-002, CERN, Geneva, Sep, 2014. https://cds.cern.ch/record/1753189.

[34] M. Albrow, M. Arneodo, V. Avati, J. Baechler, N. Cartiglia, M. Deile, M. Gallinaro, J. Hollar, M. Lo Vetere, K. Oesterberg, N. Turini, J. Varela, D. Wright, and C. CMS-TOTEM, "CMS-TOTEM Precision Proton Spectrometer," Tech. Rep. CERN-LHCC-2014-021. TOTEM-TDR-003. CMS-TDR-13, CERN, Geneva, Sep, 2014. https://cds.cern.ch/record/1753795.

[35] G. Antchev *et al. Europhys.Lett.* **95** (2011) 41001, arXiv:1110.1385 [hep-ex].

[36] U. Amaldi, R. Biancastelli, C. Bosio, G. Matthiae, J. Allaby, *et al. Phys.Lett.* **B44** (1973) 112–118.

[37] J. Kašpar, V. Kundrat, and M. Deile, *Elastic scattering at the LHC*. PhD thesis, Charles U., 2011. https://cds.cern.ch/record/1441140. Presented 10 Apr 2012.

[38] G. Bencze, A. Chikanian, M. Della Negra, V. Grachev, A. Herve, *et al. Nucl.Instrum.Meth.* **A357** (1995) 40–54.

[39] R. Tomas, O. Bruning, M. Giovannozzi, M. Lamont, F. Schmidt, *et al. Conf.Proc.* **C100523** (2010) TUXMH02.

[40] M. Alabau Pons, F. Schmidt, R. Tomas, and E. Maclean *Conf.Proc.* **C110904** (2011) 2202–2204.

[41] E. Wilson, *An introduction to particle accelerators*. Oxford University Press, Oxford, 2001.

[42] H. Wiedemann, *Particle accelerator physics: Basic principles and linear beam dynamics*. 1993.

[43] F. Willeke and G. Ripken *AIP Conf.Proc.* **184** (1989) 758–819.

[44] K. Olive *et al. Chin.Phys.* **C38** (2014) 090001.

[45] H. Niewiadomski, V. Avati, C. Da Via, and K. Eggert, *Reconstruction of Protons in the TOTEM Roman Pot Detectors at the LHC*. PhD thesis, Manchester U., Manchester, 2008. `http://cds.cern.ch/record/1131825`. Presented on 11 Sep 2008.

[46] H. Grote and F. Schmidt *Conf.Proc.* **C030512** (2003) 3497.

[47] R. Billen and C. Roderick, "The LHC Logging Service: Capturing, storing and using time-series data for the world's largest scientific instrument," Tech. Rep. AB-Note-2006-046. CERN-AB-Note-2006-046, CERN, Nov, 2006.

[48] C. Roderick and R. Billen, "The LSA Database to Drive the Accelerator Settings," Tech. Rep. CERN-ATS-2009-100, CERN, Geneva, Nov, 2009.

[49] N. Aquilina, M. Giovannozzi, P. Hagen, M. Lamont, A. S. Langner, E. Todesco, R. Tomas, J. Wenninger, and N. Sammut.

[50] P. Hagen, M. Giovannozzi, J. Koutchouk, T. Risselada, F. Schmidt, *et al.* *Conf.Proc.* **C0806233** (2008) TUPP091.

[51] L. Evans and P. Bryant *JINST* **3** (2008) S08001.

[52] A. Yamamoto, T. Ogitsu, N. Ohuchi, and T. Nakamoto, "Inner Triplet Quadrupole MQXA," Tech. Rep. LHC-MQXA-ES-0001, EDMS doc. 313715, CERN, Geneva, Nov, 2001. `https://edms.cern.ch/file/313715/1.0/lhc-mqxa-es-0001-10-00.pdf`. LHC Functional Specification.

[53] J. Kerby and M. Lamm, "Inner Triplet Quadrupole MQXB," Tech. Rep. LHC-LQX-ES-0002, EDMS doc. 256806, CERN, Geneva, Apr, 2001.

https://edms.cern.ch/file/256806/1.1/lhc-lqx-es-0002-10-11.pdf. LHC Functional Specification.

[54] J. Wenninger, "Energy Calibration of the LHC Beams at 4 TeV," Tech. Rep. CERN-ATS-2013-040, CERN, Geneva, May, 2013. https://cds.cern.ch/record/1546734.

[55] J. Wenninger, "Beam momentum calibration at the LHC," tech. rep., 2004.

[56] **TOTEM** Collaboration, V. Berardi *et al.*, "TOTEM: Technical design report. Total cross section, elastic scattering and diffraction dissociation at the Large Hadron Collider at CERN," tech. rep., 2004.

[57] G. Antchev *et al.* arXiv:1503.08111 [hep-ex].

[58] A. Donnachie and P. Landshoff arXiv:1112.2485 [hep-ph].

[59] R. J. Glauber, *Lectures in Theoretical Physics*. Interscience, New York, 1 ed., 1959.

[60] F. James and M. Roos *Comput.Phys.Commun.* **10** (1975) 343–367.

[61] A. Martin, H. Hoeth, V. Khoze, F. Krauss, M. Ryskin, *et al. PoS* **QNP2012** (2012) 017, arXiv:1206.2124 [hep-ph].

[62] E. Levin arXiv:hep-ph/9808486 [hep-ph].

[63] V. Khoze, A. Martin, and M. Ryskin arXiv:1402.2778 [hep-ph].

[64] M. Ryskin, A. Martin, and V. Khoze *Eur.Phys.J.* **C72** (2012) 1937, arXiv:1201.6298 [hep-ph].

[65] M. Ryskin, A. Martin, V. Khoze, and A. Shuvaev *J.Phys.* **G36** (2009) 093001, arXiv:0907.1374 [hep-ph].

[66] P. Lipari and M. Lusignoli *Eur.Phys.J.* **C73** no. 11, (2013) 2630, arXiv:1305.7216 [hep-ph].

[67] L. Demortier. CDF note 8661, http://www-cdf.fnal.gov/physics/statistics/notes/cdf8661_chi2fit_w_corr_syst.pdf.

[68] G. Antchev *et al. Europhys.Lett.* **101** (2013) 21002.

[69] E. Nagy, R. Orr, W. Schmidt-Parzefall, K. Winter, A. Brandt, *et al. Nucl.Phys.* **B150** (1979) 221.

[70] F. Nemes and T. Csörgő `arXiv:1202.2438 [hep-ph]`.

[71] A. Bzdak *Acta Phys.Polon.* **B38** (2007) 2665–2672, `arXiv:hep-ph/0701028 [hep-ph]`.

[72] A. Bialas and A. Bzdak *Phys.Lett.* **B649** (2007) 263–268, `arXiv:nucl-th/0611021 [nucl-th]`.

[73] A. Bialas and A. Bzdak *Phys.Rev.* **C77** (2008) 034908, `arXiv:0707.3720 [hep-ph]`.

[74] R. Glauber and J. Velasco *Phys.Lett.* **B147** (1984) 380.

[75] R. J. Glauber *Nucl.Phys.* **A774** (2006) 3–13, `arXiv:nucl-th/0604021 [nucl-th]`.

[76] M. M. Block *Phys.Rept.* **436** (2006) 71–215, `arXiv:hep-ph/0606215 [hep-ph]`.

[77] L. Jenkovszky and A. Lengyel `arXiv:1410.4106 [hep-ph]`.

[78] V. Khoze, A. Martin, and M. Ryskin *J.Phys.* **G42** no. 2, (2015) 025003, `arXiv:1410.0508 [hep-ph]`.

[79] H. Cheng and T. T. Wu *Phys.Rev.Lett.* **22** (1969) 666.

[80] C. Bourrely, J. Soffer, and T. T. Wu *Phys.Rev.* **D19** (1979) 3249.

[81] C. Bourrely, J. Soffer, and T. T. Wu `arXiv:1405.6698 [hep-ph]`.

[82] I. Bautista and J. Dias de Deus *Phys.Lett.* **B718** (2013) 1571–1573, `arXiv:1212.1764 [nucl-th]`.

[83] M. Giordano and E. Meggiolaro *JHEP* **1403** (2014) 002, `arXiv:1311.3133 [hep-ph]`.

[84] V. Anisovich, V. Nikonov, and J. Nyiri *Phys.Rev.* **D90** no. 7, (2014) 074005, `arXiv:1408.0692 [hep-ph]`.

Magyar nyelvű összefoglaló (Hungarian summary)

A TOTEM kísérlet tagjaként a Roman Pot detektorok proton-proton mérési adatai segítségével kalibráltam az LHC nyaláb optikáját, így közel egy nagyságrenddel csökkentettem a proton-proton szórás teljes hatáskeresztmetszetének legnagyobb szisztematikus hibáját. Ezzel lehetővé tettem a proton-proton szórás teljes hatáskeresztmetszet értékének minden korábbinál pontosabb meghatározását a CERN LHC $\sqrt{s} = 7$ és 8 TeV energiáin.

A Bialas-Bzdak modell publikált számításait ellenőriztem, majd meghatároztam a modell paramétereinek legjobb értékét és hibáit az ISR és LHC gyorsítók energiáin. Megmutattam, hogy az eredeti Bialas-Bzdak modell nem írja le helyesen az LHC energián mért adatokat. Bevezettem egy effektív proton sugarat R_{eff} melynek négyzete arányos a proton-proton szórás teljes hatáskeresztmetszetével az ISR energiákon.

Általánosítottam a Bialas-Bzdak modellt a szórási amplitúdó valós részének perturbatív figyelembevételével. Az így kapott modellt, αBB modell, illesztettem a mérési adatokra az ISR és LHC energiákon is. Megmutattam, hogy az αBB modell az ISR energiákon illeszthető a diffraktív minimum körüli adatpontok elhagyása nélkül is, azonban az LHC $\sqrt{s} = 7$ TeV energiáján az új modell sem illeszthető. Az adatok analízise során észrevettem, hogy a teljes proton-proton szórási hatáskeresztmetszet és az első diffraktív minimum helyzetének szorzata az ütközés energiájától független számra vezet, mely azonban eltér a "fekete korong" modellből számolható egzakt értéktől. Ezzel megállapítottam, hogy a "fekete korong" szórási határesetet nem értük el a $\sqrt{s} = 7$ TeV LHC energián.

Unitaritási kényszerekkel általánosítottam a Bialas-Bzdak modellt tetszőlegesen nagy valós részt tartalmazó elasztikus szórási amplitúdó esetére, majd megmutattam, hogy az így kapott ReBB modell illeszthető mind az ISR, mind az LHC energiákon. A ReBB modell paramétereinek energiafüggésére statisztikailag jó leírást találtam, mellyel kiszámoltam a teljes hatáskeresztmetszet várható értékét több jövőbeli LHC energiára. Megmutattam, hogy az ISR-hoz képest az LHC-nál a proton kölcsönhatási sugara lényegesen megnő. Felfedeztem, hogy kis elasztikus szórási szögek esetén a ReBB modell a rugalmas proton-proton differenciális hatáskeresztmetszet alakjára az exponenciálistól eltérő viselkedését jósol, mely összhangban van a TOTEM kísérlet legfrissebb, jelenleg a folyóirat általi elbírálás, referálás állapotában levő közleményével.

Summary

For the TOTEM experiment I have calibrated the LHC beam optics at IP5 by exploiting the proton-proton data measured by the TOTEM RP detectors. The calibration reduced the largest systematic error of the total proton-proton cross-section measurement with about an order of magnitude. With this calibration result, I made it possible to measure the total proton-proton cross-section σ_{tot} with very good accuracy at CERN LHC $\sqrt{s} = 7$ and 8 TeV energies.

I have checked and confirmed the published results of the Bialas-Bzdak model, described in the introduction and I have determined the best value and uncertainty of their model parameters at ISR and LHC energies. I have demonstrated, that the original Bialas-Bzdak model is not able to describe the TOTEM data, measured at the LHC. I have defined an effective proton radius whose square R^2_{eff} is proportional to the total proton-proton cross-section σ_{tot} at ISR energies.

I have generalized the Bialas-Bzdak model by adding a perturbatively small real part to its elastic scattering amplitude. I have fitted the improved αBB model to data measured at ISR and LHC energies. I have achieved, that the αBB model can be fitted to the ISR data without adjusting the fit range. I have found that even the αBB model is not able to interpret the data measured at LHC energy of $\sqrt{s} = 7$ TeV. I have discovered, that the product of the total proton-proton cross-section σ_{tot} and the squared four-momentum transfer position of the dip t_{dip} leads to a value which is approximately independent from the collision energy. I have also found that the so-called "black disk" model shows a similar and exact behavior, however, the exact value differs from the measured one.

Using unitarity constraints I have generalized the BB model by adding an arbitrarily large real part to its scattering amplitude in a systematic way. I have shown that the improved model, ReBB model, is able to describe the data measured at ISR and LHC energies in a statistically acceptable manner. I found a statistically acceptable description of the energy dependence of the ReBB model parameters, with which I was able to estimate the expected value of the total proton-proton cross-section at future LHC energies and beyond. I have shown as well, that the effective interaction radius of the proton is substantially increasing with increasing colliding energy between ISR and LHC. I have discovered that for low values of the squared four-momentum transfer $|t|$ the ReBB model predicts a non-exponential behavior in the elastic proton-proton differential cross-section.